2019

Smoothed Particle Hydrodynamics Modelling of the Impact of a Flat Plate upon an Aerated Water Surface

Sdiq, Hassan Muhammad

COPYRIGHT STATEMENT

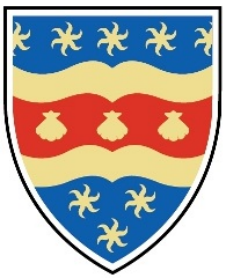

University of Plymouth

Smoothed Particle Hydrodynamics

Modelling of the Impact of a Flat Plate upon an Aerated Water Surface

By

HASSAN SDIQ

A thesis submitted to the University of Plymouth
in partial fulfilment for the degree of

DOCTOR OF PHILOSOPHY

School of Computing, Electronics and Mathematics

JULY 2019

ACKNOWLEDGEMENTS

I would like to thank my supervisors, Dr David Graham director of my study and Dr Jason Hughes, my third director, who introduced Smoothed Particle Hydrodynamics (SPH) to me and kindly helped me in everything I needed. Especially, Dr David director of my work, for his patience, support and encouragement during my study and for being available in opened his office any day at any time I needed. ...

DEDICATION

This thesis is dedicated to my loving wife, Barham, for her endless love, support and encouragement, whose sacrificial care for me and our children made it possible for me to finish this work. A very big shock and totally unexpected news in my life is knowing she has been diagnosed with cancer. Now it is time for my sacrifice to care for you and say: you are not alone, I am here to help and care for you at any and every step of life. You have been and will be always in my prayers.

To our lovely daughters, Hasty and Deya, and our new- born son, Bawan, who are indeed treasure from God. . . . Next, I gratefully dedicate this work to my beloved parents, may God preserve them for encouraging and your honest living for us and teaching me trust.

In memory of my grandparents for their love ...

Author's declaration

At no time during the registration for the degree of Doctor of Philosophy has the author been registered for any other University award without prior agreement of the Doctoral College Quality Sub-Committee.

Work submitted for this research degree at the University of Plymouth has not formed part of any other degree either at the University of Plymouth or at another establishment.

Workshop and Conference Attended:

2014 2-day Short course on SPH, University of Manchester.

2015 10th International SPHERIC SPH Workshop, University of Parma, Italy.

Presentations:

2016 SPH Single and multi-phase simulations, Marine department, University of Plymouth.

2017 SPH Single-phase simulations, Mathematics department, University of Plymouth.

Conference Presentation:

2017 SPH modelling of the impact of a flat plate upon an aerated water surface, 27th International Ocean and Polar Engineering conference, San Francisco, USA (ISOPE 2017).

Conference Paper:

2019 Smoothed Particle Hydrodynamics of Flat Plate Impact on Aerated Water, 2019 SPHERIC International Workshop, University of Exeter, UK.

Word count of main body of thesis: 35214

SIGNED:..... DATE:.....

Abstract

Smoothed Particle Hydrodynamics Modelling of the Impact of a Flat Plate upon an Aerated Water Surface

Hassan Sdiq

Smoothed Particle Hydrodynamics (SPH) is a particle-based method for solving Navier-Stokes and similar equations and is well-suited to problems where the computational domain becomes highly deformed. This study will describe in detail SPH simulations of various single- and multiphase flows with free surfaces and interactions with structures and solid surfaces. All 2D and 3D implementations have been compared with other numerical and experimental results. By adoption of multi-phase and 3D models the computational requirements rise due to the increased number of particles. The fact that large numbers of particles are required in the simulations means that a parallelised version of the SPH code has had to be developed. Cases considered in this study include collapsing water column, Rayleigh-Taylor instability and bubble rising. The main focus is the impact of a flat plate upon a bubbly water/air mixture, modelling experimental tests carried out in the FROTH project at the University of Plymouth. We show that successful predictions of peak impact pressure for varying levels of aeration can be achieved by matching sound speed to those of a homogeneous air-water mixture at the appropriate level of aeration.

CONTENTS

LIST OF FIGURES

CHAPTER 1

INTRODUCTION

Contents

1.1 Background and Motivation

The impact of a solid upon a water surface during water entry is very important in marine structures, especially due to the high impact pressures experienced. Wave slamming, fuel sloshing in tank, overturning wave, the impact of solid objects into water are all examples of violent impact on a free surface. A further example is when an aircraft needs to ditch on water or dive into water and the resulting violent impact load on the body can lead to injuries or damages. An accurate prediction or calculation of these pressure impact may save lives and reduce damage.

Such impact problems are intractable analytically and must be studied using numerical methods.

Several numerical methods have been used to simulate the impact problems, (Zhao et al. (1996), Yan & Ma (2007), Zhang (2010)). In general, mesh-based methods are commonly implemented. Mesh-based methods have difficulty in capturing fluid phenomena such as flow separation and large motions of the fluid free surface. To deal with this problem, mesh-free methods such as smoothed particles hydrodynamics (SPH) have been used.

The main goal in this study is to use an SPH method to simulate the impact of a flat plate on a water surface, as carried out experimentally in the FROTH project at Plymouth University, Mai (2017). A novel feature of the experiments was that, in order to mimic wave/structure impacts, the water was aerated by bubbling air from underneath the water surface. This created a non-homogeneous, compressible mixture. Here, simulations of these experiments have been carried out using single-phase and multi-phase SPH models in both two and three spatial dimensions.

Simulating 2D multi-phase and 3D requires a large number of particles. The number of interactions between particles will be very large thus using a single processor would take a large computation time and the number of particles would be limited. Here a parallel MPI code is created to address this problem.

In this work, the speed of the plate as it enters the water is specified

from the experiments and data from this are used as boundary conditions for the SPH model. The sound speeds used in this study are much larger than ten times the maximum fluid velocity and are set as physical sound speeds determined by aeration levels in the water-air mixture.

1.2 Thesis Structure

In Chapter Two, the most recent and relevant Smoothed Particle Hydrodynamics (SPH) literature will be reviewed. In Chapter Three, the SPH formulations will be presented, focusing in the Colagrossi & Landrini (2003) model which will be used for simulation of multi-phase flows and the plate drop. In the next chapter, parallel programming using Message Passing Interface (MPI) will be briefly described. Chapter Five presents two dimensional single phase and multi-phase simulations which are compared with experimental and numerical results. Chapter Six presents the validation of single and multiphase dam break cases using 3D. The results have been compared with experimental and other numerical results. Single-phase two and three dimensional simulations of flat plate dropping onto the water are compared with results from the FROTH project at Plymouth University in Chapter Seven. Three dimensional drop cases are presented in Chapter Eight. Finally, the main conclusions of the study are given in the last chapter.

CHAPTER 2

LITERATURE REVIEW

Contents

2.1 Overview

Wave tank sloshing and impact of objects into water are examples of complex free surface fluids. The impact of solid objects in the water is important in many applications such as ship hydrodynamics, dam-breaking and force-prediction problems.

In general two approaches are used to simulate free-surface flow. Nu-

merical methods like the finite element method, finite difference method and finite volume method are grid-based methods. However, these methods can be very expensive for large deformation problems, due to re-meshing at each time step.

Particle methods do not need any grid or mesh and follow the particles through the flow. The numerical method Smoothed Particle Hydrodynamics (SPH) is one of the oldest meshless methods. It was developed by Gingold & Monaghan (1977) and Lucy (1977). Since then, it has been widely used to simulate and investigate different fields in hydro-engineering, Cao et al. (2014), Gong et al. (2009), Marrone, Colagrossi, Antuono, Lugni & Tulin (2011) and Sun et al. (2015) and geophysical applications. SPH is a fully Lagrangian particle-tracking method which is more suitable for large surface motions complex geometry than grid-based Eulerian methods which are required to re-mesh many times during a simulation.

There are many different implementations of SPH, but two approaches are very commonly used for modelling incompressible flows: incompressible (ISPH) and weakly-compressible (WCSPH). The pressure calculation is the main difference between them. In ISPH, particle pressures are calculated from Poisson's equation, but in WCSPH pressures are computed direct from the density, Lee et al. (2008*a*), Hughes & Graham (2010) and Shadloo et al. (2012).

Lee et al. (2008*a*) presented comparisons of ISPH and WCSPH methods. Lid-driven cavity, flow around a bluff body located between two

plates and a dam-break case were simulated in order to compare both methods. Their results showed that ICSPH gave better comparisons with the reference solutions than WCSPH for the lid-driven cavity, but at higher Reynolds number WCSPH improved. In contrast to the previous study, Hughes & Graham (2010) showed the WCSPH performed at least as well as ICSPH. They compared both methods results for two dam-break cases and for wave impact against a vertical wall. Their simulations showed the WCSPH produced much smoother free-surface deformation than ISPH, especially for the overturning wave. Shadloo et al. (2012) showed the main benefit of using WCSPH method is that it is easier to program compared to the ISPH method. On the other hand, the WCSPH method can generate oscillations in the pressure field, but they showed that WCSPH could provide stable and accurate results without any noticeable noise in pressure values. To validate their results, they simulated flow over an airfoil and square obstacle and used both SPH methods and compared pressure and velocity contours; results were in very good agreement with results from the finite element method.

Several variants of original SPH have been improved to treatment and to improve pressure fields. Xu et al. (2009*a*) proposed a scheme to correct the error caused by irregular distribution of particles by shifting particle position. To improve this algorithm, Lind et al. (2012) used Fickan-based algorithm to compute the shifting location.

Vila (1999) proposed a Riemann solution method to determine the

interaction between particles. An analogy between SPH and the Finite volume method was exploited in Oger, Marrone, Touze & de Leffe (2016), who used a shifting algorithm in the ALE-SPH development of the Vila (1999) model. In passing, we also mention the δ-SPH method developed by Marrone, Antuono, Colagrossi, Colicchio, Touze & Graziani (2011) who added a diffusive term to the density evolution equation to filter out spurious pressure oscillations.

2.2 Boundary Treatment

As mentioned before, SPH is a useful numerical method, but it is not without problems. One of the most serious issues is kernel truncation near boundaries, due to a lack of particles at the boundary. The boundaries treatment can generally be summarised into three types: repulsive force, fixed dummy particles or ghost particles.

Monaghan (1994) proposed a technique for boundary treatment based on Lennard-Jones force between fluid and wall particles. In this methods the boundary is simulated as repulsive particles and when fluid particles approach the boundary, the force between them will increase and the chance of escaping particles through the boundary will be reduced. A disadvantage is that the interpolation near boundary is not completed. However, it practically easy to use for any geometry.

Another method used to simulate the boundary is dummy particles. This method was proposed by Koshizuka et al. (1998) and Gotoh & Sakai

(1999) and used by Shao & Lo (2003), Lee et al. (2008*b*), and Dalrymple & Knio (2001). In this method the boundary is simulated by multiple row of particles. A advantage of this treatment is the boundary particles fill the kernel support near the wall.

Libersky et al. (1993) presented boundary particles as ghost particles which are created outside the domain when the fluid particles reach a boundary. The number of ghost particles will vary in each time step. An advantage of this method is that boundary particles are only taking part of calculation if they are needed. in contrast, it is difficult to adopt this method with complex and sharp geometry.

The boundary integral method presented by Kulasegaram et al. (2004) treated solid boundaries by analytical integration of the kernel over the truncated area of the kernel domain. Feldman & Bonet (2007) developed the formulation for computing the correction term and it was extended for complex boundaries in 2D and 3D by Leroy et al. (2014) and D. Violeau (2014), respectively.

Full details of boundary conditions are given in 3.7 and later chapters.

2.3 Multi-phase simulations

One of the advantages of SPH is that it can easily deal with two or more fluids. Monaghan et al. (1999) used SPH to simulate two phases without any correction at the interface between phases. They dealt with each phase separately. The density ratio used was very large. Their method

yields some instability in the region between phases due to the large density gradient at the interface for small density ratio, Colagrossi & Landrini (2003).

Colagrossi & Landrini (2003) proposed a modified method of computation for those particles at interfaces with density discontinuities. They used an extra force in the pressure term for the low-density phase to prevent particle dispersion to the more dense phase. They successfully simulated air-water interaction. To smooth pressure fluctuations they used a density re-normalization technique.

Hu & Adams (2006) used a different approach. They used a Shepard function to remove the large differences between density. The volume of particles supported by kernel is not affected by the density. The density will be influenced by the particle's own volume. They showed their method was capable of simulating three or more phases; to show validation of their method capillary wave, three-phase interaction and drop deformation were investigated and compared with analytic solutions, previous numerical results and experiments. Their method was not computationally expensive, but costs increased slightly when the number of phases was increased. Hu & Adams (2007) developed an incompressible multi-phase SPH method. In this method, they calculated the pressure of particles by solving Poisson's equation and the density was updated from the continuity equation. Their modified method used a fractional time step method for both density and velocity update with new mul-

tiphase projection formulations in which the discretized gradient and divergence operator did not require a differentiable density or viscosity. They compared their results with other numerical and experimental results and showed good accuracy and convergence properties. Hu & Adams (2009*b*), modified their incompressible method. They introduced a constant density approach to simulate flows with large ratio density.

Another approach was proposed by Grenier et al. (2009), in which they combined the Hu & Adams (2006) and Colagrossi & Landrini (2003) methods. In this method they used the same equations for both phase with an external repulsive force for the pressure gradient. Colagrossi & Landrini (2003) also used a different re-normalization density.

In 2013, Monaghan & Rafiee (2013) improved the early approach proposed by Monaghan et al. (2011) by using the new term instead of artificial viscosity and this new term depends on density ratio of fluids.

Koukouvinis (2012) developed a mesh free particle method for steady and unsteady free surface flows. He showed the particle approximation errors may increase due to the non-uniform distribution of particles and voids will appear between particles. He used particle redistribution to remove the voids. The voids appeared at high resolutions with initial particle distance dx smaller than 0.0024, Mokos et al. (2017) used the shifting algorithm to remove the voids present in the air phase.

2.4 Flat plate drop

The impact between solid objects and water surface is crucial in numerous situations, such as ship hydrodynamics, aircraft impacts and breaking dam problems. This is because predicting impact pressure for the impact problem is very challenging. The air phase has a important role prior to impact on the water surface and the impact pressure, Lind et al. (2015*a*).

Oger et al. (2006) simulated a 2D wedge water entry. They used SPH method with variable smoothing length. Their predictions of vertical and angular accelerations and pressure agreed with experimental results. However, they found out that there is a disagreement with experimental results at the prior of the the impact due to neglecting the air phase in their investigation.

In 2012, Gao et al. (2012) used a 2D single-phase SPH to simulate wave slamming on an open-piled structure. They employed Riemann solution to make the water phase stable. It was found that the spatial resolution could have a large influence on flow structure in the splash-up area, but it had less influence on falling velocity and fluid force. Their results were compared to the experimental data and were in reasonable agreement.

Skillen et al. (2013) modified the ISPH method using diffusion-based shifting to investigate wedge and cylinder impacts on a water surface and wave impact on a cylinder. They showed that their prediction results for those three cases were more accurate than previous SPH models. They

neglected the air phase in all cases.

Lind et al. (2015*b*), applied the multiphase ISPH to simulate flat plate impact onto a wave and flat water surface. Their investigation clearly showed that ISPH was able to predict the high pressure at the impact time. The air phase was taken into account and they showed the influence of the air phase on the peak pressure and free surface. Their results were compared with experiments and there was good agreement between them.

2.4.1 Experimental study of impact phenomena

Experimental work related to the flat plate impact upon still water has been reported experimentally by number of authors over several decades, for example Chuang et al. (1966), Verhagen et al. (1967),Lewison et al. (1968), Miyamoto & Tanizawa (1984), Lin & Shieh (1997), Okada & Sumi (2000), Huera-Huarte et al. (2011) and Peters et al. (2013).

All of these works clearly showed the importance of the air phase during hitting, especially the reduction of impact pressures due to the air phase and the affect of air on the water surface before hitting. Chuang et al. (1966) was an early experimental study of a flat-bottomed body dropping into still water from different positions above the water surface. They showed the maximum pressure calculated was significantly reduced compared to the pressure expected. This was due to trapped air between the body and the water surface. Verhagen et al. (1967) investigated exper-

imentally and numerically the impact of a flat plate on a water surface and also showed the influence of air trapped between the flat plate and water surface. Lewison et al. (1968) noted experiments giving values of peak pressure of the same order as those recorded on ships slamming at sea, but lower than expected for existing theories. Two different type of impact were investigated by Miyamoto & Tanizawa (1984), both experimentally and theoretically. The first was a numerical study of wedge entry with constant speed. In the second study, the infuence of trapped air was investigated. Okada & Sumi (2000) in their study investigated a wedge impact problem with a small impact angle. Huera-Huarte et al. (2011) studied experimentally the slamming force on flat panels hitting a free surface at different impact speeds and angles. Recently, Peters et al. (2013) performed an experimental and numerical study of the impact of circular disc on the water surface. In their study, they focused on splashing generated after impact and the force on the disc.

The accurate calculation of impact pressure is very important in the design of structures subjected to such pressures. Water entry of a body on a free surface, involves overturning of the free surface, fast splashing water and resolution of high impact pressures. Capturing the pressure impact has been challenging to numerical simulations due to the short duration of the impact and the large deformations occurring during the impact.

The main aim of our study is to simulate the behaviour of impact of

a flat plate on pure and aerated water surfaces, as carried out experimentally in the FROTH project at Plymouth University, Mai (2017). The loading pressure on the flat plate at the time of the entry will be the main focus.

2.5 Parallel programming

Using large numbers of particles will be computationally very expensive due to the interactions between particles needing a large number of computations, Viccione et al. (2008). To get achieve accuracy in the SPH method, a large number of particles is required and this will increase the time of computation of the simulation. This is especially true when we use multi-phase, as the time step will be significantly decreased for the low density (air) phase, Colagrossi & Landrini (2003) and this will increase the computational runtime. When modelling 3D cases the particle number will be significantly increased. Therefore, to simulate such cases, running serial code on a single CPU takes a large computation time and the number of particles will be limited if parallel code is not used. Therefore, parallelized code is designed to solve this issue.

To reduce computing time and to be able to use high numbers of particles, high performance computing has been used extensively in the literature, including open multi-processing (OpenMP), message passing interface (MPI) and graphic processing units (GPU), Maruzewski et al. (2010), Ferrari et al. (2010) Cherfils et al. (2012), Marrone et al. (2012) and

Oger, Le Touzé, Guibert, De Leffe, Biddiscombe, Soumagne & Piccinali (2016).

In the shared memory OpenMP setup, the program has two different parts, serial and parallel. The serial part will be executed in a master whilst the parallel part will be divided by the master into a number of slaves and then assigned to different processors. Each slave processor will be executed separately then, when the parallel code is finished, the code will be returned to the main thread which executes the rest of the program.

An alternative method for paralleliing the code is MPI which is a completely parallel system connecting large numbers of processors to each other through a network.

The use GPUs is another alternative which utilises the power of graphics processing units to perform parallel computations.

In this work, a multiphase SPH formulation will be used to simulate violent impact free surface flows. Simulating 3D multi-phase flows requires a large number of particles hence the use of parallel programming is required. In this work, we use the MPI protocol.

CHAPTER 3

SMOOTHED PARTICLE HYDRODYNAMICS FORMULATIONS

Contents

3.1 Introduction

Smoothed particle hydrodynamics (SPH) has been successfully applied to the modelling of fluid flow, solid mechanics and fluid-solid interactions, especially when this involves deformations. SPH is a fully Lagrangian method, which does not require the use of any mesh. It was invented by Gingold & Monaghan (1977) and Lucy (1977). Since then, the use of SPH has expanded in many areas of solid and fluid dynamics. Nowadays, the SPH method is widely used to simulate flows in hydro-engineering and geophysical applications. In the following sections, a summary of the SPH method is provided.

In the SPH, the Navier-Stokes equations are

$$\frac{D\boldsymbol{u}}{Dt} = -\frac{1}{\rho}\nabla p + \nu\nabla^2\boldsymbol{u} + \boldsymbol{f}, \tag{3.1}$$

$$\frac{D\rho}{Dt} = -\rho\nabla.\boldsymbol{u}, \tag{3.2}$$

$$\frac{D\boldsymbol{x}}{Dt} = \boldsymbol{u}. \tag{3.3}$$

Here, vector quantities are represented in bold face letters. "∇"and"$\nabla.$" are respectively the gradient and divergence operators, $\boldsymbol{u}$ is the velocity, t is the time, ρ is the density, p is the pressure, $\boldsymbol{f}$ is the sum of the external accelerations on the fluid e.g gravity, ν is the kinematic viscosity and $\boldsymbol{x}$ is the particle position.

The general idea of SPH is to approximate these equations. The SPH

represents fluids as a particles, which are used as a interpolation points. The equations of motion are then derived and interpolated for these particles. The particle's location and properties will be computed by using a time integration scheme. At the heart of SPH is the kernel interpolation, which is used for calculating all particle quantities.

3.1.1 Functions and derivative in SPH

In SPH fluid is discretised by a set of particles. They have the properties: mass, density, pressure, position, viscosity and velocity.

Function approximations in SPH

A function $A(\boldsymbol{x})$ can be approximated as, Monaghan (1982), Monaghan & Gingold (1983).

$$A(\boldsymbol{x}) = \int_{\Omega} A(\acute{\boldsymbol{x}}) W(\boldsymbol{x} - \acute{\boldsymbol{x}}, h) d\acute{\boldsymbol{x}}, \tag{3.4}$$

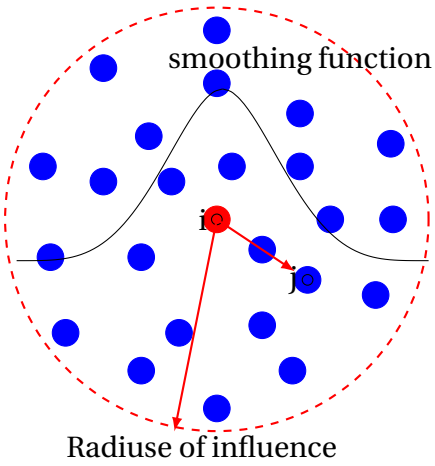

Figure 3.1: Domain and kernel function for a particle i including neighbor particles.

where Ω is the supporting domain, $W(x - \acute{\boldsymbol{x}}, h)$ is an interpolating

kernel with h as the smoothing length.

In discrete form, equation 3.4 can be written as

$$A(\boldsymbol{x}_i) = \sum_j V_j A_j W(|\boldsymbol{x}_i - \boldsymbol{x}_j|, h). \tag{3.5}$$

where V_j is the volume of particle j, $|\boldsymbol{x}_i - \boldsymbol{x}_j|$ is the distance between particles i and j, Monaghan (1992). The interpolating function $A(\boldsymbol{x}_i)$ is shown in Figure 3.1 and the integral in 3.4 is approximated by kernel summation over the neighbouring particles.

Derivative in SPH

Following the SPH approach to describe a function $A(\boldsymbol{x})$, the gradient of function $A(\boldsymbol{x})$ can be approximated with

$$\nabla A(\boldsymbol{x}) = \int_\Omega \nabla A(\acute{\boldsymbol{x}}) W((\boldsymbol{x} - \acute{\boldsymbol{x}}), h) d\acute{\boldsymbol{x}}. \tag{3.6}$$

By invoking Gauss's theorem, equation 3.6 becomes

$$\nabla A(\boldsymbol{x}) = \int_S A(\acute{\boldsymbol{x}}) W(\boldsymbol{x} - \acute{\boldsymbol{x}}, h) \boldsymbol{n} dS - \int_\Omega A(\acute{\boldsymbol{x}}) \nabla_{\acute{x}} W(\boldsymbol{x} - \acute{\boldsymbol{x}}, h) d\acute{\boldsymbol{x}}. \tag{3.7}$$

here $\boldsymbol{n}$ is the unit vector normal to surface S. The first integral of equation 3.7 can be converted into a surface integral and the surface integral is zero, as $W(\boldsymbol{x} - \acute{\boldsymbol{x}}, h) = 0$ when $|\boldsymbol{x} - \acute{\boldsymbol{x}}| > kh$. Then the first term in equation 3.7 vanishes and the derivative of a function becomes

$$\nabla A(\boldsymbol{x}) = -\int_\Omega A(\acute{\boldsymbol{x}}) \nabla W(\boldsymbol{x} - \acute{\boldsymbol{x}}, h) d\acute{\boldsymbol{x}}. \tag{3.8}$$

Eq.(3.8) can be written in discrete form, giving

$$\nabla A(\boldsymbol{x}) = -\sum_j \frac{m_j}{\rho_j} A(\acute{\boldsymbol{x}}) \nabla W(\boldsymbol{x} - \acute{\boldsymbol{x}}, h), \tag{3.9}$$

thus a derivative of a function $A(\boldsymbol{x})$ at a particle position $\boldsymbol{x}_i$ can be written as

$$\nabla A(\boldsymbol{x}_i) = -\sum_j \frac{m_j}{\rho_j} A(\boldsymbol{x}_j) \nabla_i W_{ij}(\boldsymbol{x}_i - \boldsymbol{x}_j, h), \tag{3.10}$$

where the derivative of the kernel function can be expressed as $\nabla_i W_{ij} = \frac{\boldsymbol{x}_i - \boldsymbol{x}_j}{r_{ij}} \frac{\partial W_{ij}}{\partial r_{ij}}$ where $\boldsymbol{x}$ is the vector containing the position of a particle and r_{ij} is the absolute value of the distance between particle i and j. Furthermore, $\nabla_i W_{ij} = -\nabla_j W_{ij}$ and then the equation 3.10 becomes

$$\nabla A(\boldsymbol{x}_i) = \sum_j \frac{m_j}{\rho_j} A(\boldsymbol{x}_j) \nabla_j W_{ij}(\boldsymbol{x}_i - \boldsymbol{x}_j, h). \tag{3.11}$$

3.2 Kernel function

In the previous section we showed how the integral interpolation depended on the kernel. The accuracy of the particle approximation in equation 3.5 is determined by the choice of smoothing functions. The kernel function influences the results of SPH approximations. Choosing the weighting function is one of the important factors in SPH formulation and needs to be selected by the user. In general, there is no "best" choice of kernel function used in SPH. However, there are some requirements and important properties which are summed up as in Liu & Liu (2003).

- the integral of the weighting function must be unity over its support domain

$$\int_\Omega W(\boldsymbol{x}) d\boldsymbol{x} = 1. \tag{3.12}$$

- the smoothing function should have compact support, which means

$$W(\boldsymbol{x}-\acute{\boldsymbol{x}},h)=0,\ for\mid \boldsymbol{x}-\acute{\boldsymbol{x}}\mid > kh. \tag{3.13}$$

  where kh defines size of the influence domain. The factor k is normally set to 2.

- when the smoothing length h tends to zero, the smoothing function becomes a Dirac function

$$\lim_{\boldsymbol{x}\to 0}, W(\boldsymbol{x}-\acute{\boldsymbol{x}},h)=\delta(\boldsymbol{x}-\acute{\boldsymbol{x}}) \tag{3.14}$$

- the smoothing function must be positive over its domain.

The choice of the smoothing functions affects computational costs and the stability of the method. Note also that it is possible to achieve a higher order approximation of equation 3.4 by removing the positivity condition Lind & Stansby (2016). This is not done in the present work. The user can choose from one of several kernel choices, such as the Gaussian function, the cubic spline function and the Wendland function. These are defined below:

Gaussian Function

The Gaussian function is a very capable function, even for complex geometry, Liu & Liu (2003). However, due to its non-compact support, it can be very expensive computationally. The standard form of the Gaussian function is defined below and Figure 3.2 shows the kernel and its

derivatives:

$$w(q) = \alpha_d e^{-q^2}, \qquad \frac{dw}{dq} = \alpha_d(-\frac{2r}{h^2}e^{-q^2}),$$

where $\alpha_{1D} = \frac{1}{h\sqrt{\pi}}, \alpha_{2D} = \frac{1}{\pi h^2}, \alpha_{3D} = \frac{1}{\sqrt{\pi^3 h^6}}$ $q = \frac{r}{h}$, r is the absolute distance

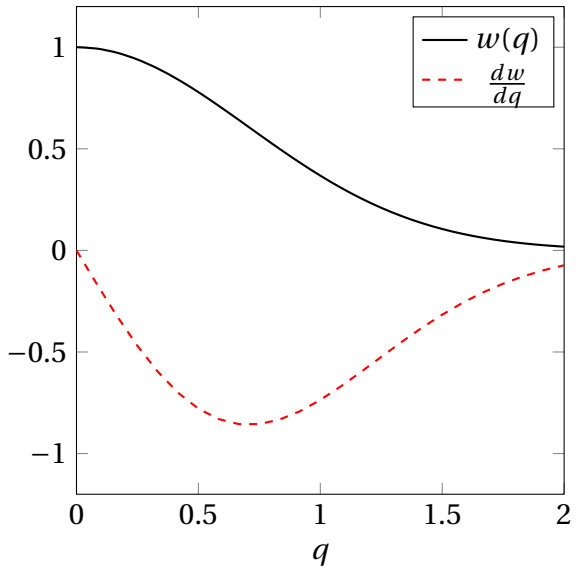

Figure 3.2: Gaussian function.

between particles. The kernel function clearly depends on h and, via q, also depends on distance r.

Cubic Spline Function

The standard form of the cubic spline is defined below as, Morris et al. (1997):

$$w(q) = \alpha_d \begin{cases} 1 - \frac{3}{2}q^2 + \frac{3}{4}q^3 & \text{for} \quad 0 \le q < 1 \\ (2-q)^3/4 & \text{for} \quad 1 \le q < 2 \\ 0 & \text{for} \quad q \ge 2 \end{cases}$$

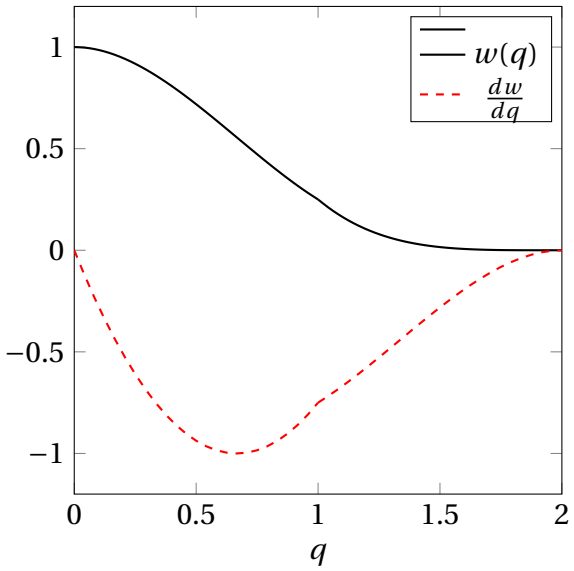

Figure 3.3: Cubic spline function.

The kernel has the dimension $(length)^{-D}$ for D-dimensional problems, $q = \frac{r}{h}$, $\alpha_d = \frac{10}{7\pi h^2}$, $\alpha_d = \frac{1}{\pi h^3}$ for 2D and 3D, respectively.

Quintic (Wendland, 1995)

The standard form of Wendland function is written as, Wendland (1995).

$$w(q) = \alpha_d \begin{cases} (1-\frac{q}{2})^4(2q+1), & \text{for} \quad 0 \le q \le 2; \\ \\ 0 \quad \text{for} \quad q \ge 2, \end{cases}$$

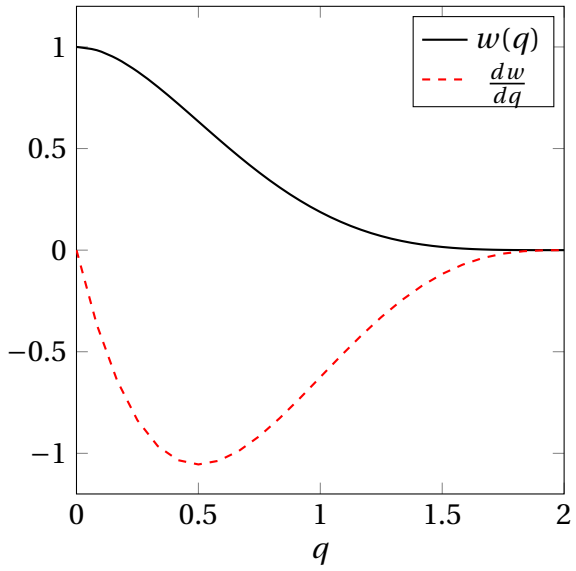

Figure 3.4: Wendland function.

where $q = \frac{r}{h}$ and $\alpha_d = \frac{7}{4\pi h^2}$ and $\alpha_d = \frac{7}{8\pi h^3}$ for 2D and 3D, respectively.

3.2.1 Smoothing Length

The choice of the smoothing length h determines the number of interactions for each particle. When h is too small, there are not enough particles inside the kernel to interact with and the result of simulation can become unstable. When h is too big, there are many particles to interact with and

simulations become expensive. In this work we used a smoothing length around 1.3 times the initial particle spacing Δx, and the circle of support has a radius of 2 times smoothing length, Quinlan et al. (2006).

3.3 Equations of Fluid in SPH

The conservation laws from section 3.1 can be combined with SPH approximations of function from section 3.1.1. The equations were derived by Monaghan (1994) and have been used by many authors with SPH.

3.3.1 Conservation of Mass

For conservation of mass, there is no change of mass in an arbitrary volume $v(t)$. This can be expressed as:

$$\frac{D}{Dt}\int_{v(t)} \rho dv = 0.$$

In differential form,

$$\frac{D\rho}{Dt} = -\rho\nabla.\boldsymbol{u} = -\nabla.(\rho\boldsymbol{u}) + \boldsymbol{u}.\nabla\rho.$$

When the particle approximation of a derivative is employed, this can be expressed as

$$\frac{D\rho_i}{Dt} = -\nabla_i(\rho\boldsymbol{u}) + \boldsymbol{u}_i.\nabla_i\rho,$$

then

$$\frac{D\rho_i}{Dt} = -\sum_j \frac{m_j}{\rho_j}(\rho_j\boldsymbol{u}_j).\nabla_i W_{ij} + \boldsymbol{u}_i\sum_j \frac{m_j}{\rho_j}\rho_j.\nabla_i W_{ij}.$$

After simplifying, this becomes:

$$\frac{D\rho_i}{Dt} = \sum_j m_j(\boldsymbol{u}_i - \boldsymbol{u}_j).\nabla_i W_{ij}. \tag{3.15}$$

3.3.2 Conservation of Momentum

To formulate the conservation of momentum under the SPH method, pressure and viscous forces need to be calculated. We use the following formulation to calculate the momentum. The pressure gradient from equation 3.5 becomes

$$\nabla p_i = -\sum_j m_j \frac{p_i}{\rho_j} \nabla W(\boldsymbol{x}_i - \boldsymbol{x}_j, h). \tag{3.16}$$

The product rule for differentiation gives us the equation

$$\nabla(p1) = 1\nabla p + p\nabla 1 \longrightarrow 1\nabla p = \nabla(p1) - p\nabla 1,$$

which can be used to reformulate the pressure force term as

$$\nabla p_i = \sum_j \frac{m_j}{\rho_j} p_j \nabla_i W_{ij} + p_i \sum_j \frac{m_j}{\rho_j} 1\nabla_i W_{ij},$$

From Equation 3.17 after simplification this becomes

$$\nabla p_i = \sum_j \frac{m_j}{\rho_j}(p_j + p_i)\nabla_i W_{ij}. \tag{3.17}$$

From Equation 3.1, we have

$$\frac{D\boldsymbol{u}_i}{Dt} = \boldsymbol{f}_i - \sum_j \frac{m_j}{\rho_i \rho_j}(p_i + p_j)\nabla_i W_{ij} + \nu\nabla^2 u. \tag{3.18}$$

Now the particle approximation of the full Navier-Stokes equation, inclusive of the viscosity term, is given by

$$\frac{D\boldsymbol{u}_i}{Dt} = \boldsymbol{f}_i - \sum_j \frac{m_j}{\rho_i \rho_j}(p_i + p_j + \Pi_{ij})\nabla_i W_{ij}, \tag{3.19}$$

where Π_{ij} is a viscous term which will be explained in the next section. $\boldsymbol{f}_i$ is the acceleration due to a body force.

3.3.3 Density Evaluation

In SPH, the conservation of mass for fluid particle i leads to calculation of the particle density at its local position $\boldsymbol{x}_i$. The density of the particle can be evaluated from the mass of neighbouring particles using Equation 3.15, Monaghan (1992).

Summation Density

The first SPH formulations for conservation of mass was derived directly from summation interpolation, equation 3.5, Monaghan (1992). By substituting ρ_i in $A(\boldsymbol{x}_i)$ in equation 3.5 becomes

$$\rho_i = \sum_j \frac{m_j}{\rho_j} \rho_j W(|\boldsymbol{x}_i - \boldsymbol{x}_j|, h), \tag{3.20}$$

from $\rho_j \neq 0$ then we have

$$\rho_i = \sum_j m_j W(|\boldsymbol{x}_i - \boldsymbol{x}_j|, h). \tag{3.21}$$

Evolved Density

The second SPH formulation for conservation of mass, Monaghan (1992) leads to

$$\frac{d\rho_i}{dt} = \sum_j m_j (\boldsymbol{u}_i - \boldsymbol{u}_j).\nabla_i W_{ij}. \tag{3.22}$$

Equation 3.22 will be called the "evolved density equation" where $\nabla_i W_{ij}$ is the gradient of the kernel function with respect to coordinates of the given particle i.

Since

$$q_{ij} = \frac{r_{ij}}{h},$$

$$\frac{\partial W_{ij}}{\partial \boldsymbol{x}_i} = \frac{\partial q_{ij}}{\partial \boldsymbol{x}_i} \frac{dW_{ij}}{dq_{ij}},$$

and

$$\nabla_i W_{ij} = \frac{(\boldsymbol{x}_i - \boldsymbol{x}_j)}{h r_{ij}} \frac{dW_{ij}}{dq_{ij}}.$$

where $r_{ij} = \sqrt{((x_i - x_j)^2 + (y_i - y_j)^2)}$ and $W_{ij} = W(q_{ij})$ and similarly for $\nabla_j W_{ij}$. In this study the evolved density formulation is employed to evaluate the density of particle i.

3.4 Pressure Evaluation

From the density of each particle the pressure can be evaluated with a stiff equation of state, Monaghan (1994). The equation of state can be expressed as

$$p(\rho) = B[(\frac{\rho}{\rho_0})^\gamma - 1 + \chi], \tag{3.23}$$

where $B = \frac{c_0^2 \rho_0}{\gamma}$ where c_0 is the reference of speed of sound, ρ_0 is reference density, Monaghan (1994). γ is constant and is usually set equal to 7 for water, Monaghan (1994), χ is background pressure. B is a constant used

to ensure the Mach number $M = \frac{u}{c}$ is small. Small δt variation of that density is directly affected by the square of Mach number, Monaghan (1994). To keep the compressibility to 1% or less in this simulation, the Mach number is set $M \leqslant 0.1$.

When a simulation needs to run with hydrostatic pressure, the initial density is used to produce hydrostatic pressure from the equation of state. Then the initial density is evaluated with

$$\rho_i = \rho_0 \left(1 + \frac{\rho_0 g(H - y_i)}{B}\right)^{1/\gamma} \tag{3.24}$$

where H is the initial water depth, y_i is the vertical particle position measured from the bottom of the tank and the other parameters are the same as equation 3.23.

3.5 Density Reinitialization

From equation 3.23, any small change in the density of particles can lead to much larger changes in the pressure field. To control any change in density, two methods have been employed, Colagrossi & Landrini (2003). First, the Shepard filter is a quick and simple correction to the density, and the following procedure is applied every n_r=15 time steps in the code

$$\rho_i^{new} = \sum_j \rho_j \widetilde{W_{ij}} \frac{m_j}{\rho_j} = \sum_j m_j \widetilde{W_{ij}}, \tag{3.25}$$

where the kernel has been corrected using a zeroth-order correction

$$\widetilde{W_{ij}}_i = \frac{W_{ij}}{\sum_j \widetilde{W_{ij}} \frac{m_j}{\rho_j}}. \tag{3.26}$$

In our work, values of n_r between 5 and 30 were tested.

Second, the Moving Least Square (MLS) approach was developed by Dilts (1999) and used successfully by Colagrossi & Landrini (2003) and by Panizzo & Dalrymple (2004). MLS is a first-order correction. Using MLS requires inverting a 3x3 matrix for 2 dimensions and 4x4 matrix for 3 dimensions for each particle. This procedure is computationally expensive, especially when it might need to be used every few time steps. For this reason we prefer to use Shepard filter which is much faster than MLS.

3.6 Viscosity

The second term of the equation 3.1 refers to the viscosity, and involves a second derivative of the velocity. Two different approaches for diffusion are presented:

- Artificial viscosity in introduced by Monaghan (1982).

- Laminar viscosity model introduced by Morris et al. (1997)

3.6.1 Artificial Viscosity

The artificial viscosity proposed by Monaghan (1982) has been used very often. Π_{ij} is the viscosity term, and is defined by

$$\Pi_{ij} = \begin{cases} \frac{-\alpha \bar{c_{ij}} \mu_{ij}}{\rho_{ij}}, & \text{for} \quad \boldsymbol{u}_{ij}.\boldsymbol{r}_{ij} < 0 \\ \\ 0 & \text{for} \quad \boldsymbol{u}_{ij}.\boldsymbol{r}_{ij} > 0 \end{cases} \tag{3.27}$$

with $\mu_{ij} = \frac{h\boldsymbol{u}_{ij}.\boldsymbol{r}_{ij}}{\boldsymbol{r}_{ij}^2}$, $\boldsymbol{u}_{ij} = \boldsymbol{u}_i - \boldsymbol{u}_j$; $\boldsymbol{r}_i$ and $\boldsymbol{u}_i$ being the position and velocity corresponding to particle i; $\bar{c_{ij}} = \frac{c_i + c_j}{2}$; c_i and c_{ji} are the speed of sound; α is a free parameter that can be changed to each problem, is often taken as $\alpha \in [0.01, 0.5]$.

3.6.2 Laminar Viscosity

The laminar viscosity used by Morris et al. (1997) is

$$\Pi_{ij} = m_j \frac{(\mu_i + \mu_j)(\boldsymbol{x}_i - \boldsymbol{x}_j)}{\rho_i \rho_j} \boldsymbol{u}_{ij}. \tag{3.28}$$

In the present study, the viscosity is constant ($\mu_i = \mu_j$) in the single phase, then viscous term expression 3.28 is

$$\Pi_{ij} = m_j \frac{2\mu_i(\boldsymbol{x}_i - \boldsymbol{x}_j)}{\rho_i \rho_j} \boldsymbol{u}_{ij}. \tag{3.29}$$

This expression conserves linear momentum, but not angular momentum, Colagrossi et al. (2011). Both formulations in sections 3.27 and 3.6.2 have been implemented in the present work, and the results show not

much difference. We prefer to use the laminar viscosity term, due to its natural relationship with the physical viscosity.

3.7 Boundary Conditions

In SPH, the kernel is truncated near the boundaries (see Figure 3.5) and to complete the kernel in these regions introducing a set of particles on the boundary with some conditions is required. There are some different

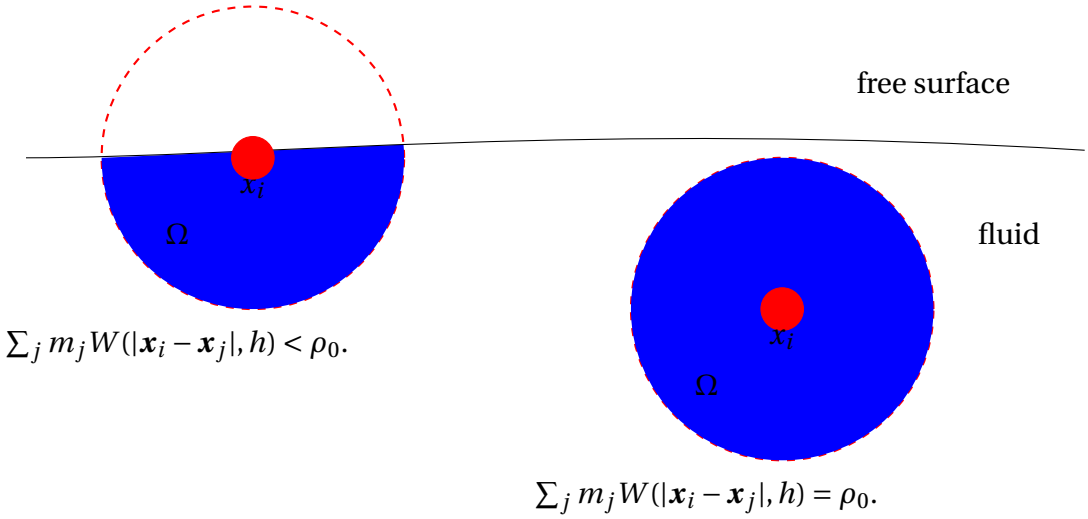

Figure 3.5: Configurations of the kernel support domain inside the fluid and near the boundary.

choices:

- Repulsive forces, Monaghan (1994).
- Dummy particles, Koshizuka et al. (1998) and Gotoh & Sakai (1999); Shao & Lo (2003); Lee et al. (2008*a*).
- Ghost particles, Libersky et al. (1993); Takeda et al. (1994); Cummins & Rudman (1999).

- Boundary integrals, Kulasegaram et al. (2004), Ferrand et al. (2013).

3.7.1 Repulsive forces

Repulsive particles were used by Monaghan (1994) in order to create no-slip boundary conditions. The particles on a wall exert a repulsive force from fluid particles (see Figure 3.6). In this boundary condition, we solve equations of motions with fixed position and zero velocity. Additionally, this model is computationally not expensive and is simple to implement. A disadvantage of this method is that the location of the boundary can be specified only approximately.

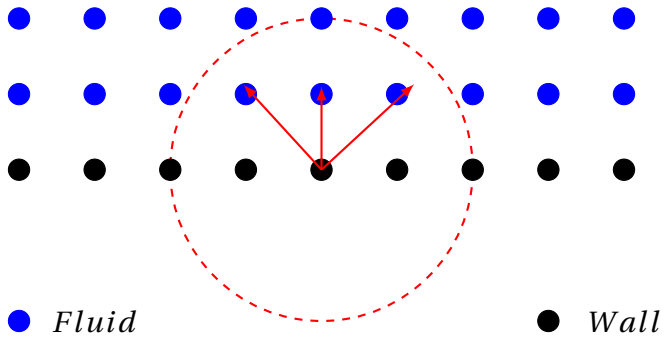

Figure 3.6: The implementation of repulsive boundary.

3.7.2 Fixed dummy particles

Here, the implementation of boundary conditions is done with the introduction of fixed dummy particles. We use two lines of dummy particles and one line of wall particles, Koshizuka et al. (1998), Gotoh & Sakai (1999), Shao & Lo (2003), Crespo et al. (2007) and Lee et al. (2008*a*). The momentum equation is not solved for them. It means that $\boldsymbol{u}$ is fixed for

these particles. Two methods have been used for dummy particle density and pressure. These are discussed in Chapter 5.

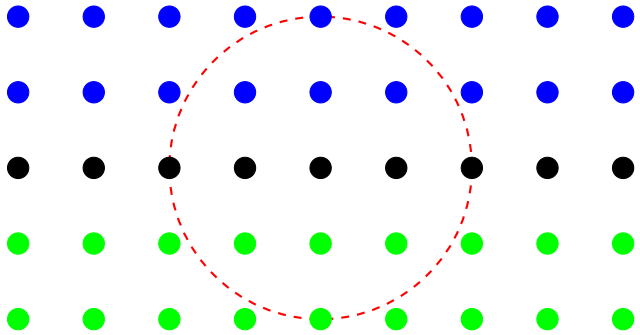

Figure 3.7: The implementation of dummy boundary.

3.7.3 Ghost or Mirror particles

Ghost particles were introduced by Randles & Libersky (1996) in order to respect a no-slip condition at the same time that the kernel is not truncated. For no-slip wall, when the fluid particle is close to a boundary for a distance less than smoothing length h, a new particle is generated with the same density and pressure, but with opposite velocity. Figure 3.8 shows the procedure for a horizontal wall moving vertically with speed v_w.

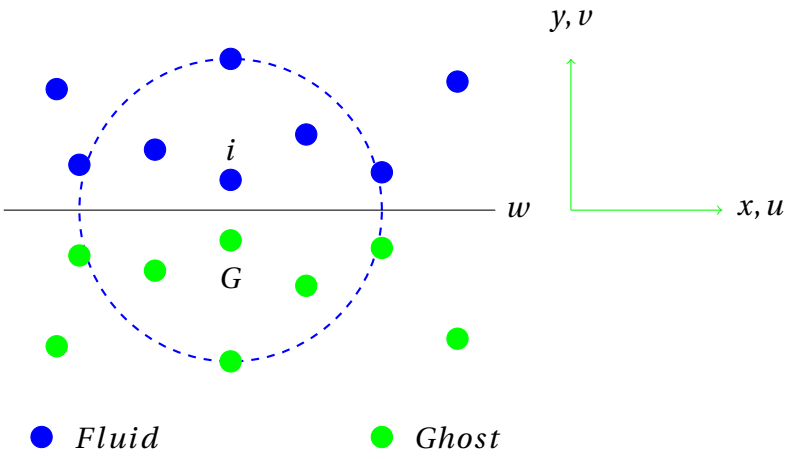

Figure 3.8: The implementation of ghost boundary.

$$x_{iG} = x_i$$

$$y_{iG} = 2y_w - y_i$$

$$v_{iG} = 2v_w - v_i$$

$$u_{iG} = -u_i$$

$$\rho_{iG} = \rho_i$$

$$p_{iG} = p_i$$

where u and v are the tangential and normal velocity to the wall boundary, respectively. Ghost particles also allow us to specify slip conditions at walls, in which case the above relations can modified by setting $u_{iG} = +u_i$.

3.7.4 Boundary integrals

In the boundary integral method, the missing area of kernel support near the wall is replaced by a surface integral and re-normalization is based upon a variation formulation introduced by Kulasegaram et al. (2004).

3.8 Tensile Instability

This clumping of SPH particles is unphysical. When the distance between two particles decreases, the repulsive force between them must increase. For this reason, to remove the instability, a repulsive force can be introduced.

In this study, an artificial pressure was tested for the dam-break case, Monaghan (2000) and Dehnen & Aly (2012). The repulsive force is added to the momentum equation, which becomes:

$$\frac{D\boldsymbol{u}_i}{Dt} = -\sum_j^N m_j(p_j + p_i + RB_{ij}^n + \Pi_{ij})\frac{\partial W_{ij}}{\partial \boldsymbol{x}_i} \tag{3.30}$$

The factor B_{ij}^n is called anti-clumping term. Where $B_{ij}^n = \frac{w(q)}{w(\bar{q})}$ and $\bar{q}$ is the average particle spacing divided by the smoothing length h. In this work, average particle spacing is set as a constant and taken as $\bar{q} = 0.7$ and R can be determined by relating to the pressure. In the code, we used 0.1 for negative pressure and 0.2 for positive pressure, where n is equal to 4, Monaghan (2000) and Dehnen & Aly (2012). The cubic spline function is used here. Figure 3.10 is without anti-clumping term and Figure 3.9 shows the result with anti-clumping term. When the anti-clumping term is employed, the space between the particles more evenly distributed than without it.

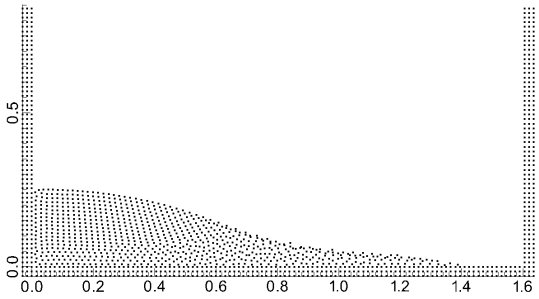

Figure 3.9: Simulation of dam break with anti-clumping term .

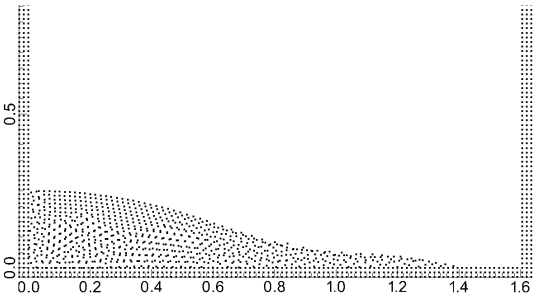

Figure 3.10: Simulation of dam break without anti-clumping term.

3.8.1 Mixed Kernel Gradient Correction

Bonet & Lok (1999) presented a correction method to preserve the angular momentum in gradient or divergence operators. The mixed-gradient correction is obtained by multiplication of the mixed gradient correction with the inverse of correction matrix. The corrected gradient of the corrected kernel is given by:

$$\widetilde{\nabla \widetilde{W_{ij}}}(\boldsymbol{x}_i) = L_i \nabla \widetilde{W_{ij}}(\boldsymbol{x}_i) \tag{3.31}$$

where the constant kernel correction is:

$$\widetilde{W_{ij}}(\boldsymbol{x}_i) = \frac{W_{ij}(\boldsymbol{x}_i)}{\sum_{j=1}^{N} \frac{m_j}{\rho_j} w_{ij}(\boldsymbol{x}_i)} \tag{3.32}$$

The gradient of the corrected kernel is shown as:

$$\nabla \widetilde{W_{ij}}(\boldsymbol{x}_i) = \frac{\nabla W_{ij}(\boldsymbol{x}_i) - \frac{\sum_{j=1}^{N} \frac{m_j}{\rho_j} \nabla W_{ij}(\boldsymbol{x}_i)}{\sum_{j=1}^{N} \frac{m_j}{\rho_j} W_{ij}(\boldsymbol{x}_i)}}{\sum_{j=1}^{N} \frac{m_j}{\rho_j} W_{ij}(\boldsymbol{x}_i)} \tag{3.33}$$

The SPH equation 3.22 and 3.19 can be rewritten as

$$\frac{D\rho_i}{Dt} = \sum_j m_j(\boldsymbol{v}_i - \boldsymbol{v}_j).L_i\widetilde{\nabla}_i\widetilde{W_{ij}}(\boldsymbol{x}_i) \tag{3.34}$$

$$\frac{D\boldsymbol{u}_i}{Dt} = \boldsymbol{f}_i - \sum_j \frac{m_j}{\rho_i\rho_j}(p_i + p_j + \Pi_{ij})\boldsymbol{L}_i.\widetilde{\nabla}_i\widetilde{W_{ij}}(\boldsymbol{x}_i) \tag{3.35}$$

This gradient correction was implemented in the SPH code. For the correction the inverse of a 3x3 L matrix is needed. This inverse matrix is very sensitive to the particle positions, and when the particles are close together, this matrix can be singular. We tried to run the code with further modification, without any further notification but found that small clump of particles were ejected from the tip of the dam break. Also, other particles were flying over the flow, which did not happen without the gradient correction. Some extra implementation should be made to the L matrix to get improvement when using this correction. We found out that using this correction with special extra modification made our code very expensive, especially when we used large numbers of particles. Moreover, there are no significant difference in results. We therefore do not use the correction in the following.

3.9 Time integration

In SPH we have three independent variables: ρ, $\boldsymbol{u}$ and $\boldsymbol{x}$: density, velocity and position, respectively. The pressure p is directly linked to the density and is not an independent variable (see equation 3.23). As shown in

section 3.1, there are three differential equations that must be evaluated in time:

$$a(t) = \frac{D\boldsymbol{u}}{Dt} = \boldsymbol{F}(\rho, \boldsymbol{u}, \boldsymbol{x}), \tag{3.36}$$

$$\frac{D\rho}{Dt} = D(\boldsymbol{u}, \boldsymbol{x}), \tag{3.37}$$

$$\frac{D\boldsymbol{x}}{Dt} = \boldsymbol{u}. \tag{3.38}$$

In this work three different time integration methods are used:

- Euler scheme time integration
- Predictor Corrector scheme time integration
- Verlet scheme time integration

Euler Scheme

In this model, we apply an Euler time stepping scheme. First, we update the velocity:

$$\boldsymbol{u}_{(t+dt)} = \boldsymbol{u}_{(t)} + \boldsymbol{a}_{(t)} dt,$$

Second, the positions use the results from the velocity update to predict the new position:

$$\boldsymbol{x}_{(t+dt)} = \boldsymbol{x}_{(t)} + \boldsymbol{u}_{(t)} dt.$$

Predictor-Corrector Scheme

Using predictor-corrector time integration with predictors for velocity, density and position at intermediate time steps, the differential equations are evaluated in time as:

$$\boldsymbol{u}_i^{n+\frac{1}{2}} = \boldsymbol{u}_i^n + \frac{dt}{2}\boldsymbol{F}_i^n$$

$$\rho_i^{n+\frac{1}{2}} = \rho_i^n + \frac{dt}{2}D_i^n$$

$$\boldsymbol{x}_i^{n+\frac{1}{2}} = \boldsymbol{x}_i^n + \frac{dt}{2}\boldsymbol{u}_i^n$$

calculating $p_i^{n+\frac{1}{2}} = f(\rho^{n+\frac{1}{2}})$ according to Equation 3.23. These values are corrected using forces at the half step:

$$\boldsymbol{u}_i^{n+\frac{1}{2}} = \boldsymbol{u}_i^n + \frac{dt}{2}\boldsymbol{F}_i^n(\boldsymbol{x}_i^{n+\frac{1}{2}}, \boldsymbol{u}_i^{n+\frac{1}{2}}, \rho_i^{n+\frac{1}{2}})$$

$$\rho_i^{n+\frac{1}{2}} = \rho_i^n + \frac{dt}{2}D_i^n(\boldsymbol{x}_i^{n+\frac{1}{2}}, \boldsymbol{u}_i^{n+\frac{1}{2}}, \rho_i^{n+\frac{1}{2}})$$

$$\boldsymbol{x}_i^{n+\frac{1}{2}} = \boldsymbol{x}_i^n + \frac{dt}{2}\boldsymbol{u}_i^{n+\frac{1}{2}}$$

Finally, the value is calculated at the end of time step following:

$$\boldsymbol{u}_i^{n+1} = 2\boldsymbol{u}_i^{n+\frac{1}{2}} - \boldsymbol{u}_i^n,$$

$$\rho_i^{n+1} = 2\rho_i^{n+\frac{1}{2}} - \rho_i^n,$$

$$\boldsymbol{x}_i^{n+1} = 2\boldsymbol{x}_i^{n+\frac{1}{2}} - \boldsymbol{x}_i^n$$

and then the pressure is calculated from density using Eq. 3.23.

Verlet Scheme time integration

This time stepping scheme, Verlet (1967) , is divided into two parts. Firstly, variables are evaluated according to

$$\boldsymbol{u}_i^{n+1} = \boldsymbol{u}_i^{n-1} + 2dt\boldsymbol{F}_i^n,$$

$$\rho_i^{n+1} = \rho_i^{n-1} + 2dtD_i^n,$$

$$\boldsymbol{x}_i^n = \boldsymbol{x}_i^n + 2dt\boldsymbol{u}_i^n + \frac{1}{2}dt^2\boldsymbol{F}_i^n.$$

Once every M time step, we replac the second-order Verlet method by a first-order Verlet method to ensure stability, Dalrymple & Rogers (2006). Variables are calculated according to

$$\boldsymbol{u}_i^{n+1} = \boldsymbol{u}_i^n + dt\boldsymbol{F}_i^n,$$

$$\rho_i^{n+1} = \rho_i^n + dtD_i^n,$$

$$\boldsymbol{x}_i^{n+1} = \boldsymbol{x}_i^n + dt\boldsymbol{u}_i^n.$$

In other SPH simulations such as the dam break and bubble rising through water, we tried time stepping algorithms such as Verlet and predictor-corrector, but did not find much difference in accuracy in the simulations compared to the Euler time stepping scheme. However, they make the code slower, so we prefer to use Euler in the following.

3.9.1 Time step

The time step in WCSPH method is typically chosen based on the following limitations:

- Courant-Friedrichs-Lewy (CFL) condition;
- Condition of the viscous diffusion;
- Condition on speed of sound.

All these three time-steps constraints were used by Lee et al. (2008*a*) in truly incompressible SPH method. In this work, all the above conditions are considered as time step criteria:

Courant-Friedrichs-Lewy (CFL) condition:

The CFL condition is written as

$$\Delta t_{CFL} \leq \sigma (dx) / u,$$

where σ is a constant, and here it is equal to 0.25; dx is the initial particle spacing.

Condition of the viscous diffusion:

The viscous diffusion condition is

$$\Delta t_{\upsilon} \leq \beta (dx)^2 / \upsilon,$$

where β is a constant , and here it is set as 0.25, υ is kinematic viscosity.

Speed of sound condition:

$$\Delta t_c \leq \alpha(dx)/c,$$

where α is a constant and here it is set as 0.25 and c is speed of sound. The time step is chosen as the minimum among the three conditions.

The basic procedure of time step method is: at the end of any step t, the velocity, acceleration and density at a particle position are updated in each full time step.

3.10 Summary of Formulation

In this chapter, the model and the SPH formulation that will be employed in this work have been introduced. The Colagrossi & Landrini (2003) formulation for the simulation of multiphase flows will be used. The evolved density, Monaghan (1992), the equation of state (Monaghan (1994)), laminar viscosity Morris et al. (1997) and Shepard filter (zeroth order density re-normalization) will be used. In subsequent chapters, both dummy and ghost boundary conditions are tested. A simple Euler time-stepping scheme is used.

CHAPTER 4

SPH ON MESSAGE PASSING INTERFACE (MPI) (CODE)

Contents

4.1 General philosophy of SPH parallelisation

Due to interactions between many particles, a large number of calculations is required to run the model. When we simulate multi-phase flow, the number of particles will be naturally increased. Therefore, to simulate large cases, we need a program to accelerate our code and to reduce computational time and to use large numbers of particles. We need a

parallelised program.

One of the important part of the parallel code is domain decomposition, Guo et al. (2013), when the simulation domain is divided into subdomain and each subdomain in parallel calculates the solution. Exchanging of data takes place at each time step. At the start of each time step, each processor during the link list creation looks to find which particle should be moved to another processor and vice versa. This search take place only for those particles within a distance of 2h of the domain. Then the new updated particle will be moved and removed from processors as necessary. Here, a simple 1-dimensional domain decomposition method is used, where the flow domain is divided into slices in the x-direction.

There are two different type scaling to measure the performance code: strong and weak scaling. Strong scaling $S(N)$ shows how the computation time T changes with increasing the number of processors N when the total problem size stays the same. Weak scaling $s(N)$ indicates how the solution time changes with the number of processors for fixed problem size per processor. The achieved speedups will be shown later, analyzing the strong scaling.

The simulation was carried at using, 36 Viglen HX425T2i HPC 2U Compute Nodes, equipped with Dual Intel Xeon E5650 (Westmere) Six Core 2.66GHz processors and 12 GB of memory per motherboard.

Some of the computations in Chapters Six, Seven and Eight require millions of particles. This is not possible on serial machines and parallel

code is required. In this chapter the structure of our Message Passing Interface (MPI) code for a 2D and 3D single and multi-phase SPH is presented. Both 2D and 3D code.

4.2 Code Structure

In our parallel SPH code, the code consists of seven major steps:

Step 1: Define geometry and initial conditions.

Step 2: Create the boundary ghost particles.

Step 3: Find the shared boundary between processors see Figure 4.1.

Step 4: Send and receive share boundary data between processors $n-1$, n and $n+1$, each processor has a left and right processor's neighbour only first and last processor have no left and right neighbours, respectively. See Figure 4.2.

Step 5: Create the particle neighbours link list.

Step 6: Calculate particles interactions.

Step 7: Update variables at the end of the time steps.

Step 8: Add or remove particles between processors.

Steps are detailed in the following.

Step 1: Define geometry and initial conditions of the SPH simulations to be executed. Also define parameters such as the SPH formulation to be used like density renormalization.

Step 2: Create the boundary ghost particles: After sharing the inner part of domain between processors, we need to create the ghost particles for each processor domain. The ghost particles will be updated each time step.

Step 3: In the SPH method, to calculate quantities like density, pressure for particle i requires information from the neighbouring particles j located on next or previous neighbouring processors, see Figure 4.1. Here, in each processor we divide the domain in to two separate parts, the inner and outer parts which will be updated each time step. Note that each particle in each time step is changing its location. The inner part is available for both processors. We need to make sure the neighbouring process has access to the correct time step data.

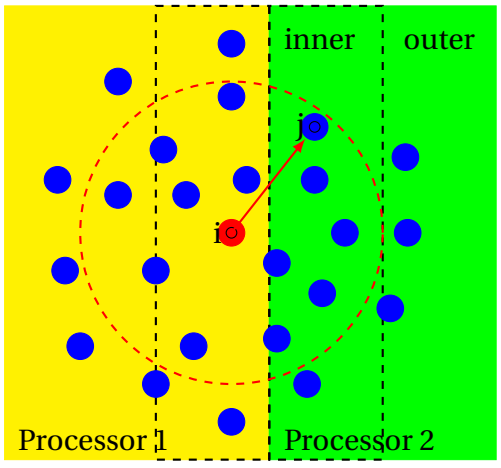

Figure 4.1: The domain divided between two processors.

Step 4: Send and receive share boundary particles between processors $n-1$ (left), n (centre) and $n+1$ (right), see Figure 4.2. After dedi-

cating shared particles between processors, we need to send or receive the data of particles to the next or from previous processors.

Step 5: Creation of the particle neighbours link list: to reduce the computational time in SPH, only the interaction of those neighbouring particles inside the kernel support will be calculated. In the SPH method, each particle will be updated each time step and can change its position on each time step. Its neighbouring particles need to be found. An efficient way to search for neighbouring particles is to employ a link list method, Monaghan & Lattanzio (1985). We divide the domain into an Cartesian network of cells of side kh where $k = 1.3$. The particles in each cell only interact with particles in the neighbouring cells, see Figure 4.3.

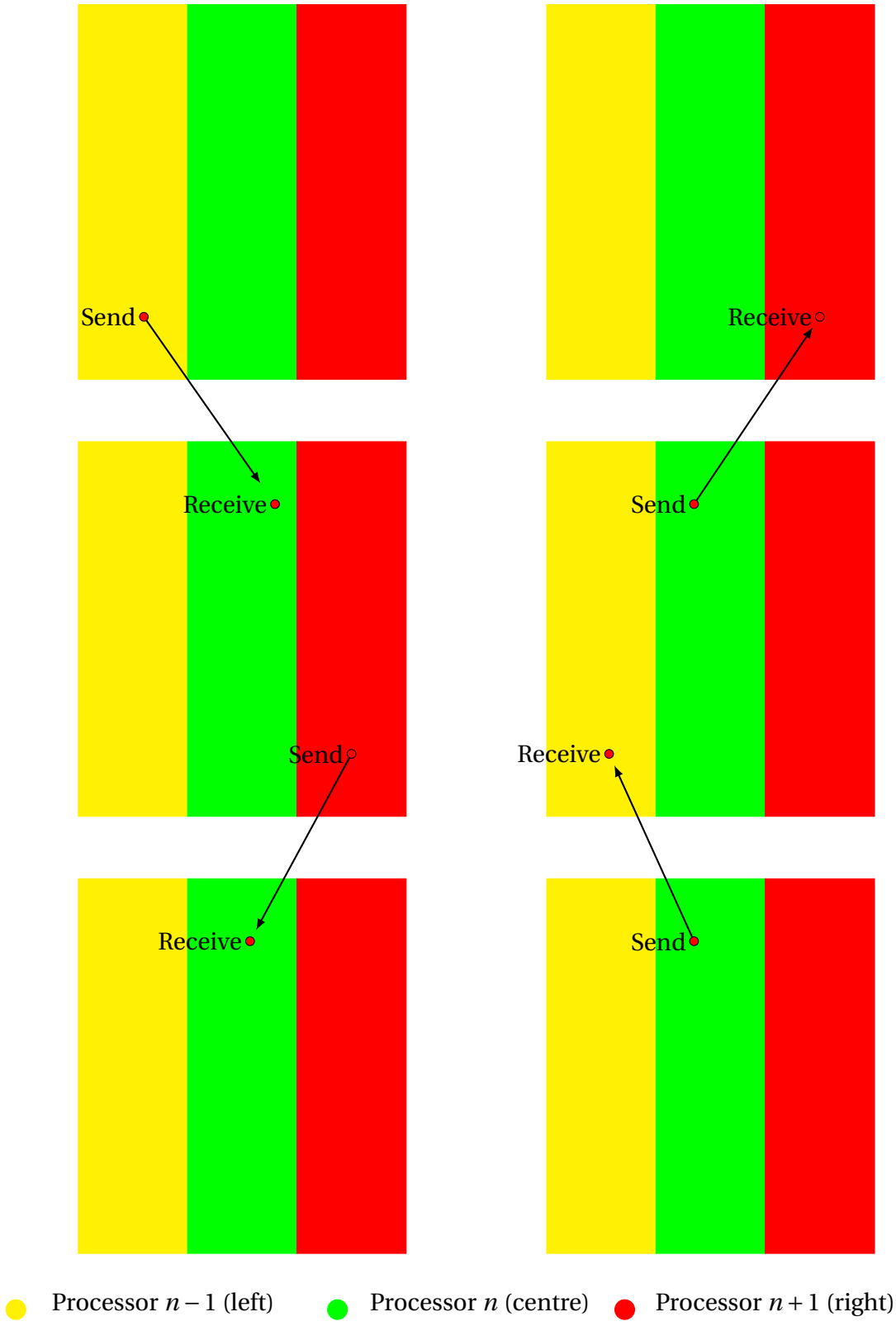

Figure 4.2: The domain divided between three processors and steps of sending and receiving data of particles to the next or from previous processors.

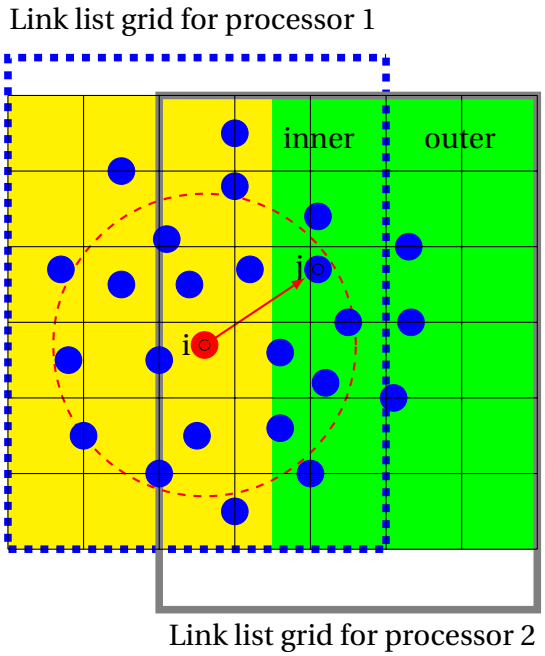

Figure 4.3: Link list algorithm grid for 2D. Cells enclosed by black solid rectangle and dash rectangle are handled by the same processors.

Step 6: Calculate particle interactions: In this step, we need to make sure for those particles are located on inner part of neighbouring processors, the particle quantity and link list should be updated for the same time steps.

Step 7: Update variable at the end of the time steps: At the end of each time step, the velocity, acceleration and then position will be updated.

Step 8: Add or remove particles migration between processors: In SPH the particles can move on each time step. Particles located on the inner part may be required to move to the next processor or previous processor. In this case, we need to add or remove those particles from its processor with the same particle ID.

4.3 Load balancing

Load balancing between processors is very important in reducing the computational time. For example, in the single-phase dam break, all particles are located at the left side of domain and the right side is empty. During the simulation fluid particles will be moved forward or backward. In this case we need to reduce the computational time and loading balance should be used. On the other hand, in the multi-phase simulation where the fluid and air particles will cover the whole domain, the loading balance does not affect the computational time.

4.4 Test Cases

We use a dam-break case to investigate the speed up of the parallel for single- and multi-phase code. In order to show the performance of our code, the speed-up is calculated by:

$$Speedup = \frac{T_{REF}}{T_N}$$

where T_{REF} is the total computational time for reference run code and T_N is the total computational time by employing N processors.

4.4.1 Dam break Cases

Dry bed 2D

Figures 4.4, 4.5 and 4.6 show the particles are divided between the different processors for three different time steps and coloured according

to their processor. Each processor computes the interaction between particles separately and the shared boundary region needs to get some information from the neighbouring processors. Comparing the results of the 2D dam break case simulation for 8 different numbers of processors is shown in Figure 4.7. Figure 4.7 and 4.8 illustrate the speed up and efficiency for 370000 particles using up to 60 processors analysing the strong scaling. The formula used to measure the efficiency is $E(N) = S(N)/N$ where $S(N)$ and N are strong scaling and number of processors, receptively. The results show that by increasing the number of processors, the speed up increases. Speeding up is not linear, due to communications between processors and particle interactions increasing, but is in general good. The efficiency decreases as the number of processors increase until $N = 10$. After that it increases at $N = 15$. Then it continues to decrease due to more processors involved. Thus the parallel code gives significant computational time saving by increasing the number of processors.

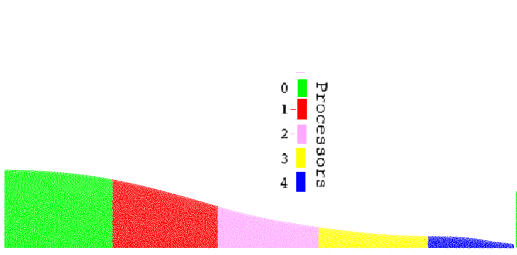

Figure 4.4: Particle distribution between processors before impacting the wall.

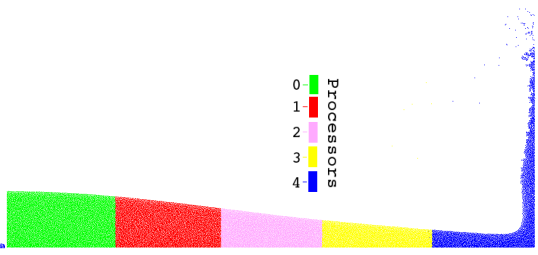

Figure 4.5: Particle distribution between processors during impact with the wall

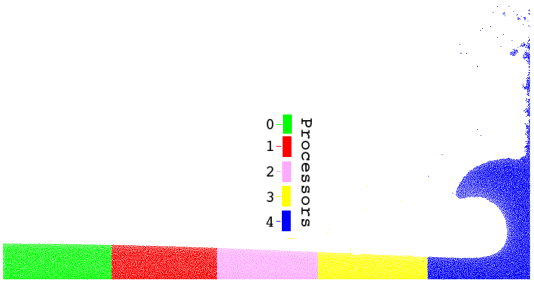

Figure 4.6: Particle distribution between processors after impact.

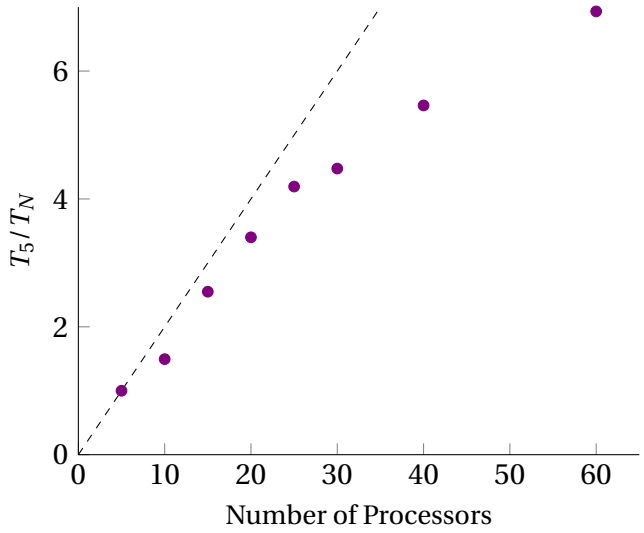

Figure 4.7: Runtime of a collapsing water column $W = 2H, D = 5.366H$, for three different numbers of processors, for 370000 particles.

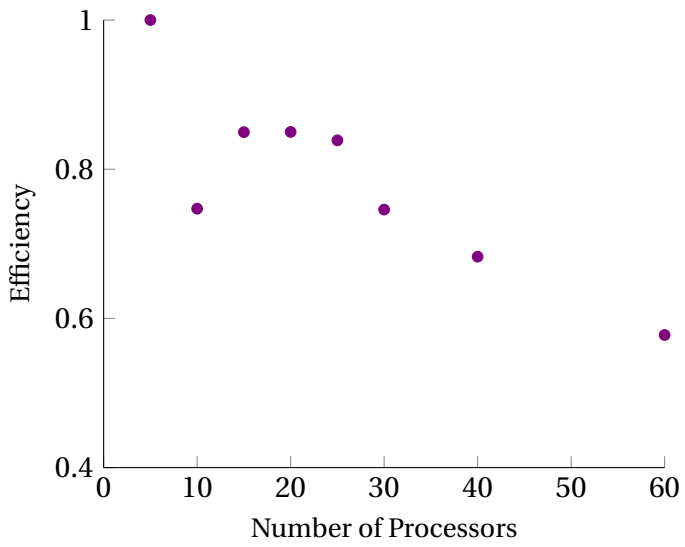

Figure 4.8: The efficiency obtained for a calculation involved 370000 particles, from 5 to 60 processors.

Rising bubble

Particles are coloured by their processor numbers in x-direction for 216000 particles in Figures 4.9. The Figure 4.10 shows the pressure fields for rising bubble through the water and shows the pressure at the interface between processors is smooth and the information is passed between processors correctly.

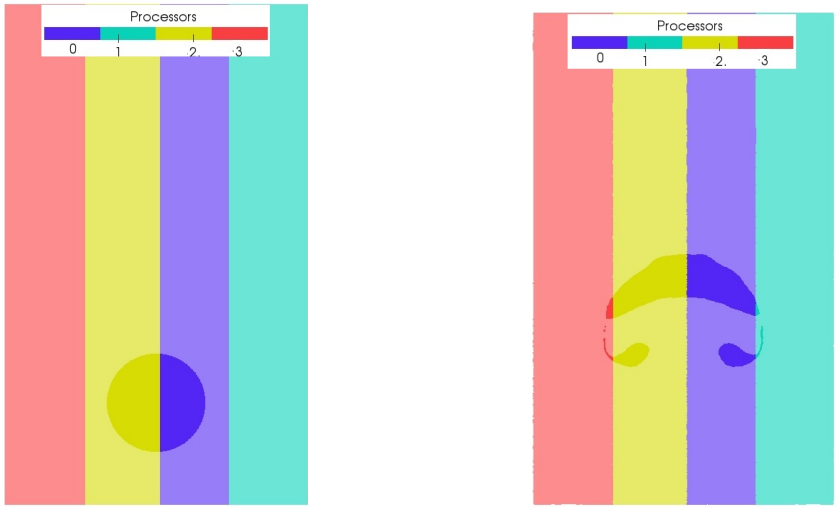

Figure 4.9: Particle distribution between processors before and during rising bubble.

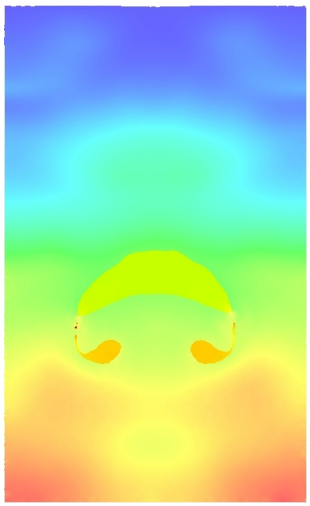

Figure 4.10: Particle distribution between processors for bubble rising and colors represent pressure fields and shows the pressure at the interface between processors is smoothed.

Dry bed 3D

In Figures 4.11 and 4.12, particles are coloured by their processors numbers in x-direction for 3 million particles. As shown in Figure 4.13, the computational time is decreasing as the number of processors is increasing. Figure 4.14 shows the efficiency decreases as the number of processors increase until $N = 30$. After that it raises with increasing number of processes.

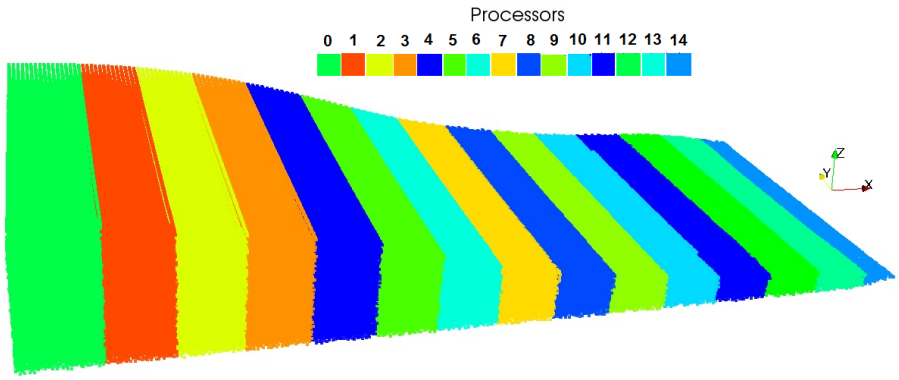

Figure 4.11: Particle distribution between processors before impact the wall.

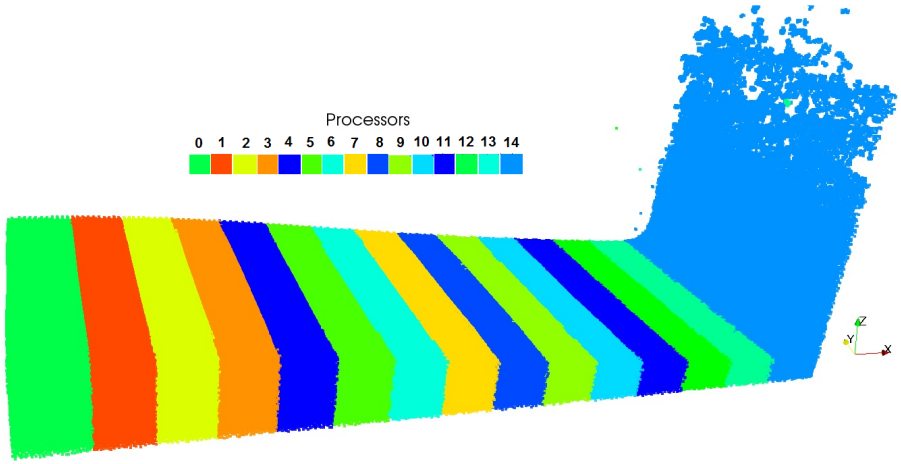

Figure 4.12: Particle distribution between processors during the impact.

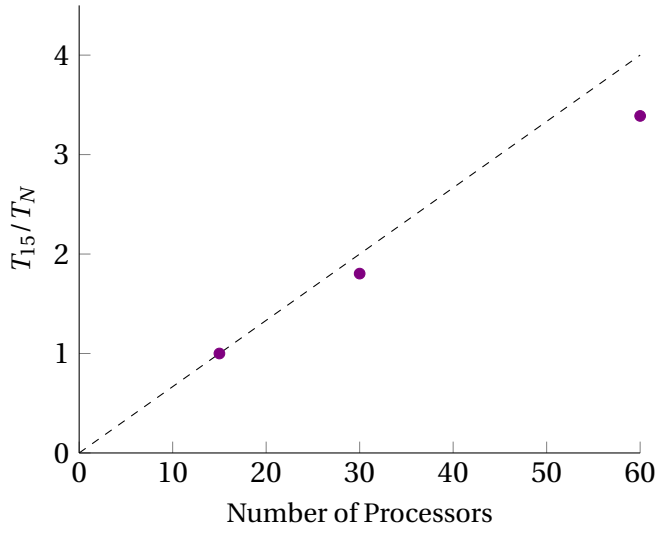

Figure 4.13: Speedup for collapsing water column $W = 2H, L = W$ and $D = 5.366H$, for three different numbers of processors for 3 million particles.

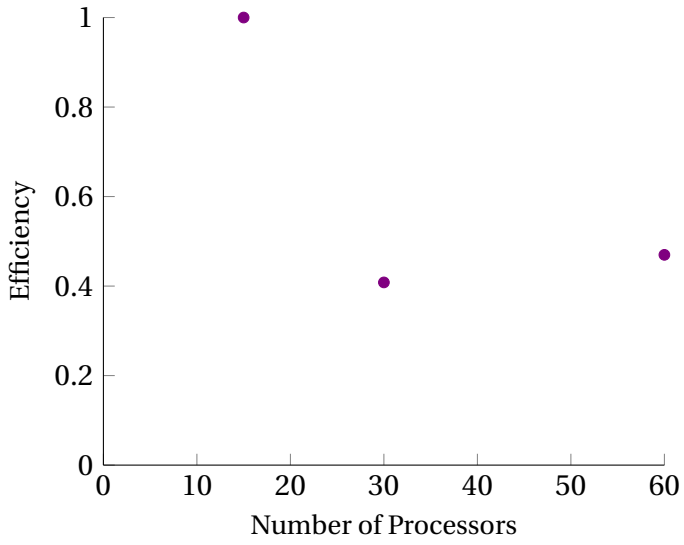

Figure 4.14: The efficiency obtained for a calculation involved 3 million particles, from 15 to 60 processors.

4.5 Conclusion

This chapter presented the details of parallel SPH and how the MPI parallel code can handle a large number of particles. The speed up of MPI parallel code was reported for two test cases for 2D and 3D dam-break cases. Linear speedup is not achieved, due to extra communications and particle interactions between processors. The efficiency decreased and then increased, how ever, it continues to decrease when more processors involved.

2D bubble rising was shown to illustrate pressure smooth information. Results are passed between processors correctly. The comparison between speed up and number of processors showed reasonable agreement for the reference total computational run time. The efficiency decreased then increased with increasing number of processors.

CHAPTER 5

VALIDATIONS: TWO DIMENSIONAL CASES

Contents

5.1 Two-Dimensional Cases Single Phase

In this section, we use SPH for simulations of two clasic CFD test cases: the dam-break and lid-driven cavity. The aim is to test the effectiveness of the various methods available to specify the SPH model including choice of kernel, boundary conditions and density and pressure smoothing.Computations will be compared with standard results from literature.

5.1.1 Preliminary Investigations

In this section, two different methods of dummy particles are tested and compared with no-slip ghost boundary with Neumann boundary condition, $dp/dn = 0$.

Method A: setting reference density for dummy particles during simulation and the same pressure of wall particle is set for dummy particles. But for bottom wall particles hydrostatic pressure is implemented, i.e. $p_{dummy} = p_{fluid} + \rho g(h_{fluid} - h_{dummy})$. This model is represented in Figures 5.1 and 5.2. Another technique is the same wall properties are set to

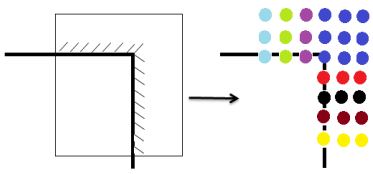

Figure 5.1: The implementation of wall pressure condition.

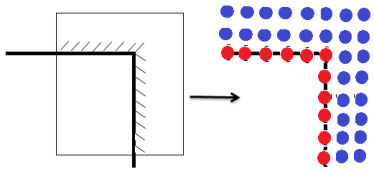

Figure 5.2: The implementation of density boundary condition.

the dummy particles, Figure 5.3 and 5.4 illustrate this method. In both models, the wall and dummy particle densities are renormalised every 15 time steps, Hughes & Graham (2010).

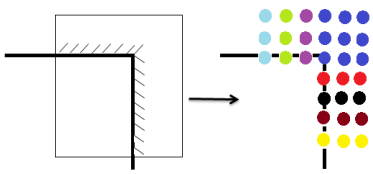

Figure 5.3: The implementation of wall pressure condition.

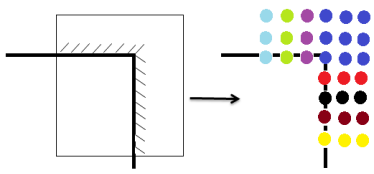

Figure 5.4: The implementation of density boundary condition.

Influence of Different Boundary

Figure 5.5 shows the result of the method A boundary condition at $(t(g/H)^{1/2} = 2)$. During the computation, the simulation will keep the promising hydrostatic pressure. In some positions, however the particles are clumping in the second boundary conditions. For method B, wall particles push fluid particles away from the boundary. This is not physical and this model will not keep hydrostatic pressure during the computation of simulation (see Figure 5.6).

Figure 5.7 shows the time variations of pressure results at P_1 and P_2 located $y/H = 0.19$ above the horizontal bed and the mid-tank and left wall, respectively. The pressure result is interpolated on these positions P_1 and P_2 using the SPH sum kernel. In comparison, the pressure oscillations of the method A of boundary is much less than this computed by the method B of boundary for measurement points, especially at P_1. The large pressure oscillations are observed in Figure 5.7, where the measurement point is located at the solid boundary.

In comparison, the pressure oscillations of method A of boundary are much less than this computed by the method B of boundary for measurement points, especially at P_1. Therefore we use method A in the following.

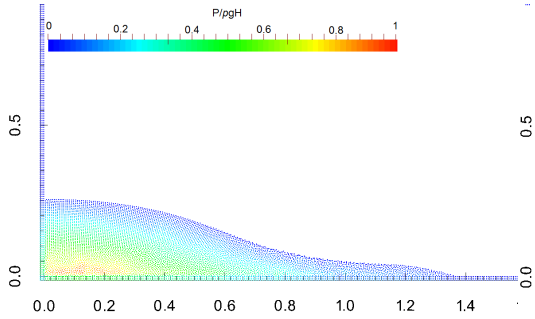

Figure 5.5: Influence of type A of boundary.

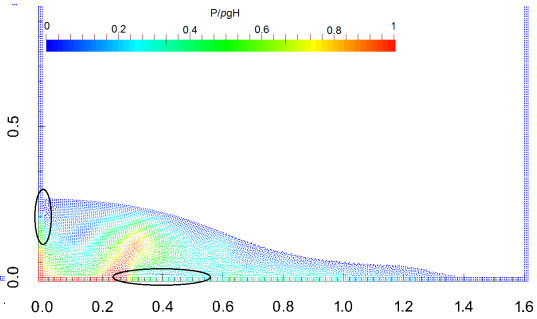

Figure 5.6: Influence of type B of boundary.

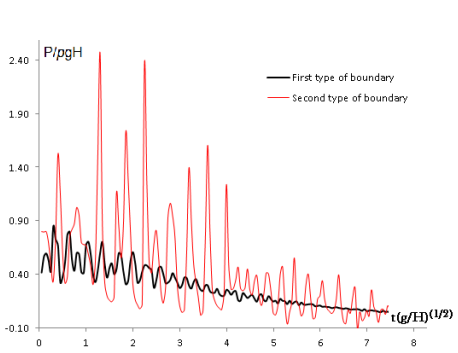

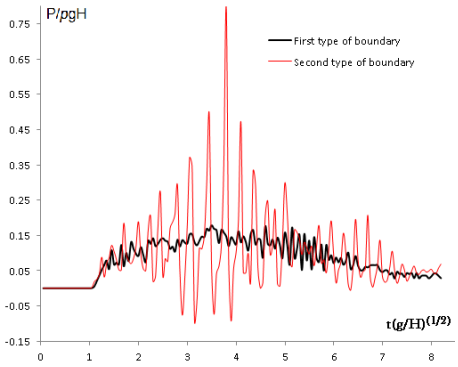

Figure 5.7: Time variation of pressure: The comparisons between type A (left) and type B (right) of boundary methods, at the position(a): $P_1(0, 0.057)$ and (b): $P_2(0.801, 0.057)$.

5.1.2 Dam break dry Bed

In this section, two test cases which are performed in other literature, Colagrossi & Landrini (2003), Crespo et al. (2008) and Adami et al. (2012) will be tested for two different boundary conditions and the results of the simulation will be compared with other numerical results and the experimental data of Martin & Moyce (1952). In the experimental case, a water column is initially held in place by a lock gate. The gate is moved up and the water held behind the gate is released and moves under the effect of gravity.

The configuration is shown in Figure 5.8 and the dimensions for each

case are dependent on the height of fluid. The water column is set with height H and width W inside a computational tank of height H_{wall} height and width D. The water column starts collapsing due to gravity and moves over to the vertical bottom wall towards the right side of the tank.

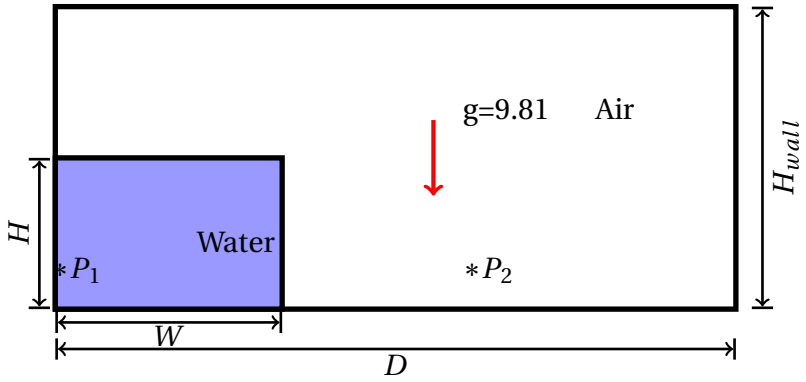

Figure 5.8: Configuration of dam break.

First case with $W = 2H, D = 5.366H$

We study the front propagation of a dam break of dimensions $L = 2H$, $D = 5.366H$. In this case, we use two different boundary conditions, with a grid resolution of $dx = 0.003$. Total number of 20000 fluid particles were used and the time step is set $\Delta t = 0.4174 \times 10^{-4}$.

The geometry of the dam break is shown in Figure 5.8 with dimensions of H_{wall}, H, D and W defined as the wall and water height and wall and water width are equal to 1, 0.3, 1.6 and 0.6, respectively, and the initial pressure field of water is set to hydrostatic pressure. All particles have the same initial spacing dx. The fluid density ρ and kinematic viscosity ν are 1000 $\mathrm{kg\,s^{-2}}$ and 1.0×10^{-6} $\mathrm{m^2\,s^{-1}}$, respectively. Under the action of

gravity, the water falls down, and gravity is taken as g= 9.81 $\mathrm{m\,s^{-2}}$. No-slip boundary conditions are applied.

The position of the simulation particles for different boundary conditions at various times is shown in Figure 5.9. First the water is squeezed out at the right bottom of the column forming a 'jet', then the top right of the column starts to move down. The fluid front is sharp. The fluid surface stays smooth during the simulation. The location of the front of the jet is compared with that from SPH results produced by Adami et al. (2012), (see Figure 5.9). It is also compared with the result of Colagrossi & Landrini (2003), (see Figure 5.10). For both dummy and ghost boundaries we see good agreement with Adami et al. (2012) and Colagrossi & Landrini (2003) results.

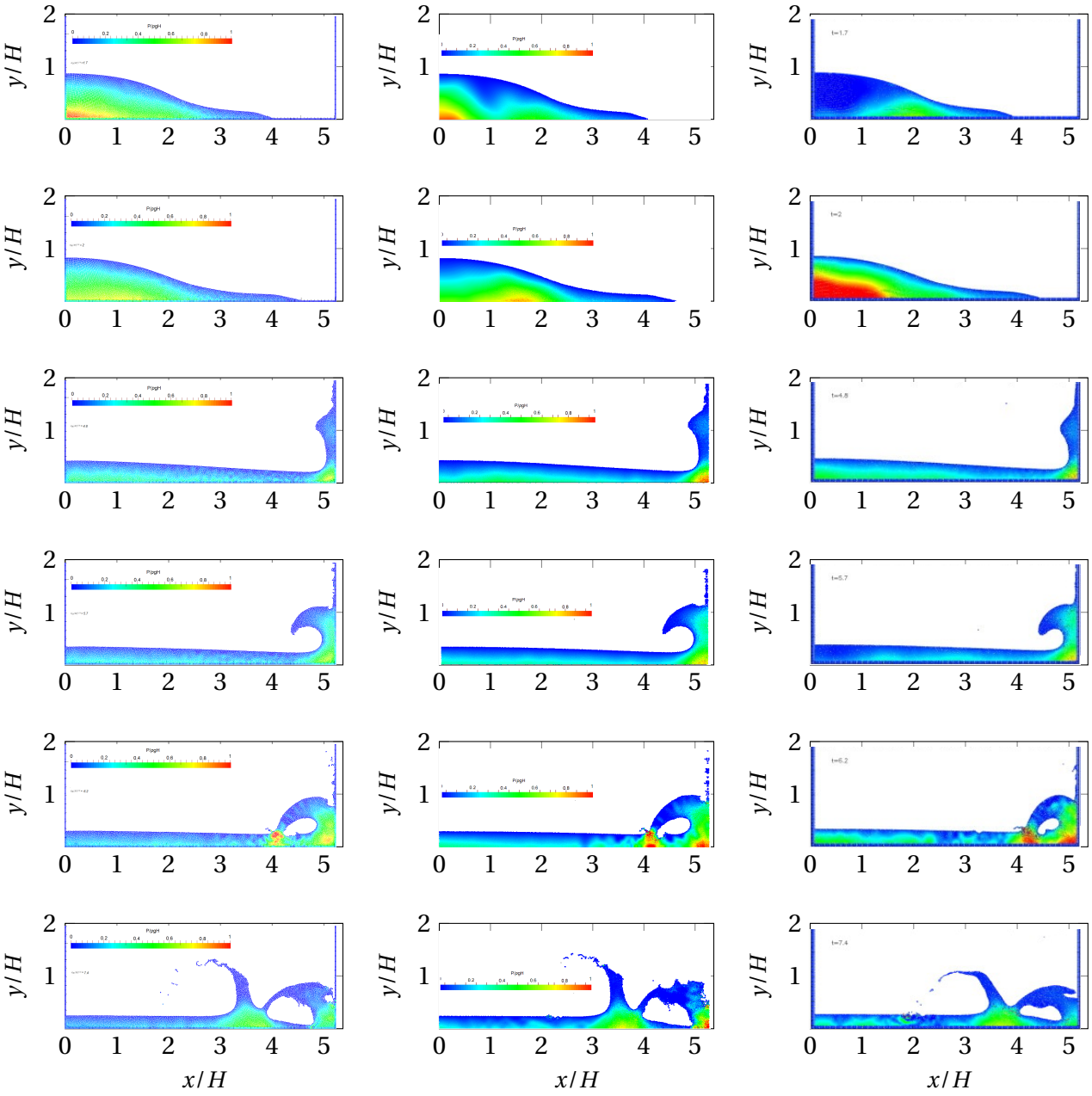

Figure 5.9: Time evaluation of the water domain after the dam breaking, using SPH method. The solution is shown at six different time steps $(t(g/H)^{1/2} = 1.7, 2, 4.8, 5.7, 6.2, 7.4)$. First and second column snapshot of the dam break simulation for 20000 particles for dummy and ghost boundary conditions, respectively, are compared with third column of snapshots of 20000 particles of Adami et al. (2012) simulation.

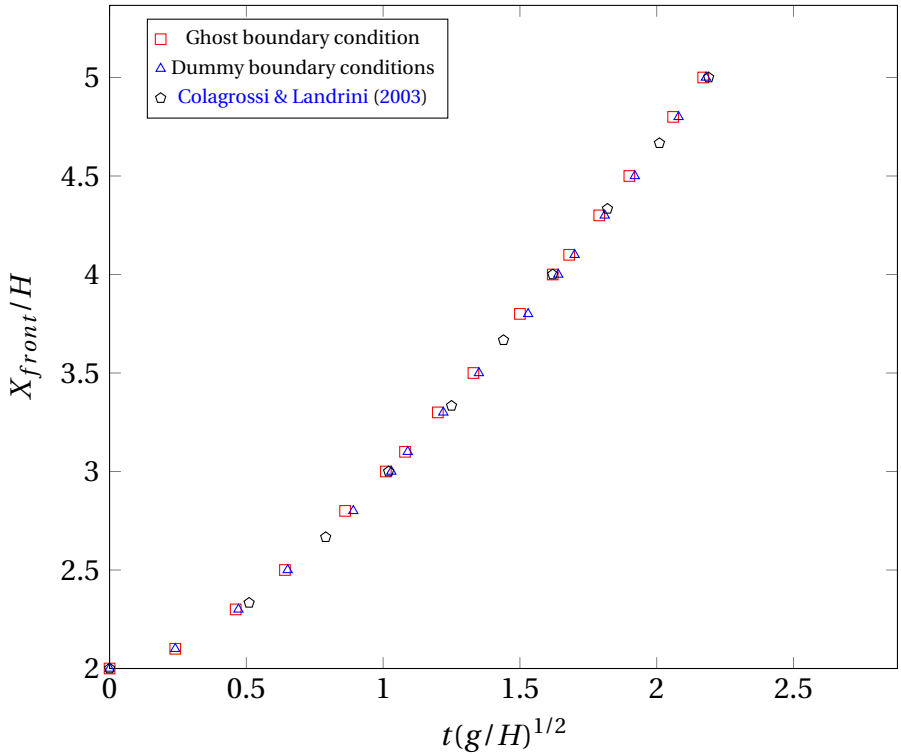

Figure 5.10: Time evaluation of the front of a collapsing water column for two different boundary conditions compared to Colagrossi & Landrini (2003).

Comparing with previous results, we get a similar roll-up after impact of the fluid on the right wall and second splash after the impact. The main difference is the pressure field after impact. We do not get a smooth pressure distribution similar to a reference hydrostatic field. At the start of the collapse there are pressure oscillations, where the maximum pressure at the wall impacts with right wall. After impact on the right wall some particles splash and fly up through the simulation, due to use the low viscosity.

We have tested the effect of the boundary condition upon the water column. The difference was pressure fluctuations in the fluid, but the overall shape and the water front were unaffected. Three different time stepping schemes have been implemented, but we found out there were

no significant differences between them. The Euler scheme is used in our subsequent simulations.

Figure 5.11 shows a comparison between our simulation results and experiments by Buchner (2002) for the pressure signal at $y/H = 0.19$ on the right wall, using the SPH sum kernel to evaluate the pressure at that point. The pressure at that point obtained with our simulation contains high frequency oscillations but the main pressure plateau is reasonably well captured.

The first peak scheme seems closer to the experiment data of Buchner (2002). The second peak, at $t(g/H)^{1/2} = 6$ is caused by the plunging wave of the first roll-up after the flow hits the right wall. The pressure increase occurs when the plunging wave closes the cavity at $t(g/H)_{1/2} = 6$. This peak occurs at a slight delay in our simulation, since the air cushion effect is not captured with a mono-fluid simulation.

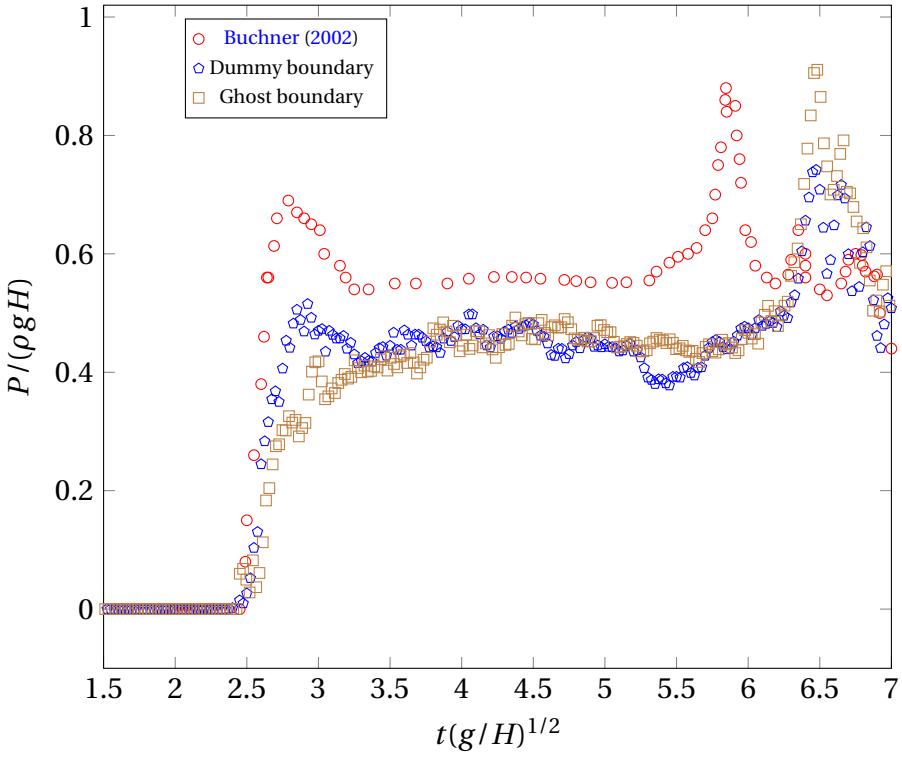

Figure 5.11: Comparison of temporal pressure profile at $y/H = 0.19$ between experimental data, Buchner (2002).

Second case with $W = H/2, D = 2H$

In the second case, the results are compared with the experimental data of Martin & Moyce (1952). In this model, W is equal to 1 and H is 2. The fluid consists of 20000 particles with particle spacing of 0.02 arranged on a box and starts to fall under the influence of gravity. 1000 $\mathrm{kg\,s^{-2}}$ and 1.0×10^{-6} $\mathrm{m^2\,s^{-1}}$ are density ρ and kinematic viscosity ν, respectively. The time step is fixed and time step size of $\Delta t = 0.11233 \times 10^{-3}$ used. The water front locations from simulations and experiments are compared in Figure 5.12. The result shows very little difference between dummy and ghost boundary conditions, but compared with the experimental data

the velocity of the tip of the fluid is higher in SPH. This could be due to the initial gate raises not being captured by the numerical scheme.

The results of the top of the fluid column at the left boundary are given in Figure 5.13. The results are very close to the experimental data of Martin & Moyce (1952).

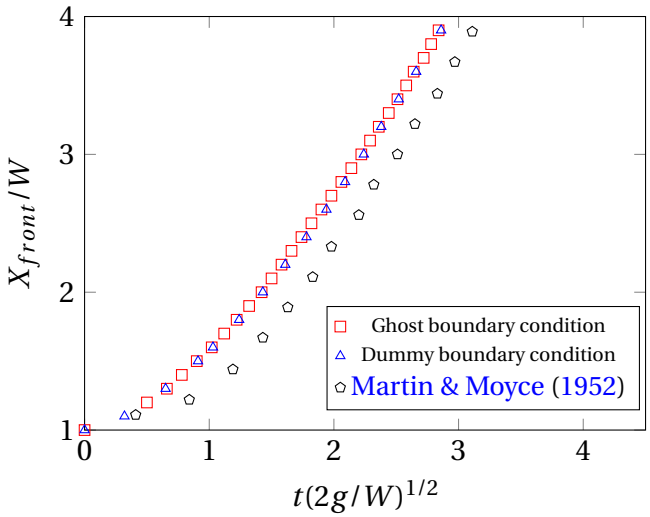

Figure 5.12: Time evaluation of the front of a collapsing water column $W = H/2, D = 2H$, for two different boundaries compared to experimental data, Martin & Moyce (1952).

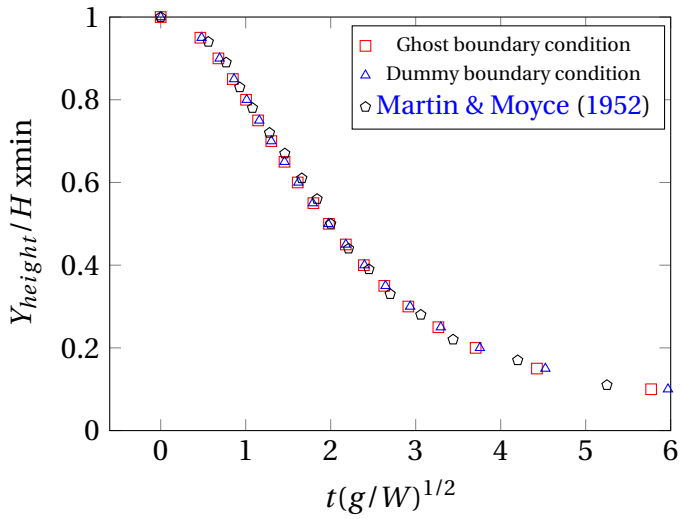

Figure 5.13: Time evaluation of the height of a collapsing water column $W = H/2, D = 2H$, for two different boundaries compared to experimental data, [Martin & Moyce (1952)].

Third case Dam-break on a wet bed

The dam break on a wet bed is another test model. This case is often implemented for testing programs. This case is based on the experiments of Jánosi et al. (2004) where the main body of water is separated from a thin water layer by a lock gate. The lock gate is placed in fixed position. The implemented domain is shown in Figure 5.14, where d_0 is the height of the water layer and d is the height of the main water body. Jánosi et al.

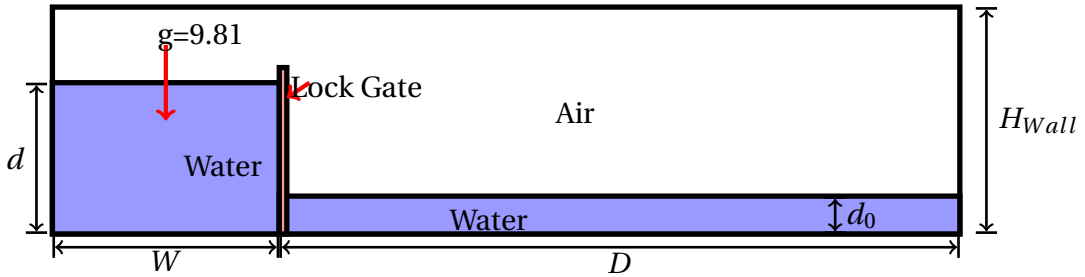

Figure 5.14: Configuration of dam break on wet bed.

(2004) proposed that at the beginning of propagation, the effect of the

side wall on the flow inside the tank is tiny, therefore the model can be simulated in a two-dimensional domain, Mokos (2014). In the previous dam-break cases, the water moves rapidly downstream. In the case of the wetted bed, interaction of the jet with the bed causes an overturning wave to be produced (see Figure 5.15) .

The lock gate will be simulated using ghost boundary condition (no-slip) particles and an initial constant velocity. In this model, the initial height of water left of the lock gate, d and fluid depth, d_0 are important. Profiles were used for $d = 0.15$ m, $d_0 = 0.018$ m and 0.38 m.

The case has been implemented with SPH by Violeau & Issa (2007), Crespo et al. (2008), Lee et al. (2008*a*), Gomez-Gesteira et al. (2010) and Mokos (2014). The gate is moved upward at time $t = 0$ with constant speed of 1.5 ms^{-1} to let water collapse into the tank. In this case, we chose initial particle spacing of 0.0025 and we used 13663 and 18206 fluid particles for $d_0 = 0.015$ mand 0.038 m, respectively. This case has been implemented with our SPH code. Figure 5.15 and 5.16 show the evaluation of the flow after the gate removal, compared with results of Violeau & Issa (2007) and experimental results Jánosi et al. (2004). The shape of the breaking dam compares reasonably well with Violeau & Issa (2007) and experiments, Jánosi et al. (2004). There is a small gap in time, about 0.069 ms, between the experimental [Jánosi et al. (2004)], and our simulation results. This could be due the influence of the gate that initially supports the water column, Shakibaeinia & Jin (2011).

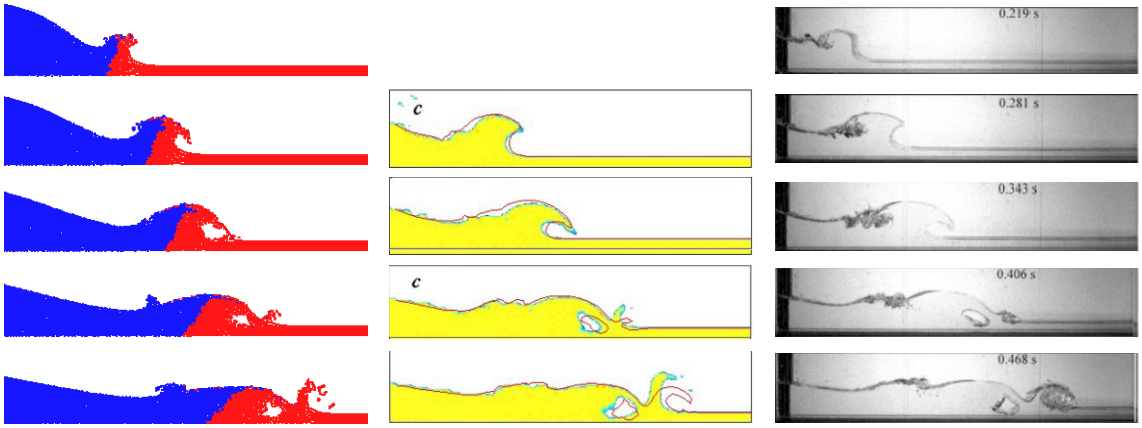

Figure 5.15: Comparison (case with $d_0 = 0.015$ m) of numerical results to the numerical results by Violeau & Issa (2007) and experimental results, [Jánosi et al. (2004)], First, second and third column, respectively. The blue and red colours represent water column and the wet bed channel water and the dotted lines mimic the experimental free surface.

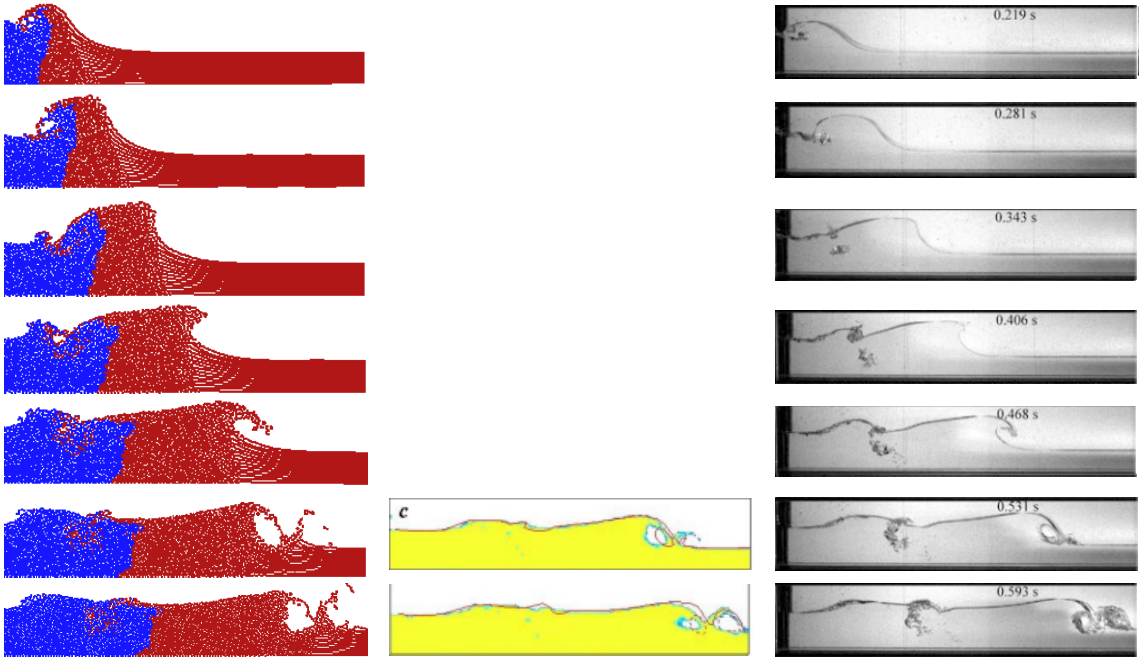

Figure 5.16: Comparison (case with $d_0 = 0.038$ m) of numerical results to the numerical results by Violeau & Issa (2007) and experimental results, [Jánosi et al. (2004)], First, second and third column, respectively. The blue and red colours represent water column and the wet bed channel water and the dotted lines mimic the experimental free surface.

5.1.3 Lid driven cavity

The lid driven cavity problem is the fluid flow within a closed square generated by moving the top side of the cavity at constant velocity u_{top} while the other three sides remains stationary and the no-slip boundary conditions are implemented. The cavity side size is L, the lid velocity and density are $u_{top} = 1$ m/s and ρ, respectively, such that the Reynolds number is defined as:

$$Re = \frac{u_{top} L}{\nu}, \tag{5.1}$$

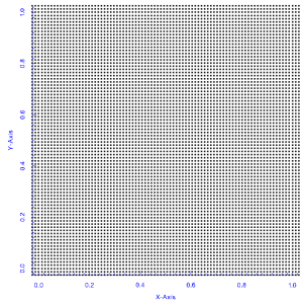

Figure 5.17: Initial particle distribution (for 130x130).

Three different initial fluid particle distributions are employed in this simulation for $Re = 100, 400$ and 1000, with initial distance $\Delta x = \Delta y$ between close neighbouring particles of 0.025, 0.0125 and 0.007692. In the current simulation, the physical properties are selected as $L = 1$, the top side of the square moves at a constant velocity of $u_{lid} = 1.0$, density is $\rho = 1000$ kgs^{-2} and kinematic viscosity is as described in Table 5.1.

Reynolds number	100	400	1000
Viscosity (m^{2}s^{-1})	0.01	0.0025	0.001

Table 5.1: Physical characteristics of the lid driven cavity.

Figure 5.17 shows the initial particle distribution. Three different resolutions of initial fluid particle distribution are used for various Reynolds numbers and time steps, as shown in Table 5.2:

	Grid size		
	40 × 40	80 × 80	130 × 130
Total Number of Particles	2116	7396	18225
Particle spacing (m)	0.025	0.0125	0.007692
Time step (R=100, 400, 1000)	6.0975E-04	3.0864E-04	1.9379E-04

Table 5.2: Comparison of the 2-D lid-driven cavity time step.

Numerical results

We performed numerical simulations for Re=100, 400 and 1000 using both dummy-boundary and ghost-boundary conditions (no-slip). The data of u-velocity profiles along at $x = 0.5$ and v-velocity at along $y = 0.5$ were extracted (which is plotted by dividing the line through centre to 10 equal spaces and measure velocities at each position by SPH sum) for three different particle number at Re=100, 400 and 1000 and found good agreement with the results of Ghia et al. (1982). For the dummy-boundary, the results are shown in Figures 5.18, 5.22 and 5.28. For ghost boundary the results are shown in Figures 5.19, 5.23 and 5.29. As expected, the smoother velocity and more accurate results are found by using a higher numbers of particles.

The cavity flow at Re=100

The maximum average density changes for the highest number of particles (130×130) were located at the top right corner of the cavity for a few particles. These density changes were (2.45%) and (2.72%) for dummy and ghost boundary, respectively. However, the average density difference over all particles was (%0.87) and (0.91%) for dummy and ghost density, respectively. Higher resolution results show close agreement with the results of Ghia et al. (1982).

The comparisons of vertical and horizontal velocity components are shown in Figures 5.18 and 5.19, including three different resolutions. Both boundary conditions in WCSPH give good results for both horizontal and vertical velocity, even with lowest particle number. The streamline contours for the cavity flow configuration with Re=100 are shown in Figures 5.20 (a) and 5.20 (b) for dummy- and ghost-boundary conditions, respectively. To plot streamline contours, we divide the domain into a grid; the stream function at each point in the grid has been calculated by SPH sum. These plots shows good comparison with Ghia et al. (1982) in primary vortices, but can not capture the secondary vortices at the bottom left and right. Comparison of the center of the primary vortices is given in Table 5.3. Vorticity contours are plotted in Figure 5.21 and generally compared with Ghia et al. (1982) results.

The cavity flow at Re=400

By employing the dummy boundary condition for Re=400 and highest number of particles (130×130), the highest variation of density is (1.15%) for some particles located at the right top corner of the cavity. On the other hand, by using ghost boundary, the maximum oscillation of density is (1.1%). However, the average fluctuations in the density of particles over the domain are (0.7%) and (0.65%) for dummy and ghost boundary, respectively. Using both boundary conditions in WCSPH gives a good estimation of both horizontal and vertical velocity components, even with the lowest resolution (dx=0.025 m), see Figures 5.22 and 5.23.

For dummy particles, a small hole at the centre of the cavity is found employing the normal definition of the speed of sound $c_0 = 10.u_{lid}$ (see Figures 5.24 (Left) and 5.24 (Right)). Lee et al. (2008*b*) and Shakibaeinia & Jin (2011) showed this problem at Re=400, 1000 and 3200. Lee et al. (2008*b*) recommended removing this void using a speed of sound one hundred times larger than the lid velocity. Particle shifting also eliminates voids, Mokos et al. (2017).

In this work, $c_0 = 100.u_{lid}$ and background pressure has been tested. A background pressure of $\chi = 0.01$ is used here, for more details see Equation 3.23. The void at the centre of cavity is not present when using the ghost boundary condition, see Figure 5.25. We see the streamline, vorticity contour and the location of the centres of the vortices agree

well with Ghia et al. (1982) (see Table 5.3, Figure 5.26 and 5.27). Again, the main vortices at the centre as shown agree well but the secondary vortices at the bottom right and left not captured, figures 5.26.

The cavity flow at Re=1000

Horizontal and vertical velocity component profiles are compared with Ghia et al. (1982) data, (see Figure 5.29). For a few particles located a the top right corner, the maximum average density changes by (1.5%) for dummy particles and by (1.35%) for the ghost boundary. Average density variation changed by (1.1%) and (0.9%) for dummy and ghost boundary.

The streamline and vorticity contours for the cavity flow configuration with Re=1000 are shown in Figures 5.30 and 5.31, respectively. The streamline contour gives very good results and the locations of centres of the vortices are compared with Ghia et al. (1982) results in Table 5.3. For higher Reynolds number vorticity changes more rapidly than at lower Reynolds as shown by the decreased spacing between vorticity contours.

The result shows that results from both boundary conditions are in good agreement with Ghia et al. (1982) but we prefer ghost boundary condition, since the void at the centre of cavity vanishes without using any extra conditions. Vorticity contours show a better match for ghost boundary compared to the dummy boundary conditions.

	Re=100		Re=400		Re=1000	
	x	y	x	y	x	y
Ghia et al. (1982)	0.6172	0.7344	0.5547	0.6055	0.5313	0.5625
For dummy boundary	0.602	0.762	0.589	0.619	0.532	0.582
For ghost boundary	0.601	0.743	0.586	0.621	0.543	0.593

Table 5.3: Comparison of the 2-D lid-driven cavity of centre of the vortices at Re=100, 400 and 1000.

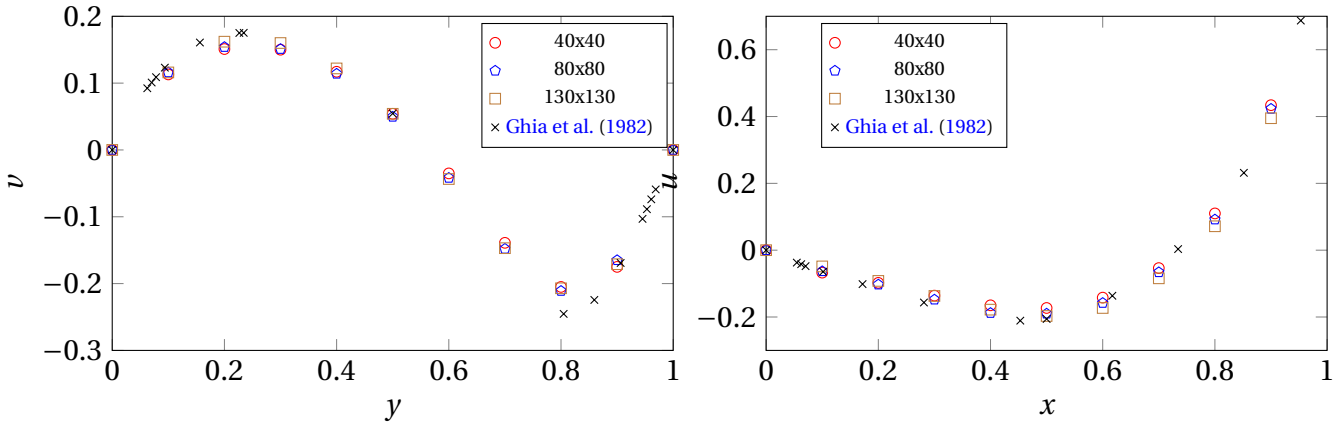

Figure 5.18: Velocity profiles for Re=100 using dummy boundary condition for particle resolution of 0.025, 0.0125 and 0.007692 and the results are compared to the data of Ghia et al. (1982): (Left) at: Mid-vertical cross-section of the cavity. (Right)at: Mid-horizontal cross-section of the cavity.

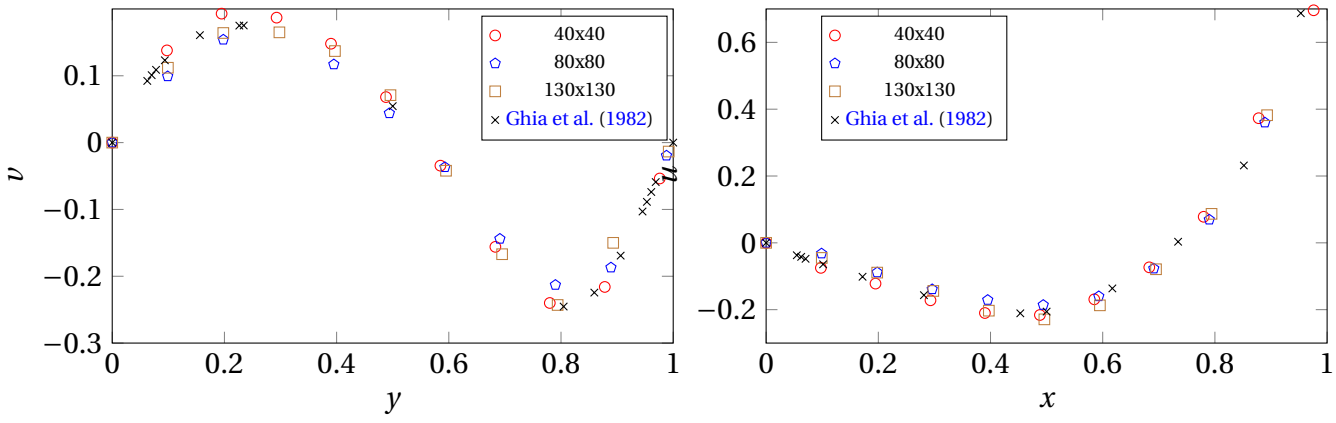

Figure 5.19: Velocity profiles using ghost boundary condition for Re=100 using ghost boundary condition for particle resolution of 0.025, 0.0125 and 0.007692 and the results are compared to the data of Ghia et al. (1982): (Left) at: Mid-vertical cross-section of the cavity. (Right) at: Mid-horizontal cross-section of the cavity..

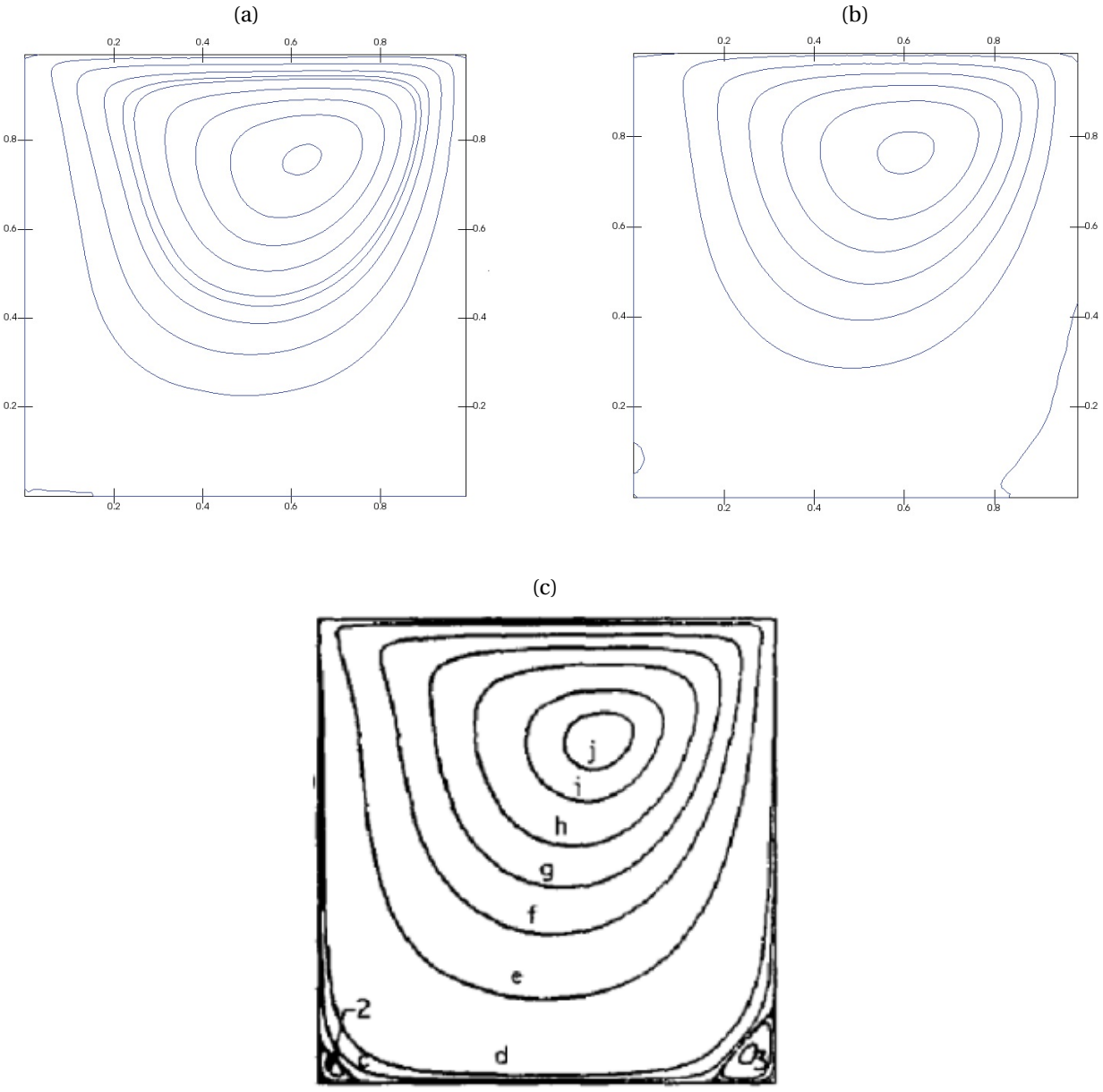

Figure 5.20: Comparison of streamline results for Re=100 with Ghia et al. (1982): (a) Using dummy boundary. (b) Using ghost boundary. (c) Ghia et al. (1982) results.

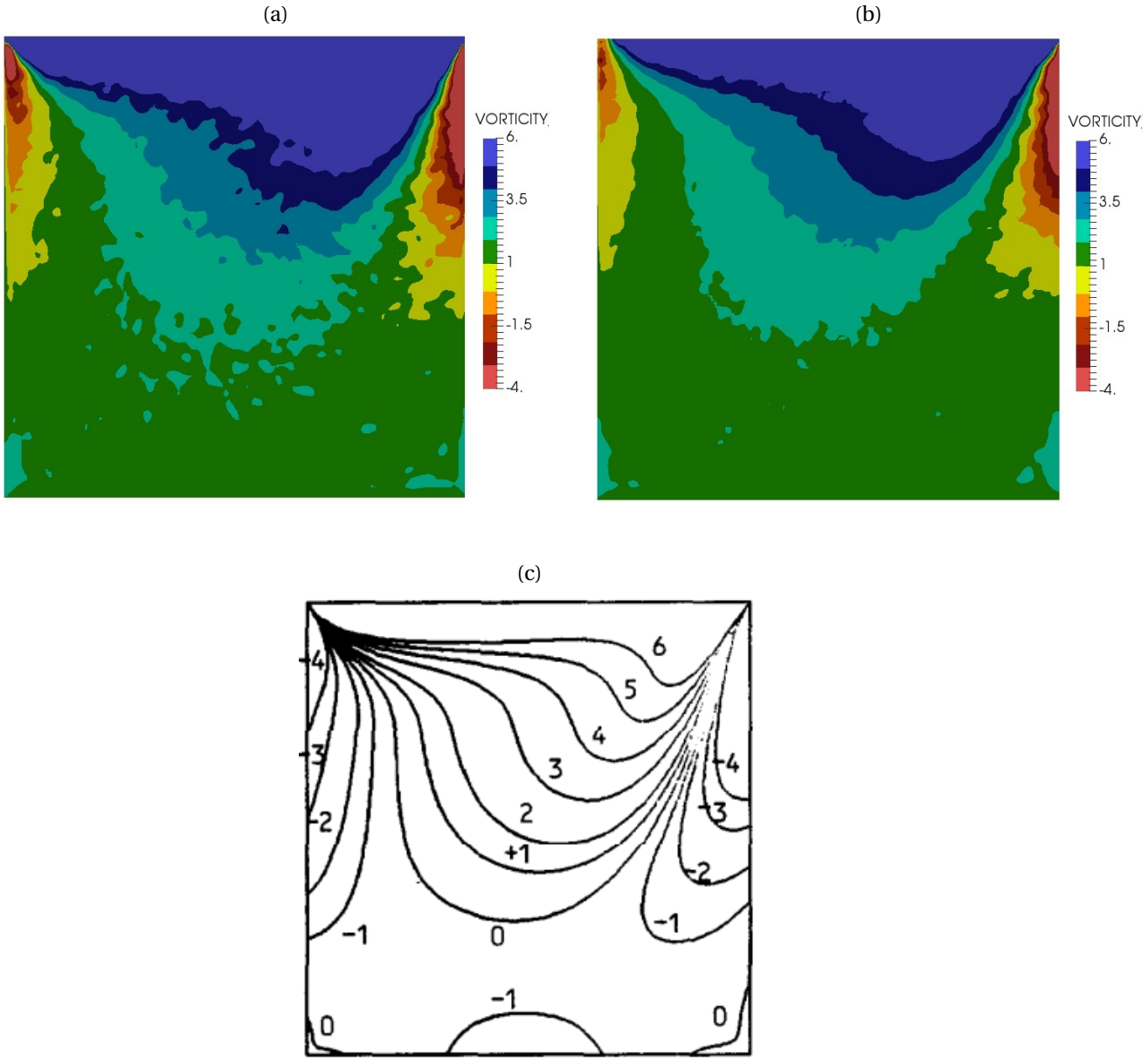

Figure 5.21: Comparison of vorticity contour results for Re=100 with Ghia et al. (1982): (a) Using dummy boundary. (b) Using ghost boundary. (c) Ghia et al. (1982) results.

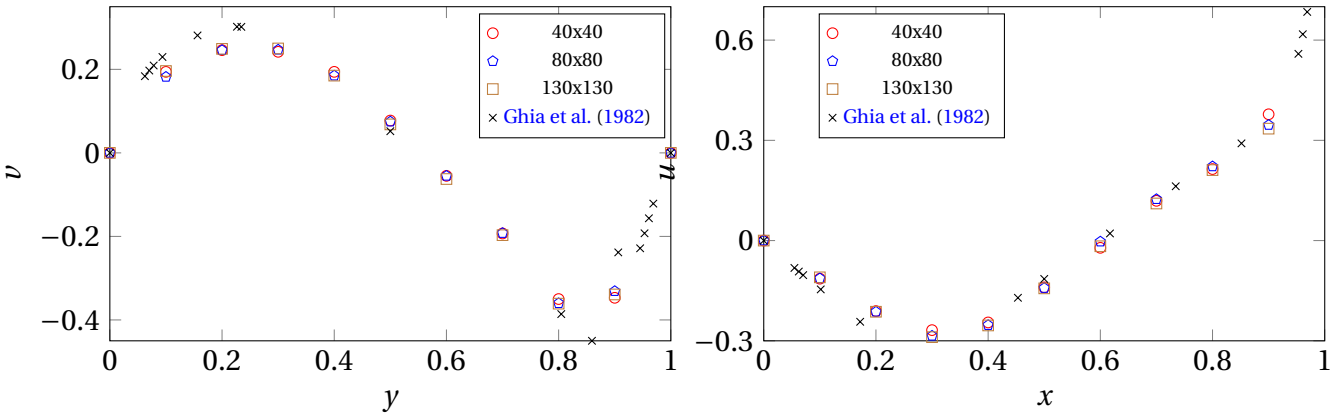

Figure 5.22: Comparison of velocity values using dummy boundary for Re=400 for particle resolution of 0.025, 0.0125 and 0.007692 with Ghia et al. (1982) (Left) at: Mid-vertical cross-section of the cavity. (Right) at: Mid-horizontal cross-section of the cavity.

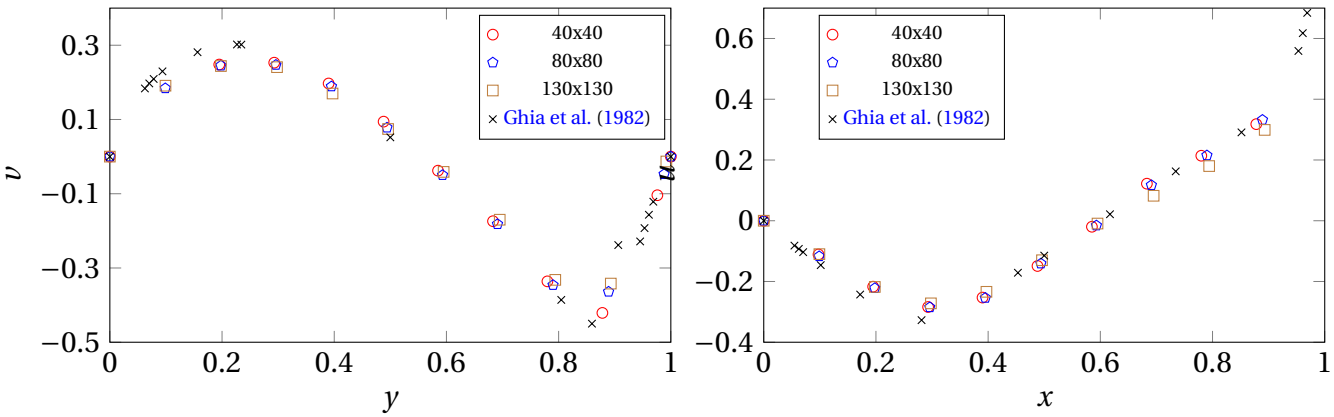

Figure 5.23: Comparison of velocity values using ghost boundary for Re=400 for particle resolution of 0.025, 0.0125 and 0.007692 with Ghia et al. (1982) (Left) at: Mid-vertical cross-section of the cavity. (Right) at: Mid-horizontal cross-section of the cavity.

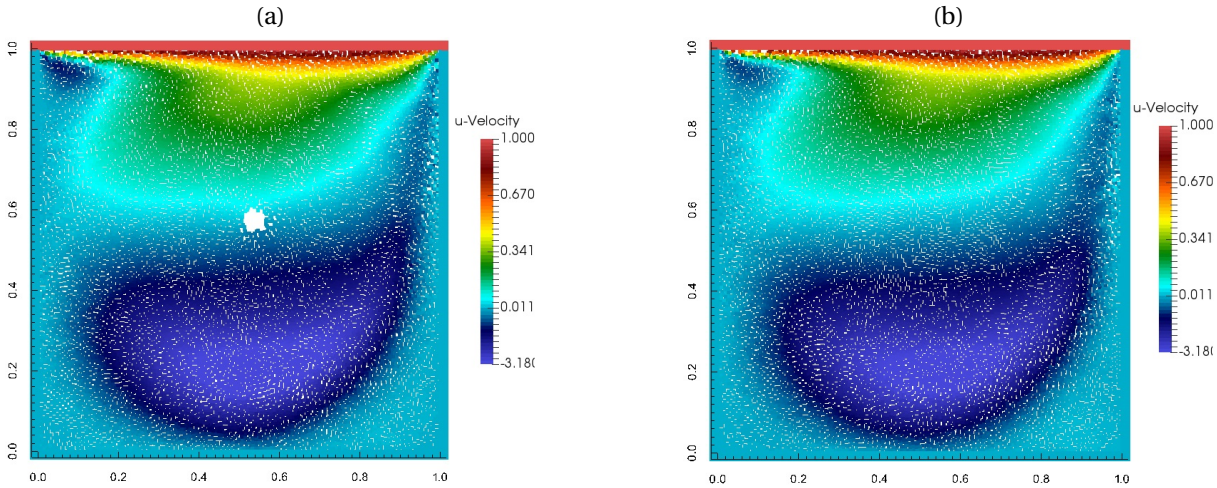

Figure 5.24: Velocity profiles using dummy boundary conditions: (Left) at: Mid-vertical cross-section of the cavity with $c = 10u_{lid}$ and no background pressure. (Right) With background pressure

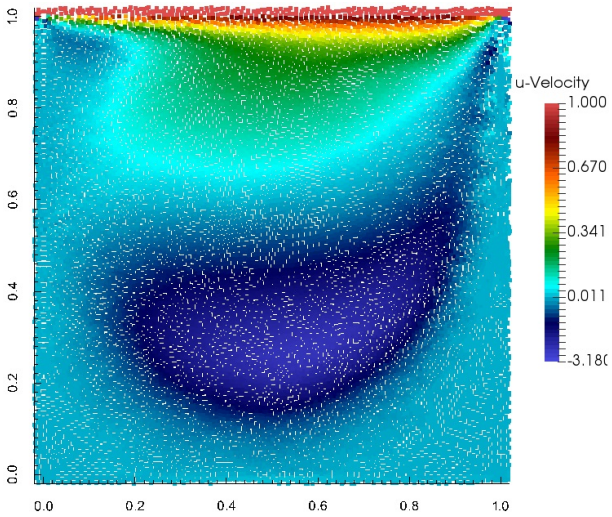

Figure 5.25: Velocity distributions using ghost boundary conditions at: Mid-vertical cross-section of the cavity with no background pressure.

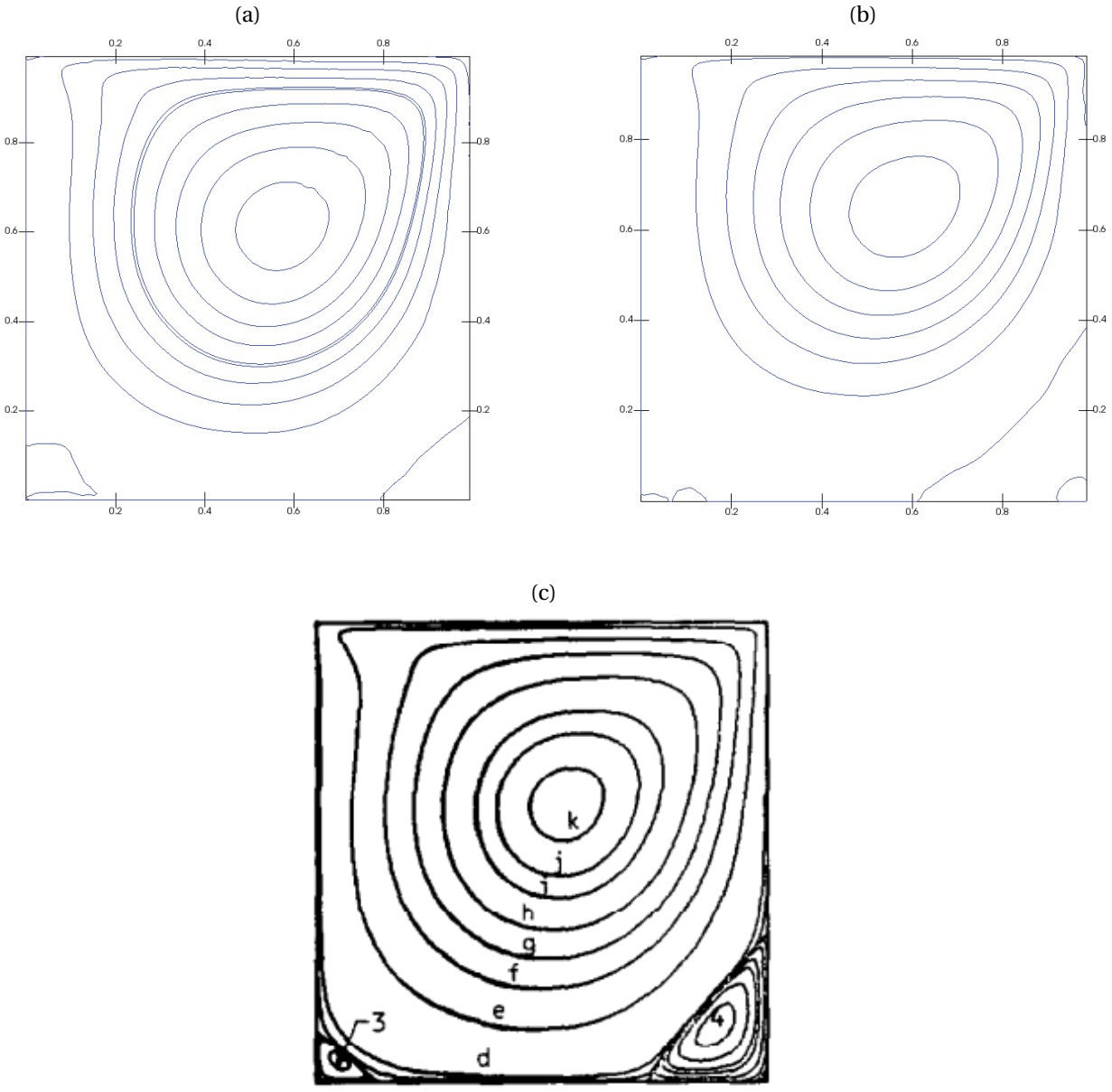

Figure 5.26: Comparison of streamline results for Re=400 with Ghia et al. (1982): (a) Using dummy boundary. (b) Using ghost boundary. (c) Ghia et al. (1982) results.

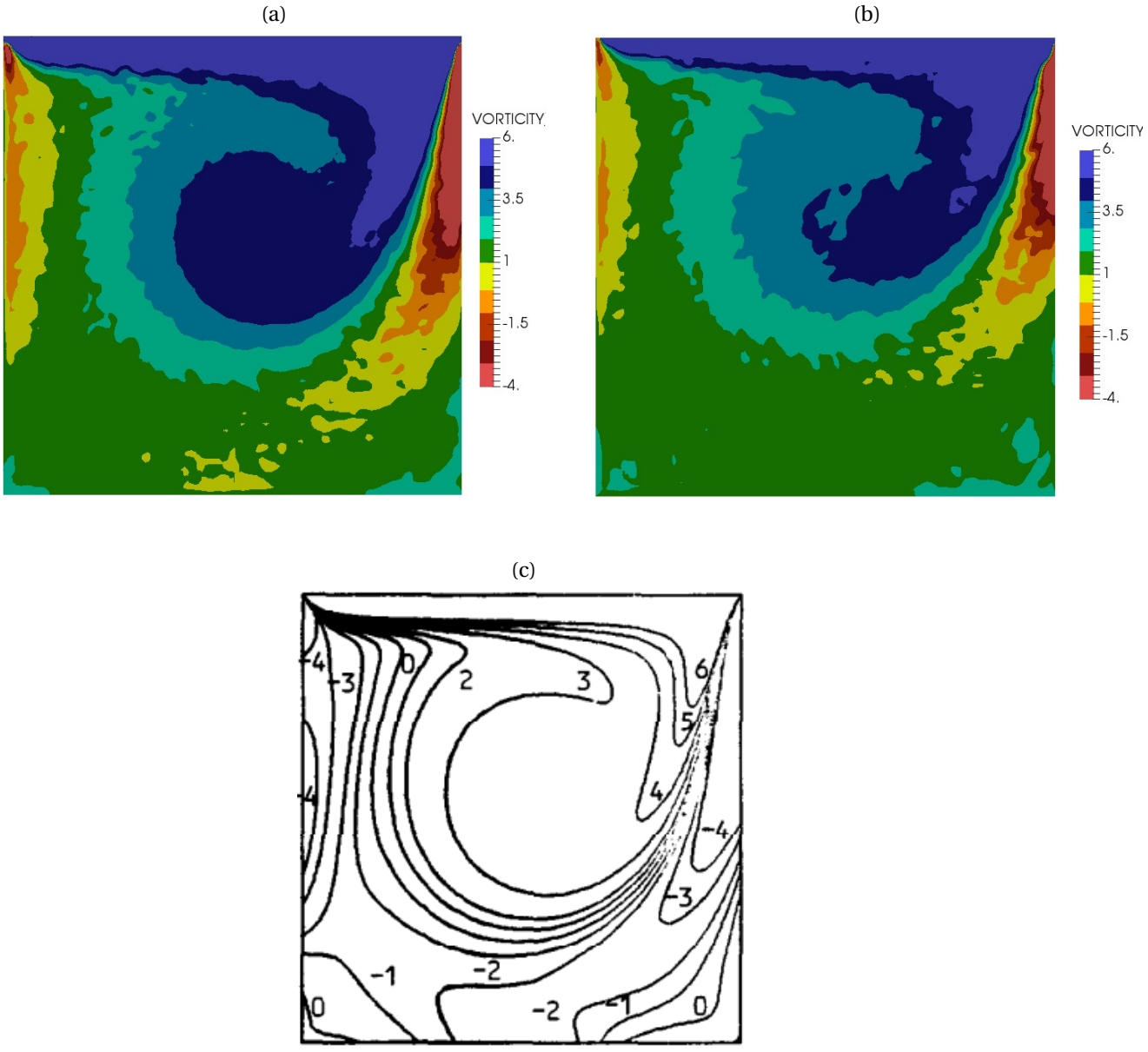

Figure 5.27: Comparison of vorticity values for Re=400 with Ghia et al. (1982): (a) Using dummy boundary. (b) Using ghost boundary. (c) Ghia et al. (1982) results.

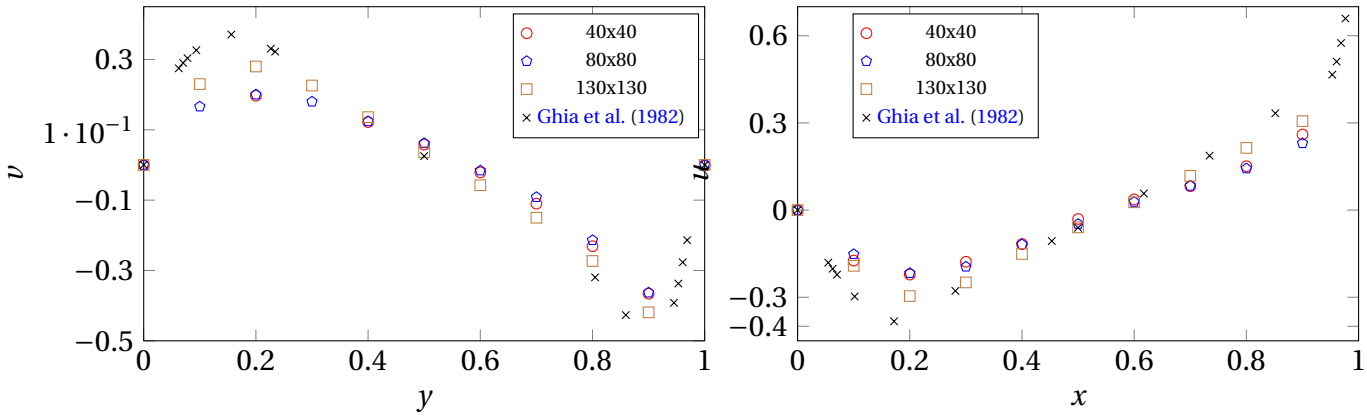

Figure 5.28: Comparison of velocity values using dummy boundary for Re=1000 for particle resolution of 0.025, 0.0125 and 0.007692 with Ghia et al. (1982) (Left) at: Mid-vertical cross-section of the cavity. (Right) at: Mid-horizontal cross-section of the cavity.

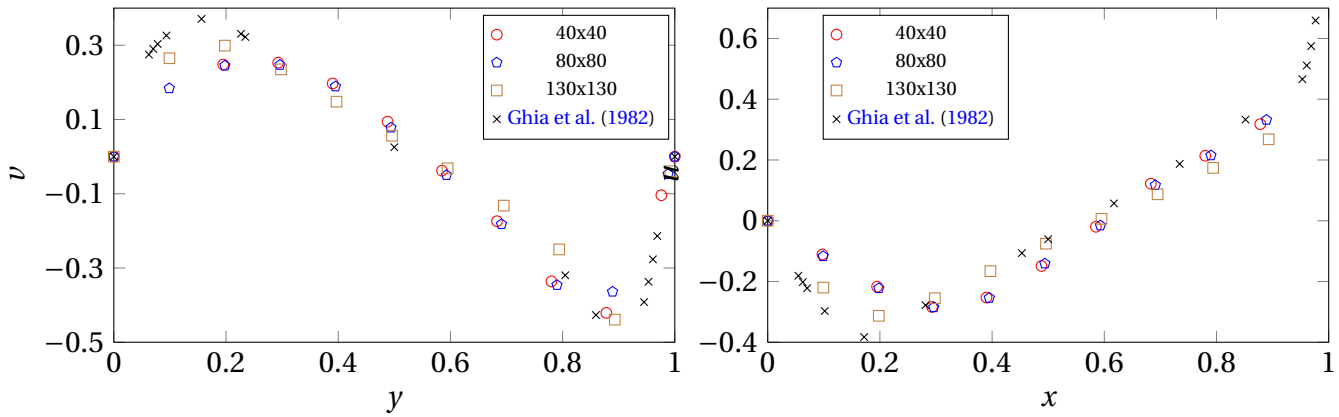

Figure 5.29: Comparison of velocity values using ghost boundary for Re=1000 for particle resolution of 0.025, 0.0125 and 0.007692 with Ghia et al. (1982) (Left) at: Mid-vertical cross-section of the cavity. (Right) at: Mid-horizontal cross-section of the cavity.

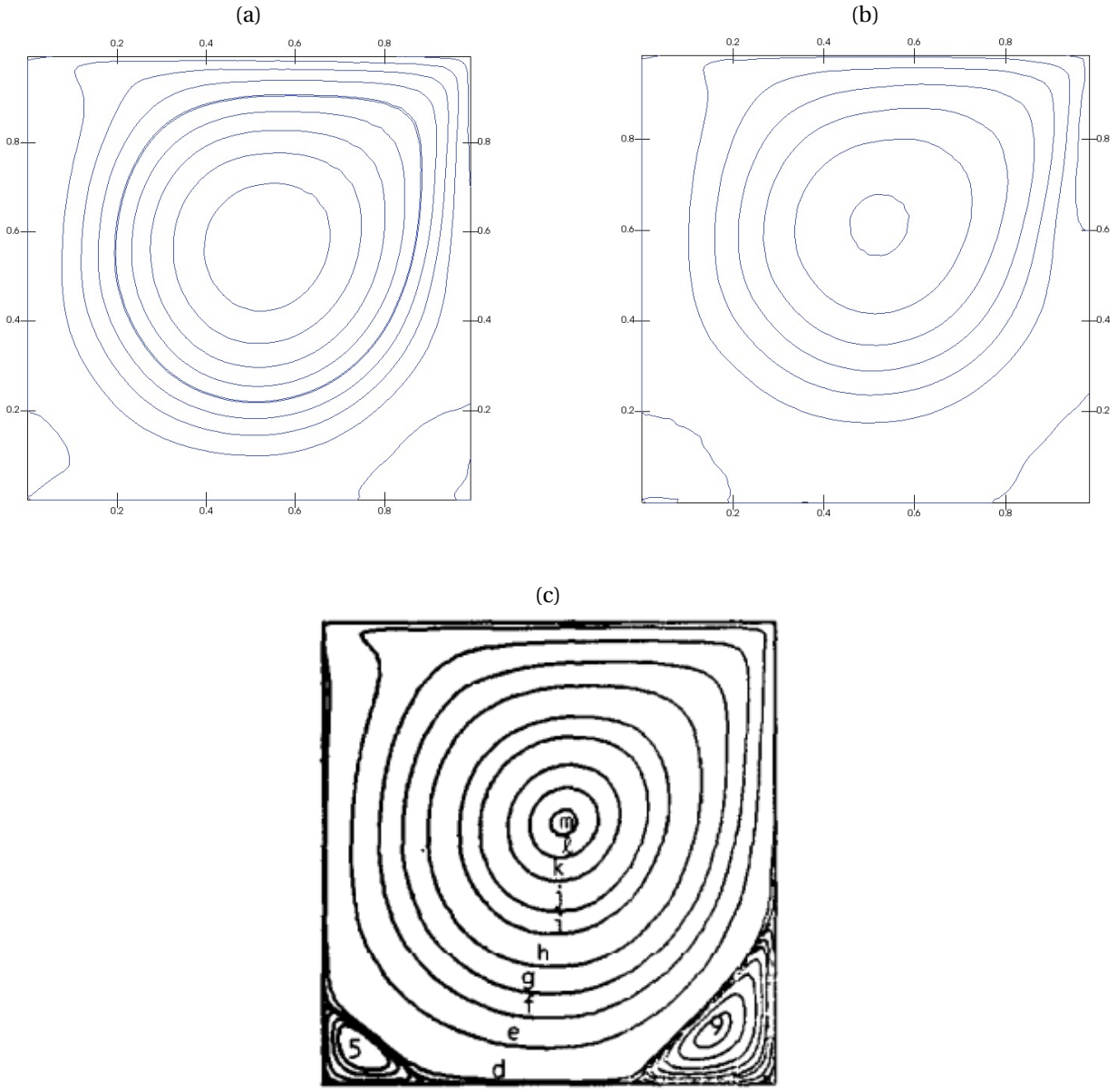

Figure 5.30: Comparison of streamline results for Re=1000 with Ghia et al. (1982): (a) Using dummy boundary. (b) Using ghost boundary. (c) Ghia et al. (1982) results.

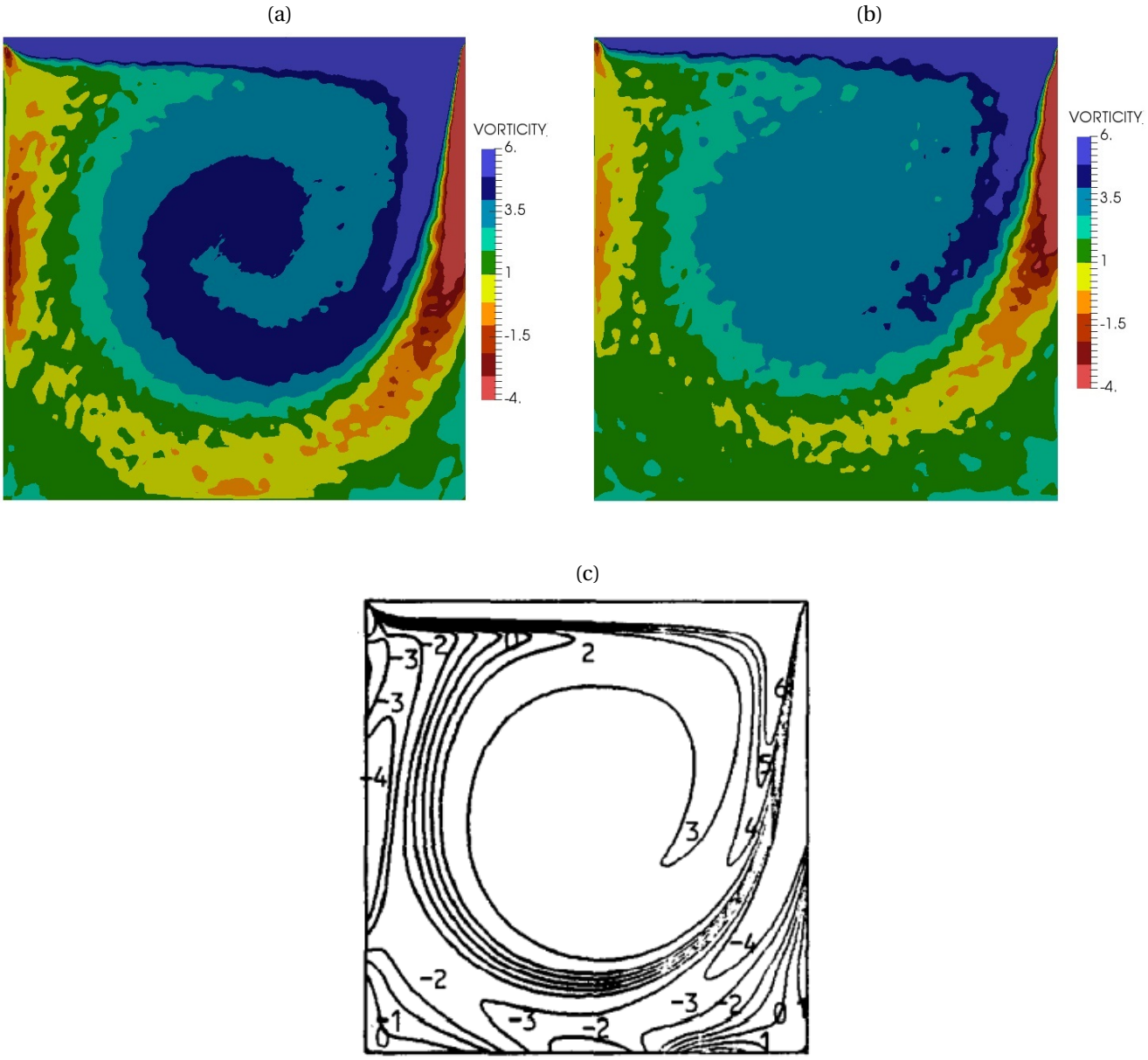

Figure 5.31: Comparison of vorticity values for Re=1000 with Ghia et al. (1982): (a) Using dummy boundary. (b) Using ghost boundary. (c) Ghia et al. (1982) results.

5.2 Conclusions related to single phase model

In this chapter, we described some implementations of the SPH method for simulations of lid-driven cavity flow and two different dam-break cases. Two different boundary conditions have been investigated and the validation results for different cases are presented and compared with numerical and experimental results. We prefer to use the ghost boundary condition (no-slip) for this study. The Shepard filter is applied to reduce density oscillations every 15 time steps. The Wendland kernel has been used as it is free from clumping for large numbers of particles, Dehnen & Aly (2012).

First: two different dam-break cases have been investigated for two different boundary conditions. The results have been compared with other numerical and experimental results. In the first case, both resolutions are closer and agree well to the numerical solution of Colagrossi & Landrini (2003) results. For the second model, comparison has been made and the results are in good agreement with experimental data of Martin & Moyce (1952).

Second: The SPH method has been successfully applied to simulate lid-driven cavity flow. The void inside the cavity disappear with the ghost boundary condition compared to the dummy boundary that needs extra conditions. In the first case, three different Reynolds numbers were used. Numerical results are in generally good agreement with Ghia et al. (1982) data.

5.3 Two Dimensional Cases: MultiPhase

Multi-phase flow is commonplace in marine and coastal engineering applications. To fully capture the physical nature, the air phase needs to be included. The air phase could have a large influence on the free surface and interaction with structures. Therefore, the single phase simulation is extended to the multi-phase flow. One of the issues in multi-phase flow is a discontinuity in density at the interface between fluids. To fix this problem, extra calculations are needed to take this into account. Small changes in density can became a large fluctuation in the pressure field. In this study to control any change in density, the density re-normalisation method (Shepard filter, Panizzo & Dalrymple (2004)) has been employed every 15 time steps for each phase separately. Figure 5.32 shows the density re-normalisation for each phase where just the same type of particles are taken into account. Finding pressure directly from density for each phase from equations, 5.2 and 5.3 for water and air, respectively, is Nugent & Posch (2000)

$$p_w(\rho) = \frac{c_w^2 \rho_w}{\gamma_w}[(\frac{\rho}{\rho_w})^\gamma - 1 + \chi_w], \tag{5.2}$$

$$p_a(\rho) = \frac{c_a^2 \rho_a}{\gamma_a}[(\frac{\rho}{\rho_a})^\gamma - 1 + \chi_a]. \tag{5.3}$$

To get the same initial pressure at the interface between water and air, we set, Colagrossi & Landrini (2003):

$$\frac{c_w^2 \rho_w}{\gamma_w} = \frac{c_a^2 \rho_a}{\gamma_a} \tag{5.4}$$

$$\chi_w = \chi_a$$

Where χ_w and χ_a are background pressure coefficient for water and air phase, respectively.

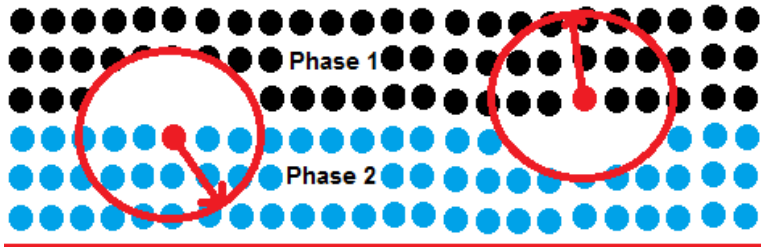

Figure 5.32: The implementation of density re-normalisation.

Influence of re-normalization density for each phase separately

The influence of the re-normalisation density will be shown with the interface between phases in Figure 5.33. The normalization density is given by:

$$\rho_i^{new} = \sum_j m_j \widetilde{W_{ij}}, \tag{5.5}$$

where

$$\widetilde{W_{ij}} = \frac{W_{ij}}{\sum_j W_{ij} \frac{m_j}{\rho_j}}.$$

When the fluid particles for re-normalization density are not separated, the neighbouring particles j include both water and air particles.

At the interface between phases, the heavy phase will have high pressure and push the light phase particles back at the interface, see Figure 5.33 (Left). This is clearly unphysical. This can be prevented by testing the re-normalization density for each phase separately, See Equation 5.6 and Equation 5.7 for the water and air phase, respectively. The improvement is shown in Figure 5.33.

$$\rho_{i_{water}}^{new} = \sum_{j_{water}} m_{j_{water}} \widetilde{W}_{ij_{water}}, \tag{5.6}$$

$$\rho_{i_{air}}^{new} = \sum_{j_{air}} m_{j_{air}} \widetilde{W}_{ij_{air}}, \tag{5.7}$$

where

$$\widetilde{W_{ij}}_{water} = \frac{W_{ij_{water}}}{\sum_{j_{water}} W_{ij_{water}} \frac{m_{j_{water}}}{\rho_{j_{water}}}}.$$

and

$$\widetilde{W_{ij}}_{air} = \frac{W_{ij_{air}}}{\sum_{j_{air}} W_{ij_{air}} \frac{m_{j_{air}}}{\rho_{j_{air}}}}.$$

5.4 Validation of Results

In this section, the multiphase flows involving water and air will be investigated. The implementation of standard zero-pressure-gradient conditions can lead to non-physical low-frequency pressure oscillations in both single-phase free surface and multi-phase WCSPH flow computations. Additionally, it is well known that negative pressure can lead to the

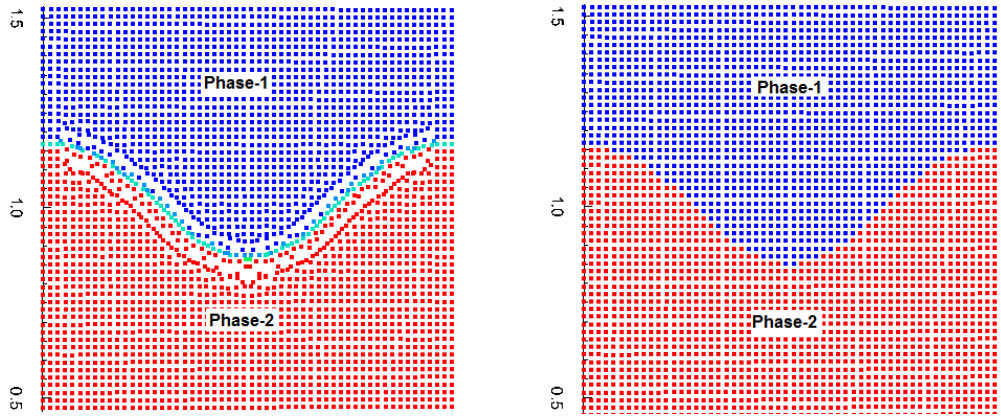

Figure 5.33: Rayleigh-Taylor instabilities. Particle position at $t = 0.024$ selected, using re-normalisation density: Left: For each phase is not separated. Right: For each phase is separated.

formation of voids in WCSPH, Barcarolo et al. (2012), or the lighter phase, Mokos et al. (2017), and cause other problems with numerical solutions. In this study treatments required on the interface between phases are the re-normalization density for each phase separately and adding background pressure. We also investigated an alternative approach, whereby a cut-off value for the density is specified to avoid negative pressure, Chen et al. (2015). The WCSPH formulation were shown in Chapter 3 will be used.

The following cases are implemented to test our multiphase SPH code.

5.4.1 Case One: Rayleigh-Taylor

We consider the Rayleigh-Taylor problem in this study to test our multiphase flow model. In this case, lighter phase with density $\rho_1 = 1\,\mathrm{kg\,s^{-2}}$ sits below a heavier phase with density $\rho_1 = 1.8\,\mathrm{kg\,s^{-2}}$. The computational domain is rectangular, with $0 < x < 1$ and $0 < y < 2$. Initially the two phases

are separated with an interface at to $y = 1.0 - 0.15\sin(2\pi x)$. The Reynolds number and time step are set to Re= $\frac{\rho g^{1/2} H^{3/2}}{\mu} = 420$ (where H is the half of height of the domain) and $\Delta t = 0.1663 \times 10^{-3}$, respectively. The initial particle velocity is set to zero and the initial setup of the Rayleigh-Taylor instability is shown in Figure 5.34.

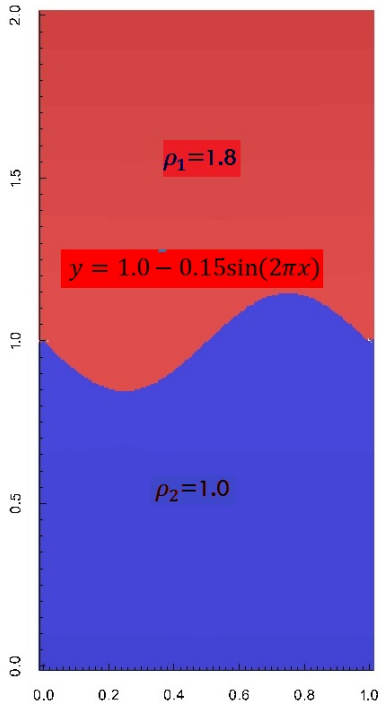

Figure 5.34: Initial conditions of the Rayleigh-Taylor instability.

Numerically, a total of 60x120 fluid particles are employed in this simulation. The parameters used in our simulation are represented in Tables 5.4.

The particle position at times $t = 3$ and 5 are shown in figure 5.35, 5.36, 5.37 and 5.38. Our simulation results generally compared reasonably well with reference solution given by a Cummins & Rudman (1999) and Hu & Adams (2009*a*) at two different times. However, the present result shows

H	1
Re	420
ρ^{ratio}	1/1.8
Kernel	Wendland
radius	$1.3\Delta x$

	Light Phase	Heavy Phase
ρ	1	1.8
γ	7	7
Speed of sound	28	28
Dynamic viscosity	0.006734	0.012122

Table 5.4: Summary of the parameters used in our simulations.

the plumes start roll-up along the sides with sharp spikes slightly later than the Cummins & Rudman (1999) at time $t = 3$. The interface positions of particles at time $t = 5$ are shown in Figure 5.36; the mushroom is beginning to roll-up in the present simulation, but not in Cummins & Rudman (1999). The lower spike nearly reaches the bottom wall in Cummins & Rudman (1999), but in our results, still has some distance to travel. In this study, the plumes developed with a sharp spike in both sides, in contrast to Cummins & Rudman (1999) which developed without any sharp spike plumes. On the other hand, the rolling up of the plumes is slightly late and the mushrooms are less spiked in both sides, compared to Hu & Adams (2009*a*), but the interface between the two phases in our simulation is smoother than that of these authors.

The pressure field at the beginning of the simulation is unsteady, but after a few time steps, the pressure kept approximately hydrostatic during the simulation.

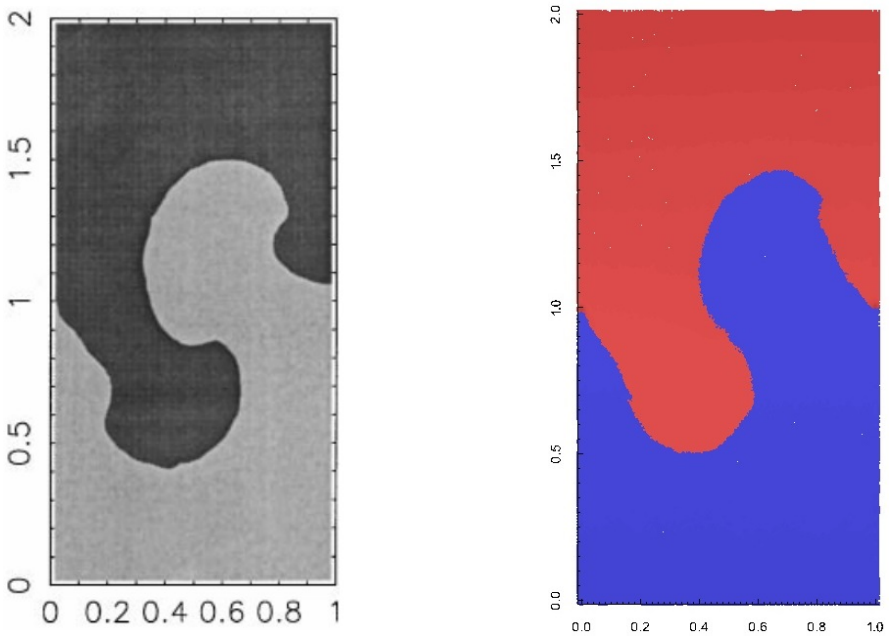

Figure 5.35: Rayleigh-Taylor instabilities. Particle position at $t = 3$ selected, using (a) Cummins & Rudman (1999) numerical results (b) our implementation .

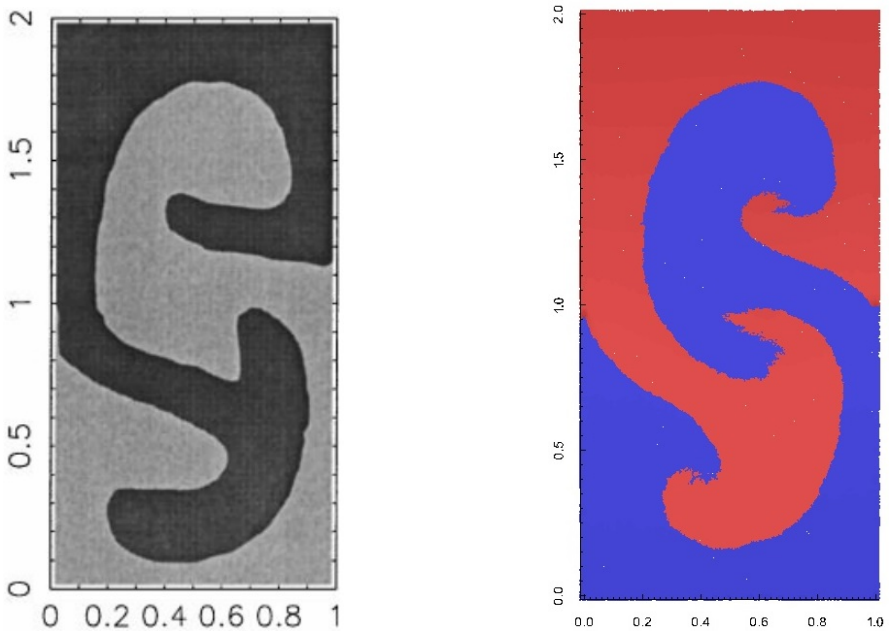

Figure 5.36: Interface position at $t = 5$ for the Rayleigh-Taylor instabilities. Using (a) Cummins & Rudman (1999) numerical results (b) our implementation

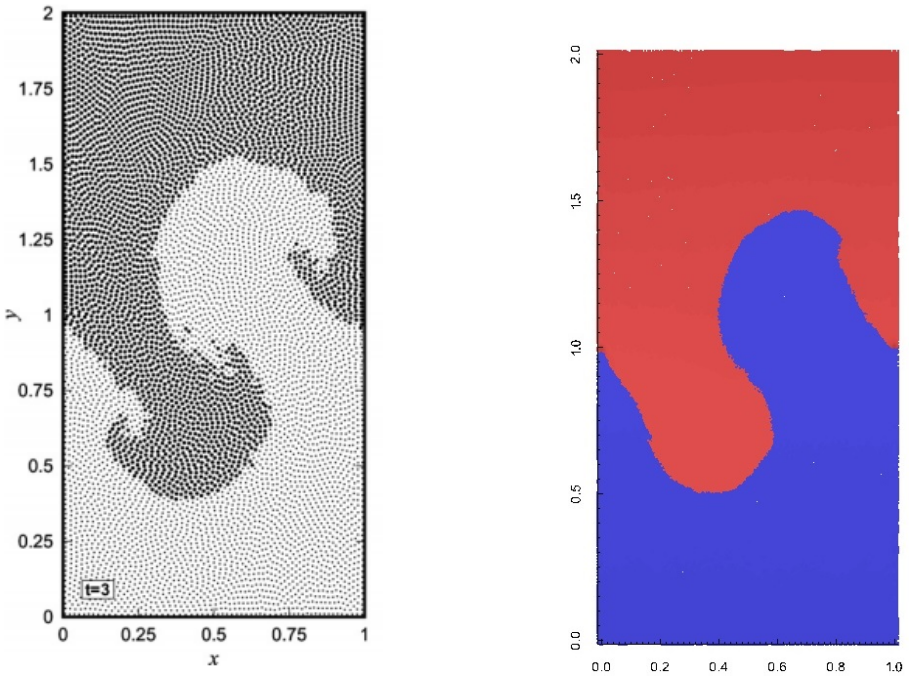

Figure 5.37: Rayleigh-Taylor instabilities. Particle position at $t = 3$ selected. Using (a) Hu & Adams 2009*a* numerical results (b) our implementation

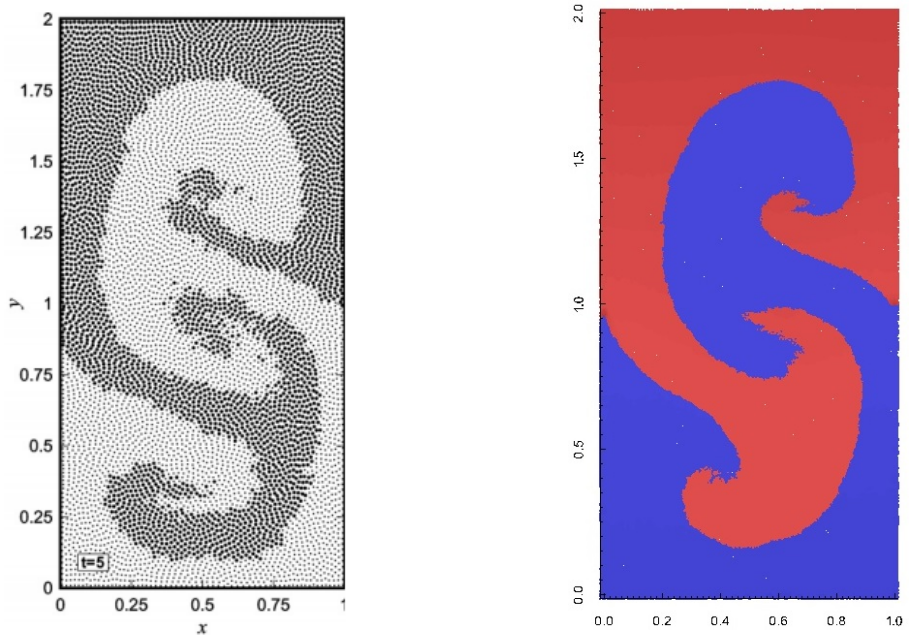

Figure 5.38: Interface position at $t = 5$ for the Rayleigh-Taylor instabilities. Using (a) Hu & Adams 2009*a* numerical results (b) our implementation

5.4.2 Case Three: Rising Bubble in Water

In this section, air bubble rising through the water will be simulated for a small density ratio ($\frac{\rho_a}{\rho_w} = 0.001$). The configuration of the rising bubble is shown in Figure 5.39. The air bubble is rising through a stationary water column with width and height of $6R$ and $10R$, respectively, where R is the bubble radius. Here, the no-slip boundary conditions are applied at the top and bottom walls.

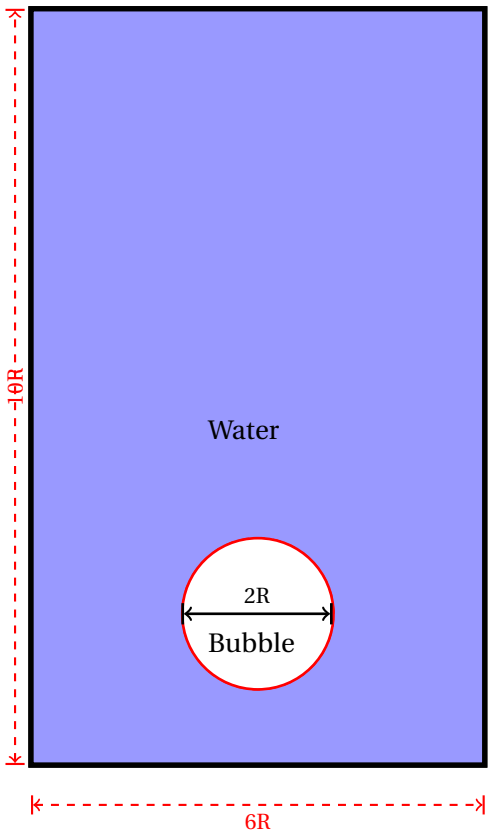

Figure 5.39: Configuration of a bubble rising in water

In this case, an extra term will be added to the pressure gradient equation. This term prevents the dispersion of the bubble particles in the

water phase, Colagrossi & Landrini (2003) and the extra term is:

$$-2\bar{a}\rho_a^2\frac{m_j}{\rho_w}\nabla_i W_{ij} \tag{5.8}$$

where $\bar{a}$ is the interface control coefficient and will be assumed as in Colagrossi & Landrini (2003):

$$\bar{a} = 1.5\rho_w g r/\rho_a^2.$$

This equation is used only in the pressure gradient term between the same particles of the air phase. For this case the density ratio and and kinematic viscosity are

$$\frac{\rho_a}{\rho_w} = 0.001$$

and

$$\frac{\nu_a}{\nu_w} = 128.$$

The speed of sound for water and bubble are set $28.28\sqrt{gR}$ and $400\sqrt{gR}$, respectively. Using the physical value of speed of sound will result in very small time steps, which is unsuitable for simulation. Based on the Equation 5.4, Colagrossi & Landrini (2003), and substituting the physical speed of sound for air and water, we can see that the pressure at the interface will not be the same; creating pressure difference between air and water at the interface . In order to solve this problem, an unphysical value for the speed of sound will be used. As we mentioned, the pressure at the interface needs to be the same for air and water. Then the air phase

will be simulated by a larger speed of sound, in contrast to its physical value and vice versa for the water phase, Mokos et al. (2017). The total number of particles used in this simulation is 216000. Fixed time step size of $\Delta t = 0.8936 \times 10^{-5}$ is used. The results are shown in Figure 5.40 and are compared with the shape of the bubble from a level set method (Sussman et al. (1994)). The thickness along the middle of the bubble is bigger than that from the level set method. Later on, the jets of small bubbles at the edge of the large bubble during the simulation are smaller compared to the level set method. After the jets are separated from the bubble in our simulation, five bubbles will appear as two large and three small bubbles. In the level set method, six bubbles were predicted: three each side. Both large bubbles in each side are in good agreement with our simulation, but one of the small bubbles does not appear in our SPH method. Finally, in the level set (Sussman et al. (1994)) simulation, those small bubbles vanished due to numerical errors in mass conservation, Colagrossi & Landrini (2003). In contrast, in our simulation the small bubbles will remain.

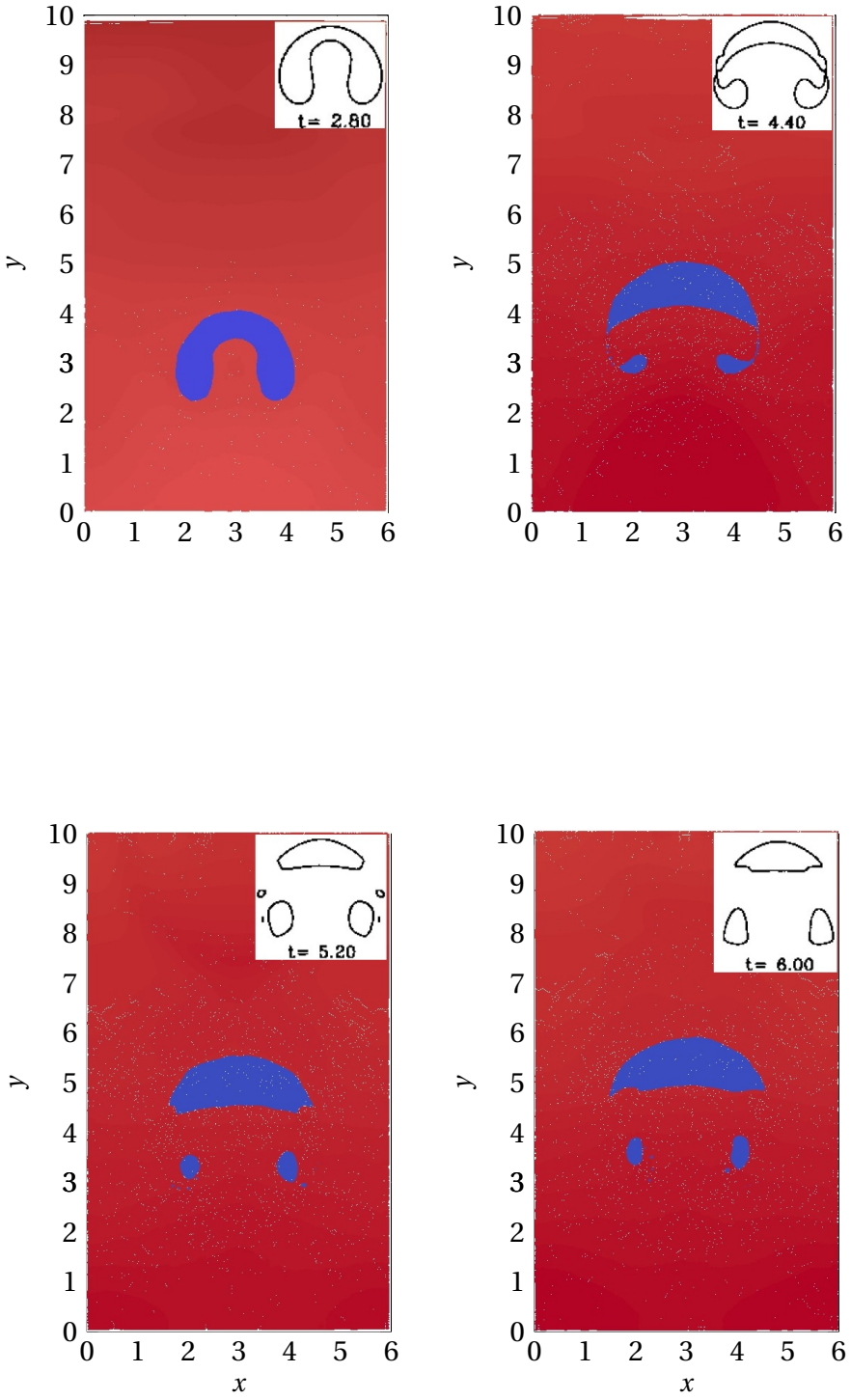

Figure 5.40: Time evaluation of rising bubble problem, using SPH method and compared the shape of bubble with level set (Sussman et al. (1994)) method.

5.4.3 Case Four: Dam break

In this section, the dam-break cases which were simulated in section 5.1.2 are simulated using a two-phase flow model. Colagrossi & Landrini (2003) introduced extra terms for multiphase flows to avoid dispersing air particles on the water phase, as we mentioned in section 5.4.2. Fourtakas (2014) and Mokos et al. (2017) used the shifting algorithm to remove the voids and interface issues. Mokos et al. (2017) employed a shifting algorithm, as well, to solve the interface problem between phases in multiphase flow in which the air particles were unphysicaly dispersing into the air phase. He investigated a large number of configurations and different parameters of Colagrossi & Landrini (2003) to eliminate the void but he found this did not have an effect on air particles and the void remains Mokos et al. (2017) tried, by modifying the speed of sound for air particles, to solve the voids issue and found that they disappeared for a short time and then re-appeared.

In this study, the background pressure has been investigated for both phases separately. An investigation has shown the background pressure has the main role of removing the voids. The best value for background pressure we have tested is between 0.05 to 0.1. We have tested two different dam-break cases with three different resolutions and the position of the height and toe edge of the water column is tracked and compared with numerical results and experimental data, Martin & Moyce (1952),

Buchner (2002), Colagrossi & Landrini (2003) and Mokos et al. (2017).

Case one with $W = 2H, D = 5.366H$

The sketch shown in Figure 5.8 is a tank with a length of D=1.6 and height of H_{wall}=2m containing a water column with width W=0.6m and height H=0.3m. The water column is located in the left side of the tank and held by a gate which will be removed with fixed velocity when the water starts collapsing under gravity. The dam break is simulated as multi-phase flow for density ratio of 0.001. 368640 particles were employed in this simulation. The speed of sound of water and air used were $10.9\sqrt{gH} = 18.879$ and $155\sqrt{gH} = 268.46$, respectively. The initial particle spacing and time step are set as 0.00208 and 0.255×10^{-5}, respectively. The density re-normalisation was used every 15 times steps.

- Pressure distribution of water phase in free and multi-phase simulation

Figure 5.41 shows the pressure field distribution of the water phase in a multi-phase simulation at $t\sqrt{g/H} = 1.7$. After releasing the dam break

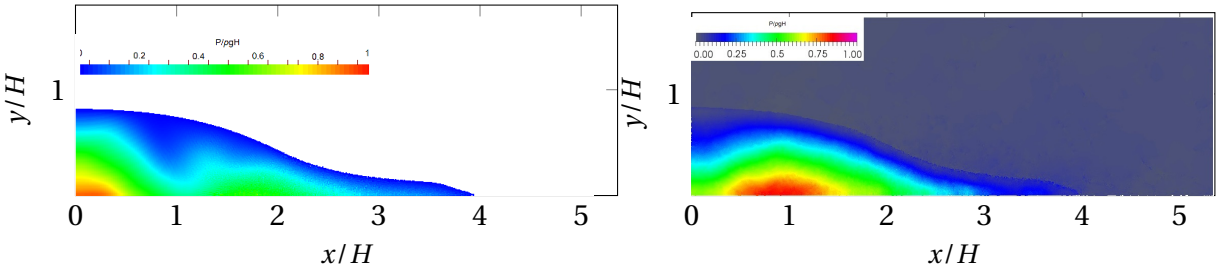

Figure 5.41: pressure distribution of water phase in multi-phase simulation at $t\sqrt{g/H} = 1.7$.

from hydrodynamics pressure, the water phase will experience oscillations in pressure for a few time steps and then will keep the hydrostatic pressure during the simulation. As shown in Figure 5.41, it is clear that the pressure contours are smoother in our multi-phase simulation than from the single-phase simulation.

- Overturn water after impact

Comparing Figure 5.41 with Figure 5.42, we see there are no significant differences between the motion of water when the air phase is involved, compared with the single phase case. Here, we focus on the pressure measurement on the vertical wall during the impact and after impact due to air particles being entrained by the overturned water after impacting the vertical wall at the right. Pressure measurement is set on the vertical wall 0.057m above the right-hand side corner. For this multi-phase model, the entrained voids will not vanish. Second, as we mentioned above, Mokos et al. (2017) demonstrated at high particle resolution, voids appear in the light phase. Here, we investigate the role of background pressure to remove the voids. Figure 5.42 shows the pressure fields model just after water overturns for the single-phase (left) and multi-phase (right). The Figures 5.42 and 5.43 show that our results are in a good agreement with the numerical results of Colagrossi & Landrini (2003).

Figure 5.42 shows that the pressure is increased inside the cavity and also will get large pressure in water phase near the right corner. In the single-

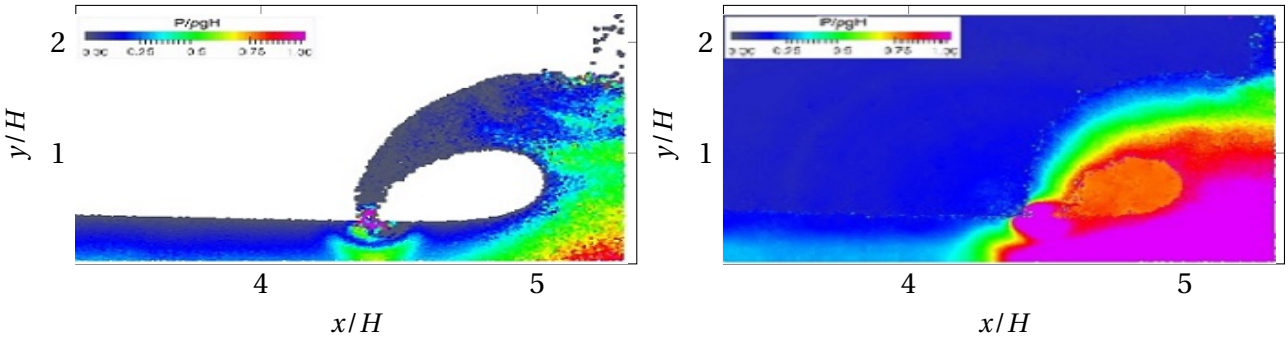

Figure 5.42: Overturn wave after impact against the vertical wall. Left: single-phase model. Right: Multi-phase flow model.

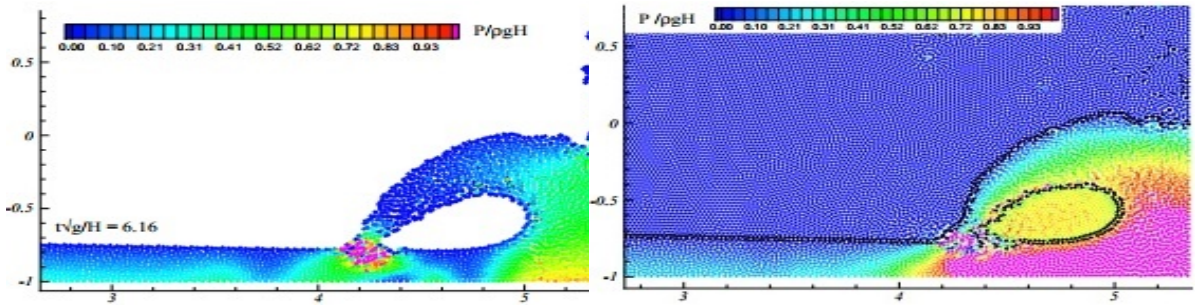

Figure 5.43: Single-phase (left) and air-water (right) of pressure field after impact the wall, from Colagrossi & Landrini (2003)

phase, the pressure inside the cavity will be lower than the multi-phase due to lack of the air phase, shown in Figure 5.42. The pressure at point $x = 5.336H, y = 0192H$ has been measured by using the SPH kernel sum and is plotted in Figure 5.44. Figure 5.44 shows the effect of entrapped air on pressure fields and shows that the multi-phase model is closer to the experimental data with high oscillation, compared to single-phase, around the second peak.

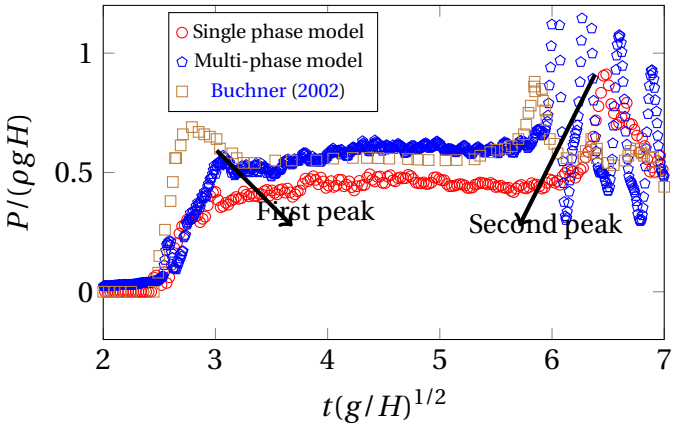

Figure 5.44: Comparison of temporal pressure profile at $y = 0.19H$ between experimental data, Buchner (2002).

- Toe position of dam break

Figure 5.45 shows that both single-phase and multi-phase models compare well with the results of Colagrossi & Landrini (2003).

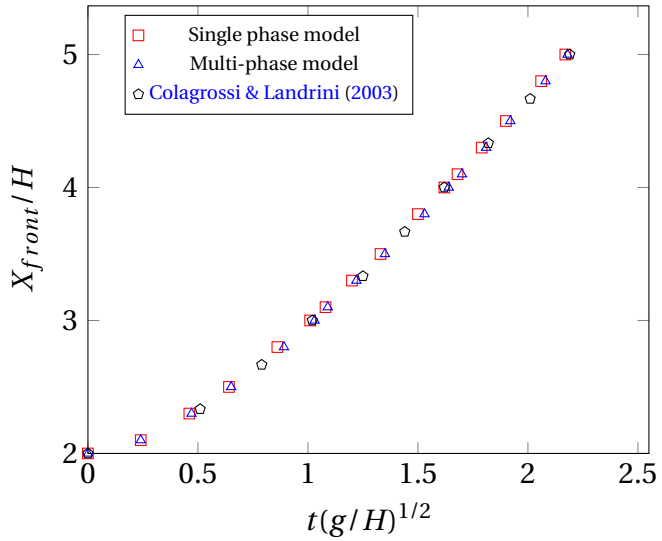

Figure 5.45: Time evaluation of the front of a collapsing water column for two different boundary conditions compared to Colagrossi & Landrini (2003).

Case two with $H = 2W, D = 2H$

The second case which was simulated in section 5.1.2 will now be modelled as a multi-phase flow (see Figure 5.46) and the result compared to our single-phase and Mokos et al. (2017) results. The ratio of air-water density is 0.001. Distributing particles uniformly with spacing of 0.001, the number of particles used in this case is 240000. In this study, no-slip boundary conditions for velocity are used.

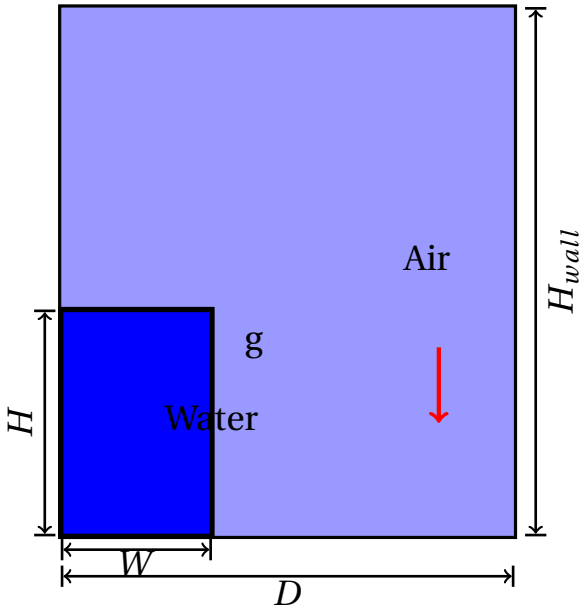

Figure 5.46: Configuration of dam break for multi-phase case

The time step and speed of sound for both water and air are 0.1625×10^{-5}, $10.\sqrt{2gW} = 14.42$ and $282.84\sqrt{gW} = 200$, respectively.

The results for the jet tip and water column height obtained from the multi-phase case are plotted in Figure 5.47 and 5.48. The results are slightly closer to the experiment values compared to the single phase. The water phase moves slightly slower in the multi-phase flow than the single-phase due to the repulsive forces from air particles.

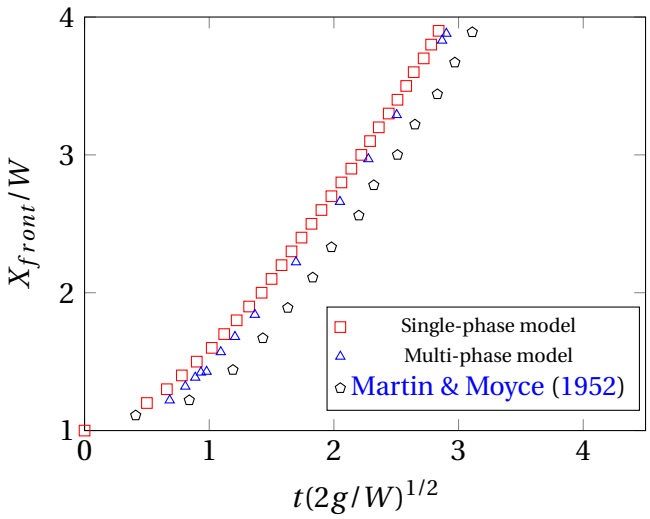

Figure 5.47: Time evaluation of the front of a collapsing water column $W = H/2, D = 2H$, for single and multi-phase models and compared to experimental data, Martin & Moyce (1952).

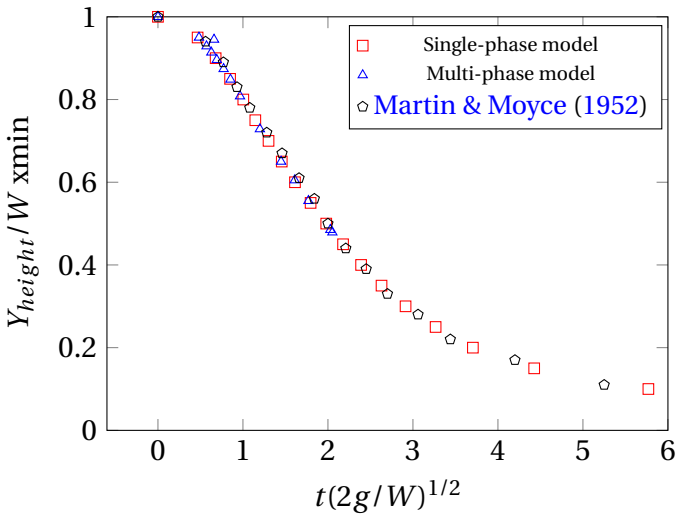

Figure 5.48: Time evaluation of the height of a collapsing water column $W = H/2, D = 2H$, for single and multi-phase models and compared to experimental data, [Martin & Moyce (1952)].

5.5 High resolution simulation of the dam break cases

Here, the two dam-break cases simulated in section 5.4.3 have been re-simulated using a high number of particles (over 300,000). The results will be again compared with Mokos et al. (2017). As we mentioned in

section 5.4.3, Mokos et al. (2017) void formation, occurred in the multi-phase simulation when they used (over 200,000 particles) initial particle spacing less than $\delta x = 0.008h$, where h is initial height of the water. Voids appeared when the water impacted the wall and also after the jet overturned. In the case of 5.1.2, the void appeared after overturning in the water and under the jet of water. However, the 5.1.2 case was shown inside the entraining air. This phenomenon is investigated with our model.

5.5.1 Case One: $W = 2H$

- Using background pressure for both phases

Figure 5.49 and 5.50 show a comparison between present simulations and those of Mokos et al. (2017) using background pressure for both phases. As seen in Figures 5.49 (right) and and 5.50 (right) by adding background pressure for both phases, no voids appeared in the air pocket. The interface between the two phases is smooth. There are some differences between the two results: the air pocket is smaller in the present simulation and the water jet is slightly higher than Mokos et al. (2017). Using a shifting algorithm due to, Xu et al. (2009*b*), with artificial viscosity leads to a change in the water jet as shown in Figure 5.49, where the water jet is shorter and higher, Mokos et al. (2017). In contrast, in the present work, the water jet is slightly longer and lower, but the interface between the two phases is smoother.

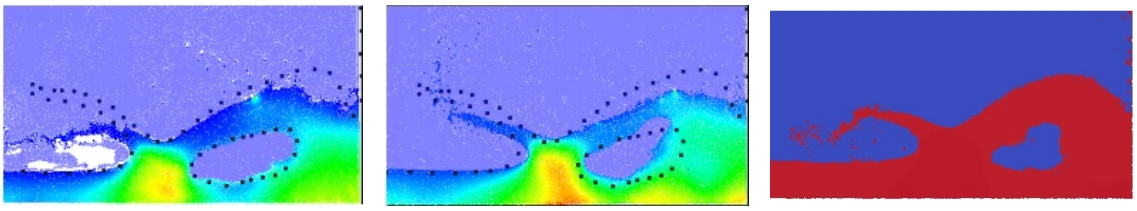

Figure 5.49: Comparison with a Mokos et al. (2017) without shifting (left) and Colicchio et al. (2005) shows as a dot, using artificial viscosity, shifting algorithm (centre) and present result with background pressure (right) at $t = 6.76$ for 368640 particles.

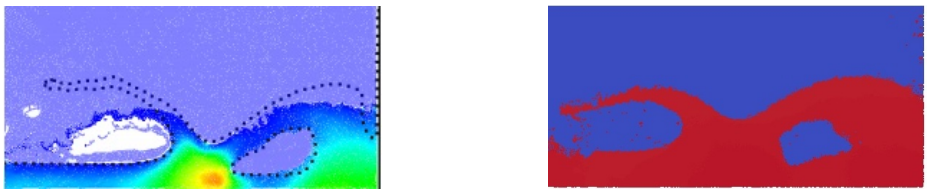

Figure 5.50: Comparison with Mokos et al. (2017) without shifting (left) and Colicchio et al. (2005) shows as a dot with present result with background pressure (right) at $t = 7.14$ for 368640 particles.

5.5.2 Case Two: $H = 2W$

- Using background pressure only for water phase

The results presented in Figure 5.51 show a comparison between using background pressure only for the water phase and no background pressure for either phase. When the background pressure is not employed for either phase, a void will be created within the air pocket after the returning jet overturns and is under the overturning water jet, see 5.51 (left). By adding background pressure to the water phase, the void under the water jet will disappear, but there is still the gap between water and air particles inside the entrained air pocket, see 5.51 (right). Figure 5.52 shows the results between Mokos et al. (2017) without shifting algorithm (left) and present simulation without background pressure (right). The

free surface which can be seen in the present study is smoother, but there is a void under the water jet which in the Mokos et al. (2017) results does not appear. In addition, the jet shape is completely different.

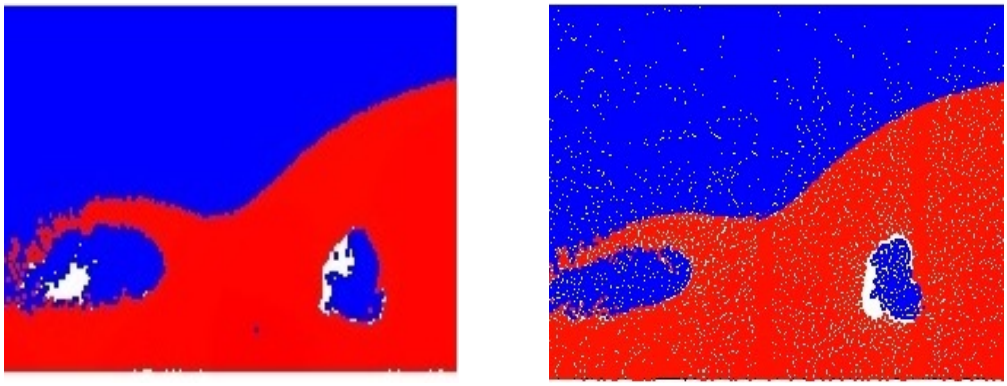

Figure 5.51: Comparison between using background pressure: (left) without background pressure in either phase and (right) with background pressure only for water phase at $t = 6.76$ for 368640 particles.

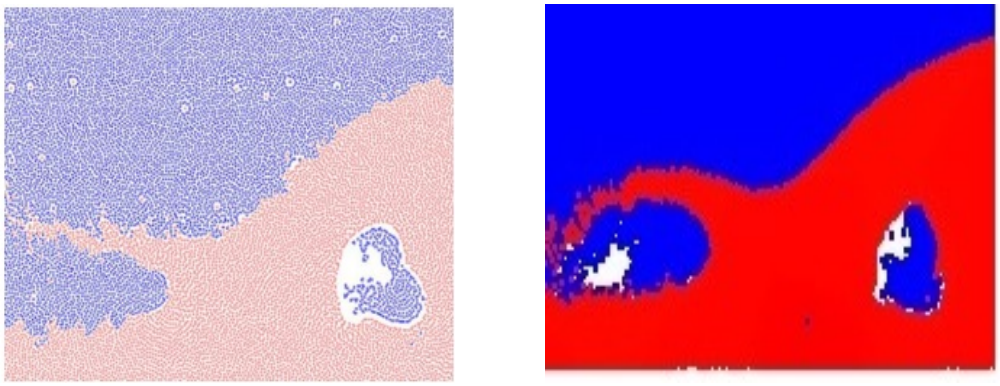

Figure 5.52: Comparison with a Mokos et al. (2017) without shifting in both phase and surface term only in the water phase (left) and present result without background pressure in both phase (right) at $t = 6.76$ for 368640 particles.

- Using background pressure for both phases

In Figure 5.53, the present simulation using background pressure for both phases is compared with Mokos et al. (2017) using both shifting and surface term. In both results the voids have disappeared, but the entrained air packet inside the water is smaller in the present study (right) than in Mokos et al. (2017) (left) and the jet shape of water is longer in the Mokos et al. (2017) result than the present study.

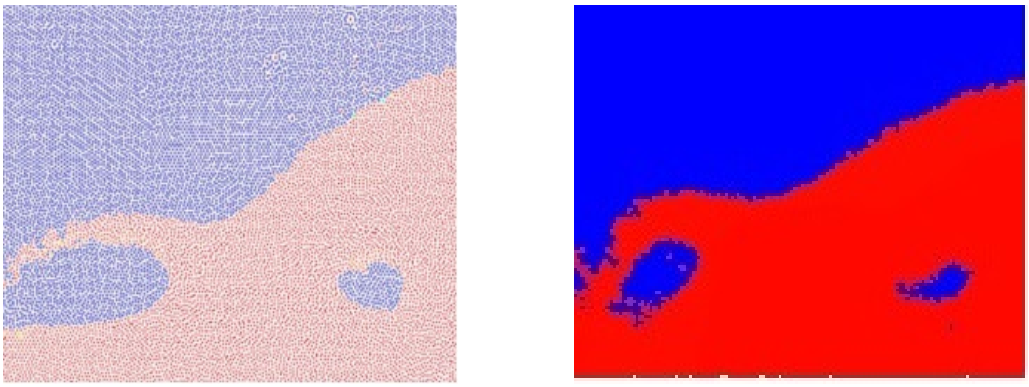

Figure 5.53: Comparison with a Mokos et al. (2017) shifting in both phase and surface term only in the water phase (left) and present result with background pressure in both phase (right) at $t = 6.76$ for 368640 particles.

5.6 Conclusion

As SPH for the simulation of multi-phase has been presented. Several simulations have been performed, namely Rayleigh-Taylor instability, bubble rising and two different dam-break cases. The results are compared to other numerical and SPH results; the level of agreement between this work and other results is in general acceptable. An SPH formulation for the simulation of multi-phase fluid flows has been presented. In this

study, to control any pressure fluctuation, the density re-normalisation method (Shepard filter, Shepard (1968)) has been employed every 15 time steps. To deal with the high density ratio at the interface between water and air, density re-normalization was applied for each phase separately. The laminar viscosity term by Morris et al. (1997) has been used to ensure the numerical stability of the simulation. A background pressure has been applied to prevent the formation of unphysical voids in the less dense phase at high resolutions, instead of shifting algorithm, Mokos et al. (2017) for higher resolutions. As he showed, shifting algorithm affected the shape of the overturning wave as the background pressure does. The background pressure also increased the pressure field. Using the shifting algorithm computationally is expensive as we need to apply to all particles and find out which particle has to move.

CHAPTER 6

VALIDATION: 3D CASES

Contents

In this chapter, 3D single-phase and 3D multi-phase models have been developed. Two cases of dam break which were simulated in chapter 5 will be investigated in this chapter for comparison between SPH single, multi-phase, 2D and 3D with experimental results. 3D simulations are more realistic than 2D simulations but are also more expensive thus parallel code is necessary.

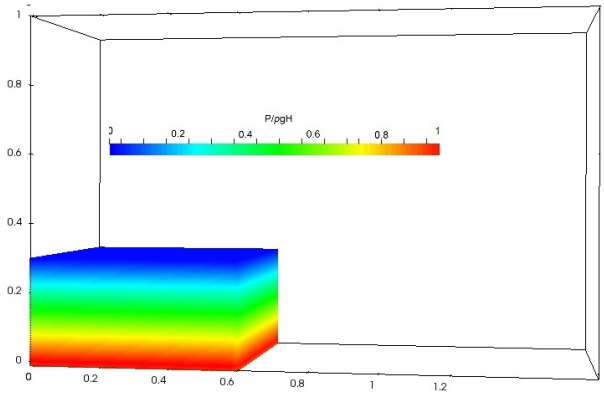

Figure 6.1: Initial particle configuration of the 3D dam break

6.1 3D Single Phase

6.1.1 Validation: Case One

In this simulation the height of the water is selected as 0.3 m, the length of the tank is 1.60 m and width is 0.6 m as shown in Figure 6.1. The particle spacing dx is 0.005 m and a total of 864000 particles are used in this simulation and $\Delta t = 1.15 \times 10^{-4}$ is the time step. The density of the water is 1000 kgm^{-3} and dynamic viscosity 10^{-3} kg/ms. In this simulation no-slip boundary conditions are employed on solid walls. The non-dimensional parameters for time and front position are given by $t^* = t\sqrt{g/H}$ and $x^* = x/H$. Figure 6.2 shows the pressure distribution for the 3D dam break at $t^* = 1.7$ and 2 before impact with the wall. After initial release, it takes about $t^* = 2.2816$ for the water to collide with the vertical wall on the right side and the impact increases the particle pressures at the bottom right corner, see Figure 6.3 (left). The pressure contours are shown in Figure 6.2 and 6.3 show the pressure field is smooth compared to the

single phase 2D which was shown in Figure 5.41 (left). The snapshot of

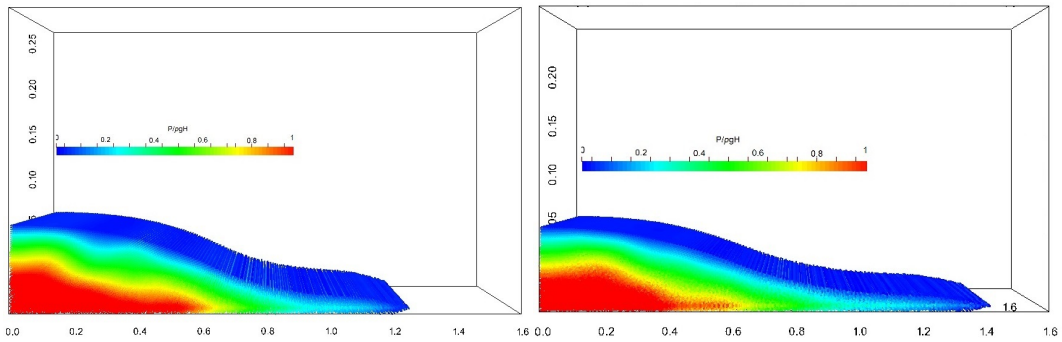

Figure 6.2: Pressure contours of a 3D dam break (left) $t(g/H)^{1/2} = 1.7$ (right) $t(g/H)^{1/2} = 2$

the water after flow impact at time $t^* = 4.8$ is presented in Figure 6.3 (left). After impacting the wall, the fluid particles move upwards and they make a water column on the right side, then start to overturn as shown in Figure 6.3 (right).

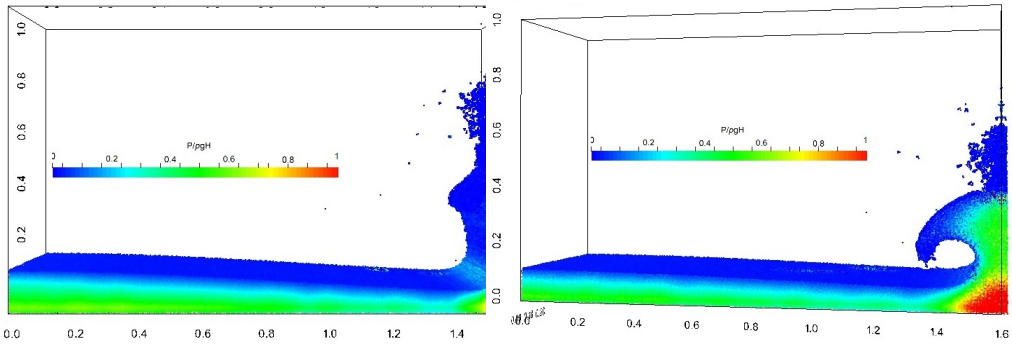

Figure 6.3: Pressure contours of a 3D dam break (left) $t(g/H)^{1/2} = 4.8$ (right) $t(g/H)^{1/2} = 5.7$

Figure 6.4 shows the pressure field at $t^* = 6.2$ (left) and 7.4 (right) after the water column moves downward and creates another wave, but in the opposite direction. The 3D simulation shows the free surface and pressure field are smoothed well, compared to the 2D case (see Figure 5.9).

Splashing particles and the water jet in the 3D model are well preserved. In the 3D case, the front position particles are not uniform, and for this

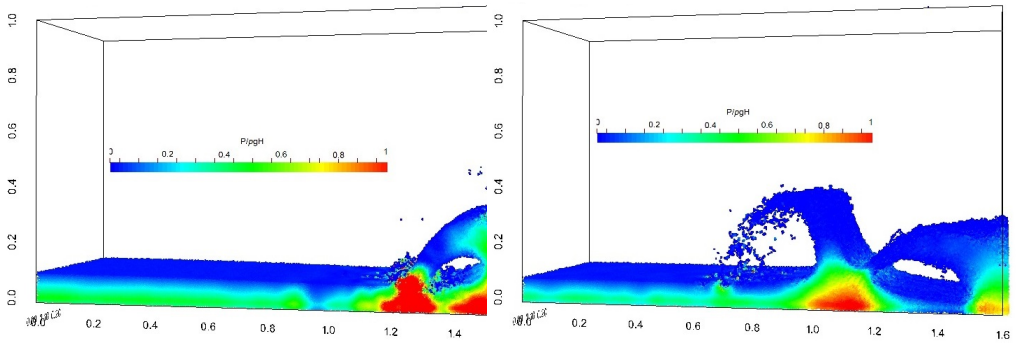

Figure 6.4: Pressure contours of a 3D dam break (left) $t(g/H)^{1/2} = 6.2$ (right) $t(g/H)^{1/2} = 7.4$

reason to plot the toe position overall particle positions are averaged. The toe position results obtained from the 3D simulation compare well with results from Colagrossi & Landrini (2003) and from other 2D simulations (see Figure 6.5). The pressure profile at $x/H = 5.3366$, $y/H = 0.19$ and $z/H = 0.5$ on the right wall (using the SPH sum) is plotted in Figure 6.6 and compared with Colagrossi & Landrini (2003), 2D SPH simulations, Buchner (2002) and experimental results (Zhou et al. (1999)). The result compares well with the other SPH, numerical and experimental results.In general, the pressure profile plot captures the experimental result (Zhou et al. (1999)) with slight delay.

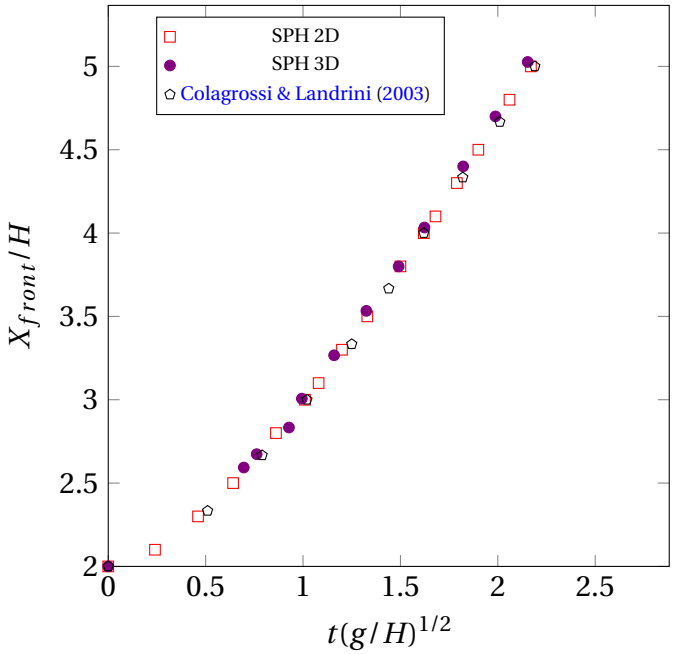

Figure 6.5: Time evaluation of the front of a collapsing water column for 2D and 3D compared to Colagrossi & Landrini (2003).

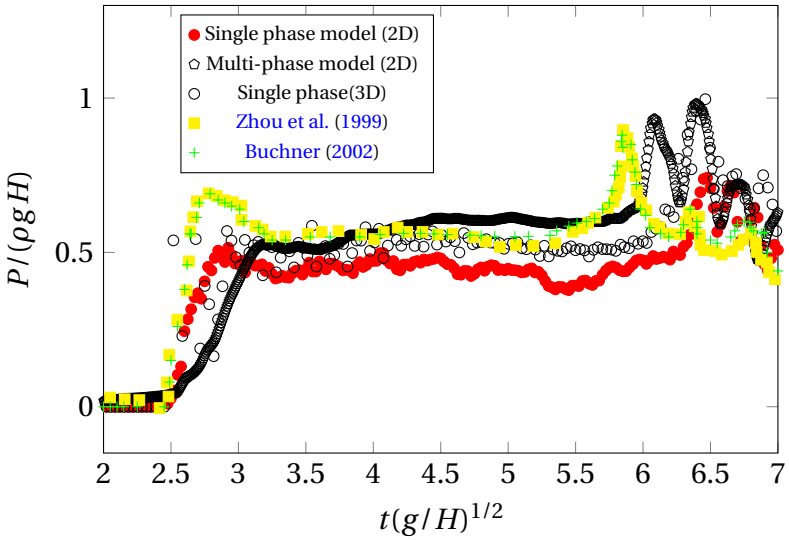

Figure 6.6: Comparison of pressure profile at $x = 1.601$, $y = 0.19H$ and $z = 0.15$ with Colagrossi & Landrini (2003), 2D SPH simulations, Buchner (2002) and experimental results (Zhou et al. (1999)).

6.1.2 Validation: Case Two

In this section the 3D simulation of dam break was investigated in chapter 5, section 5.1.2 will be performed. The dimensions of the dam break are shown in Figure 6.7 (0.4x0.15x0.9 m in x, y and z directions) and particle spacing is 0.0025 m with 192000 particles used in this simulation. Parameters employed in this simulation are $\rho = 1000$ kg/m^3, $\mu = 10^{-3}$ kg/ms and $\Delta t = 5.75 \times 10^{-6}$ s. The water column starts to collapse under the effect of the gravity and results are displayed in Figures 6.8 (left). After $t^* = t(2g/W)^{1/2} = 2$, the water flow will hit the opposite wall and will get the high pressure at the bottom corner 6.8 (right). The snapshots of the water flow at time $t^* = t(2g/W)^{1/2} = 4.8$ and 5.7 are presented in Figure 6.9 and show the opposite wave is created after the water overturns. The comparison of front position and height of water in our 3D simulations have been plotted in 6.10 and 6.11. They show the 3D simulation is agreed well with other SPH and experimental results (Martin & Moyce (1952)).

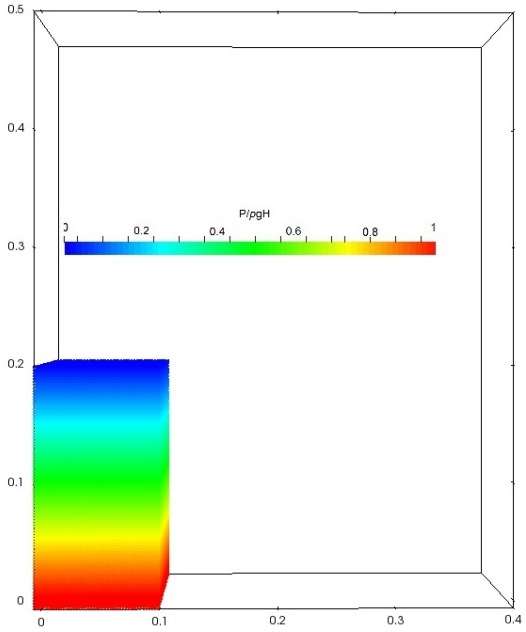

Figure 6.7: Initial particles configuration of the 3D dam break.

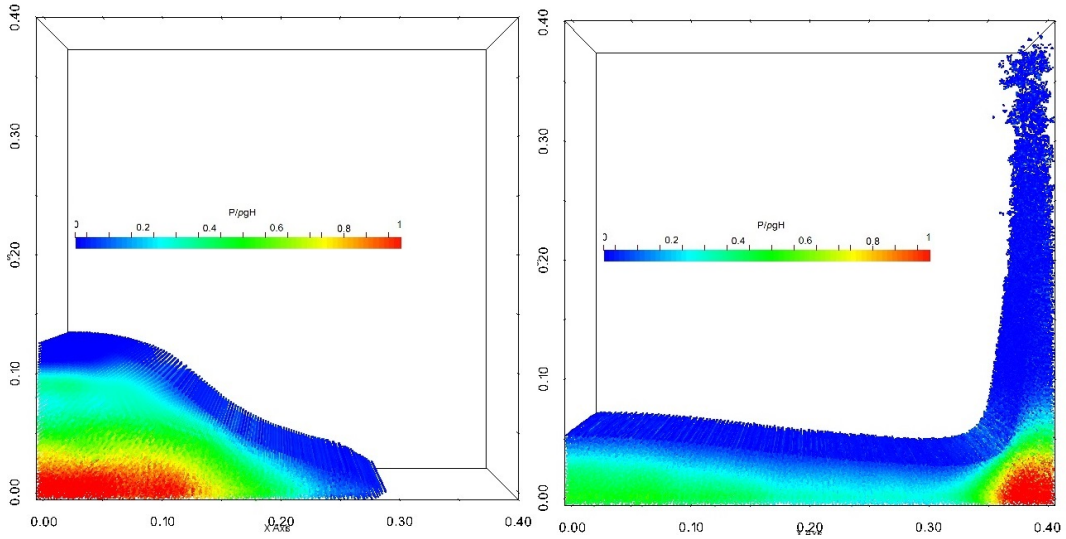

Figure 6.8: Pressure contours of a 3D dam break (left) $t(2g/W)^{1/2} = 2.1$ (right) $t(2g/W)^{1/2} = 4.4$

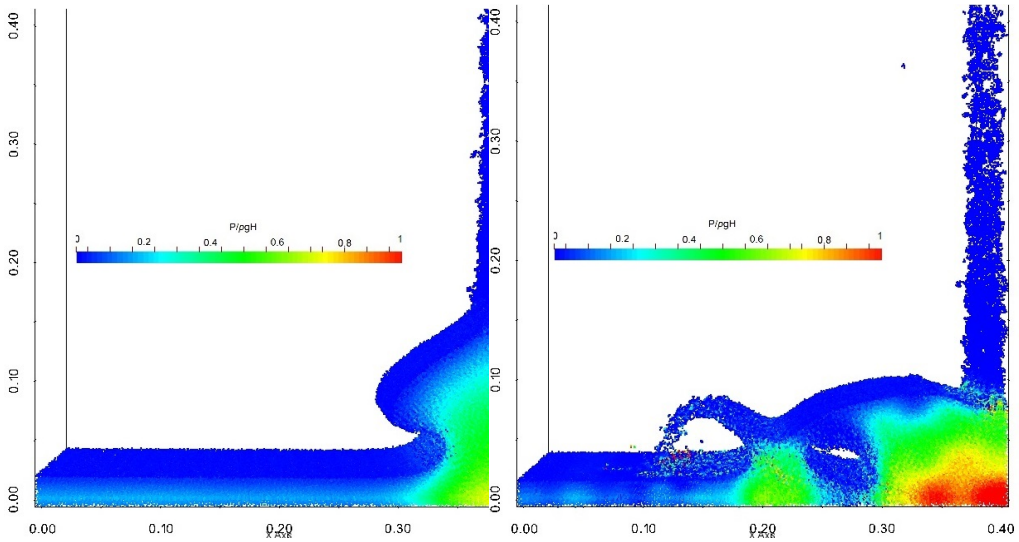

Figure 6.9: Pressure contours of a 3D dam break (left) $t(2g/W)^{1/2} = 8.1$ (right) $t(2g/W)^{1/2} = 9.5$

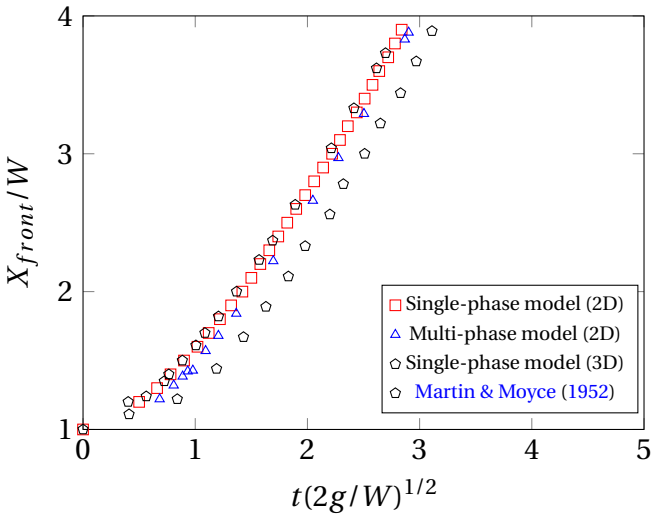

Figure 6.10: Time evaluation of the front of a collapsing water column $W = H/2, D = 2H$, for single, multi-phase model and 3D, compared to experimental data, Martin & Moyce (1952).

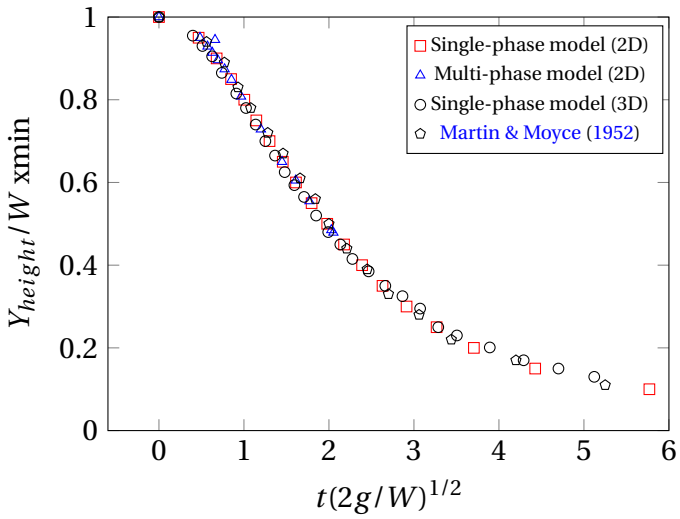

Figure 6.11: Time evaluation of the height of a collapsing water column $W = H/2, D = 2H$, for single, multi-phase model and 3D compared to experimental data, [Martin & Moyce (1952)].

6.2 Conclusion

The single-phase dam-break cases in this section have been developed in 3D and results compared with experimental results, Zhou et al. (1999), Martin & Moyce (1952) and other numerical data, Buchner (2002) and Colagrossi & Landrini (2003) for the toe and height of the water column. In general, all results are agree well with the experimental and other numerical results. The second peak of pressure field in Figure 6.6 was slightly delayed compared to the experimental results, due to the lack of the air phase.

6.3 3D Multi-phase

In this section the multi-phase dam break model will be extended to 3D. Both cases simulated in sections 6.1.1 and 6.1.2 will be investigated. The water column height and the position of the surge front, as well as the pressure at the wall, will be compared. Here, the boundary conditions are used as they have been applied on 2D simulations plus free-slip on side boundaries $y = 0$ and $y = n_y$.

6.3.1 Validation: Case One

The sketch of the 3D multi-phase set up is shown in Figure 6.12. The dimensions and particle spacing of the dam break are the same as for the single-phase (the particle spacing in x, y and z directions is $dx = dy = dz$=0.005 and the number of particles used in x, y and z directions are 320, 120, 200), giving a total of 7680000 particles of which 120 x 60 x 120 are water particles and the remainder are air. Figures 6.13 to 6.16 show the motion of the water at different times. As we can see from Figure 6.17, there is not a significant change in the motion of the water jet when the air phase is taken into account. The toe position results from 3D multi-phase agrees well with Colagrossi & Landrini (2003) and other simulations (see Figure 6.17). Next, we compare the pressure measurement on the vertical wall during and after the jet impact.

To measure the pressure, we set the pressure sensor on the vertical wall 0.19H above the right-hand side of water tank. The results are shown

in Figure 6.18 and compared with single and multi-phase 2D, 3D single phase, Zhou et al. (1999) and Buchner (2002). The peak pressure at the start of impact is in good agreement with Zhou et al. (1999) and Buchner (2002), but at the second peak pressure after impact, there is a slight delay and compared to Zhou et al. (1999) and Buchner (2002) and the results showed from 3D multi-phase are in well captured the experimental results. As we see, the second peak pressure in 3D multi-phase shows reduced oscillation compared to the other simulations.

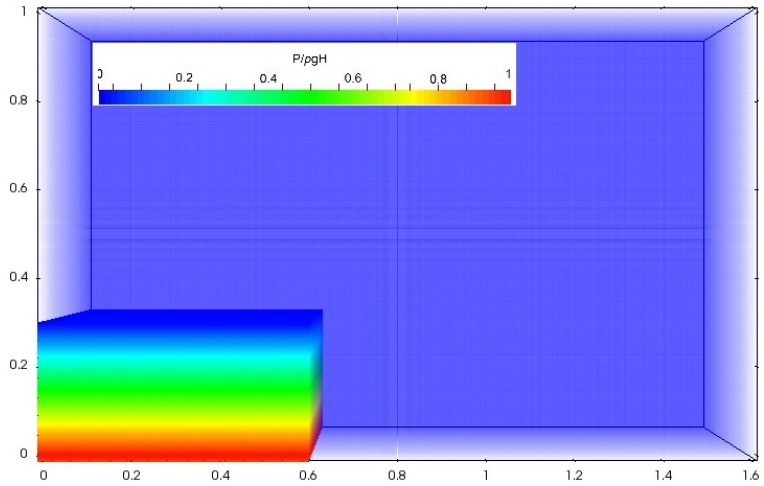

Figure 6.12: Particle configuration of the 3D dam break

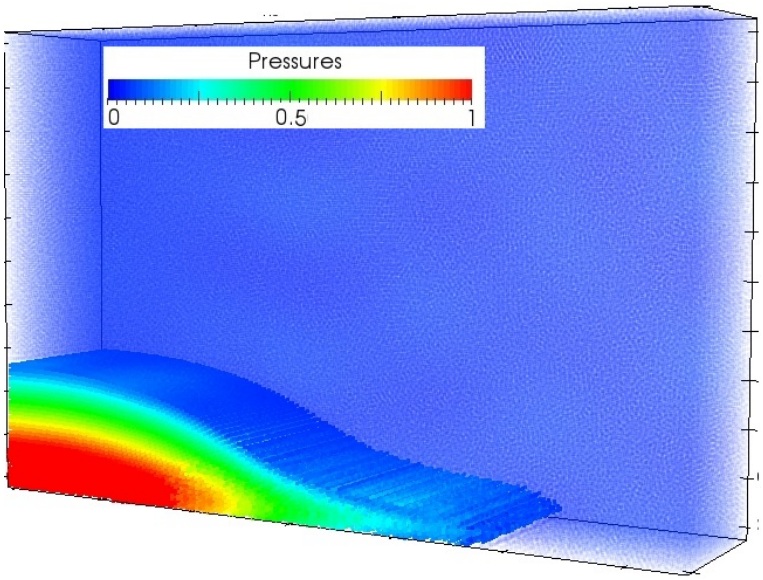

Figure 6.13: Initial particles configration of the 3D dam break.

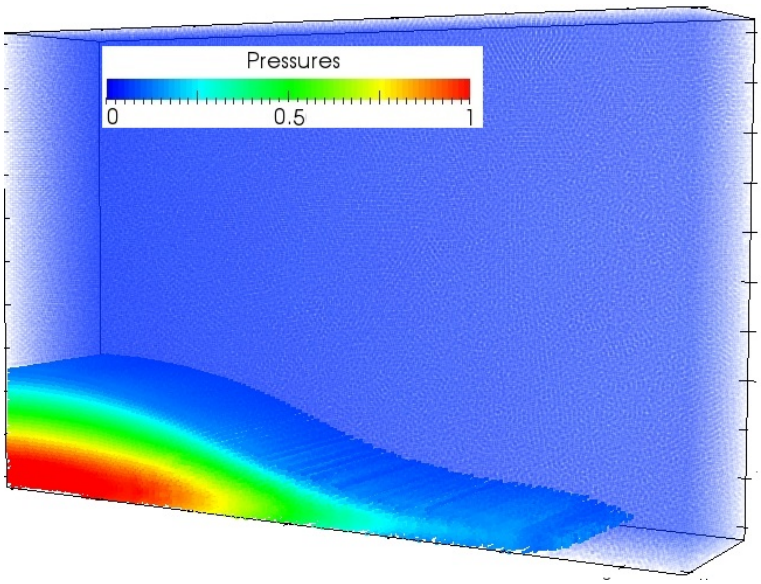

Figure 6.14: Pressure contours of a 3D dam break at $t(g/H)^{1/2} = 2$.

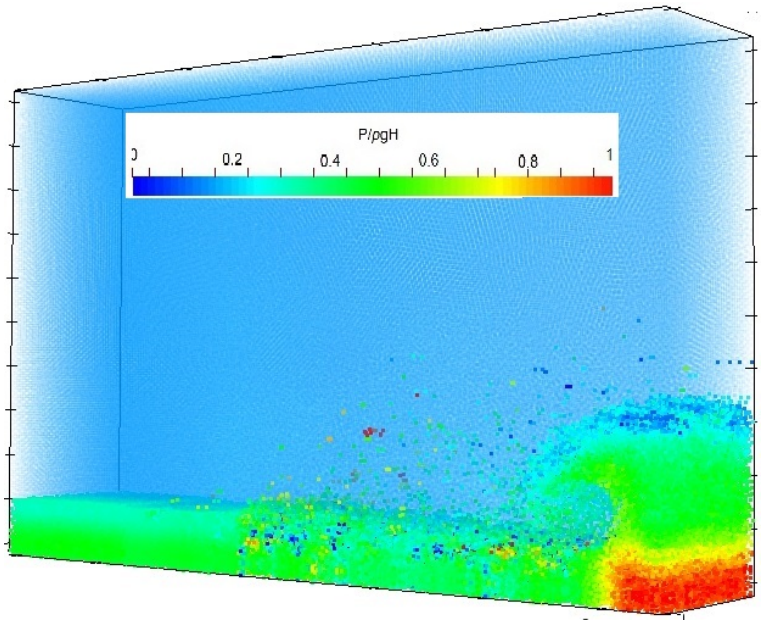

Figure 6.15: Pressure contours of a 3D dam break at $t(g/H)^{1/2} = 5.7$.

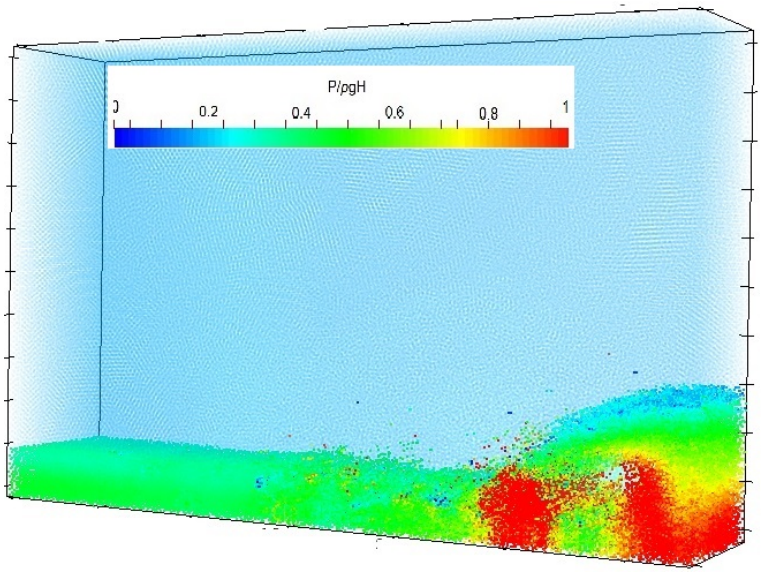

Figure 6.16: Pressure contours of a 3D dam break at $t(g/H)^{1/2} = 6.2$.

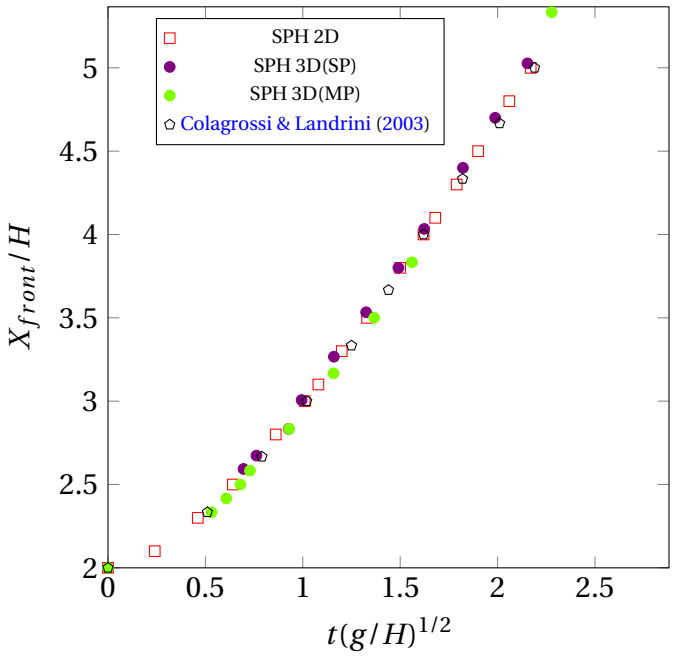

Figure 6.17: Time evaluation of the front of a collapsing water column for 2D and 3D compared to Colagrossi & Landrini (2003).

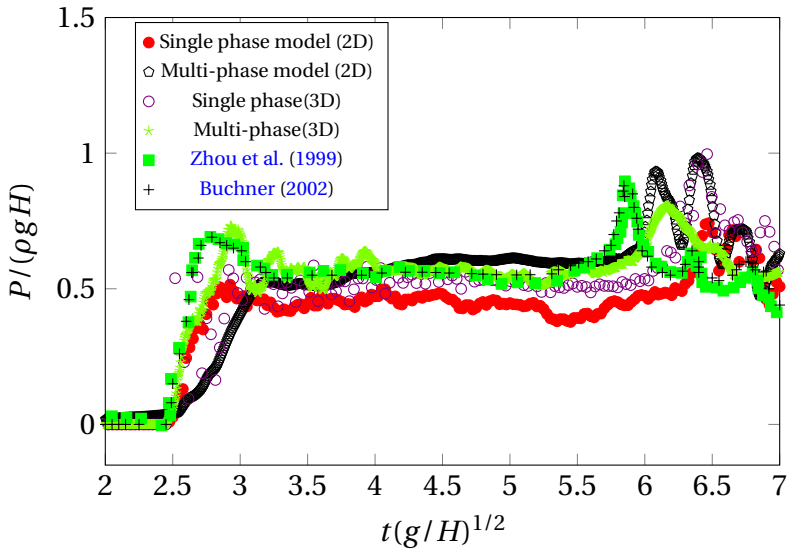

Figure 6.18: Comparison of 3D multi-phase pressure profile with Colagrossi & Landrini (2003), 2D SPH simulations, Buchner (2002) and experimental results (Zhou et al. (1999)).

6.3.2 Validation: Case Two

Here, we consider the dam-break problem studied by Martin & Moyce (1952). Figure 6.19 (Left) displays a sketch of the configuration and he dimensions and particle spacing ($dx = dy = dz$=0.0025)of the dam break are the same as for the single-phase. The number of particles to be used in this simulation is 3456000 which 40x60x80 are water particles in x, y and z directions and the remainder are air. At $t = 0$, water starts collapsing under the effect of the gravity. Figures 6.19 and 6.20 illustrate the velocity contours and the motion of water at different times.

The comparison of the front position and height of water in our 3D multi-phase simulation with experimental results and other simulations are plotted in Figures 6.21 and 6.22. The results show the 3D multi-phase simulation results are in a good agreement with the experimental data and are similar to the single-phase simulations.

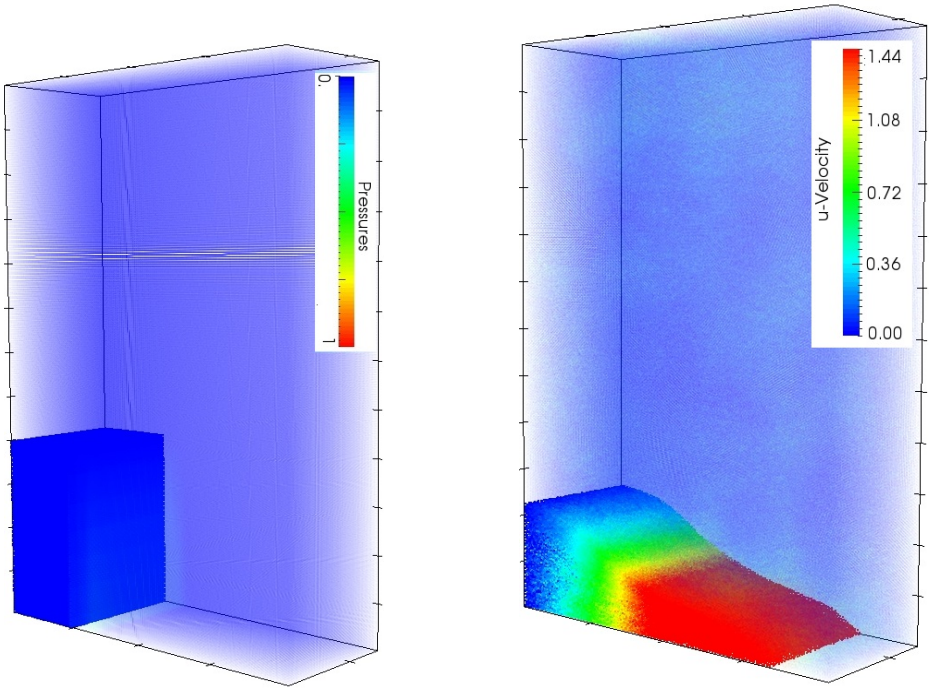

Figure 6.19: Initial particle configuration of the 3D dam break (Left) and velocity contours of a 3D multi-phase dam break problem at $t(2g/W)^{1/2} = 2.5$ (Right).

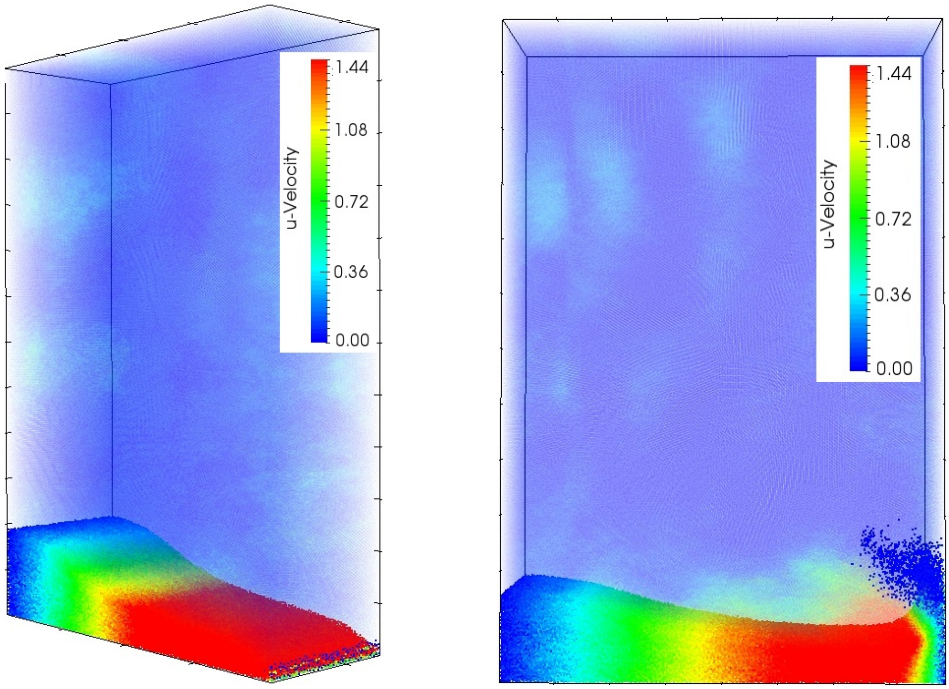

Figure 6.20: Velocity contours of a 3D multi-phase dam break problem at $t(2g/W)^{1/2} = 3$ and $t(2g/W)^{1/2} = 3.5$

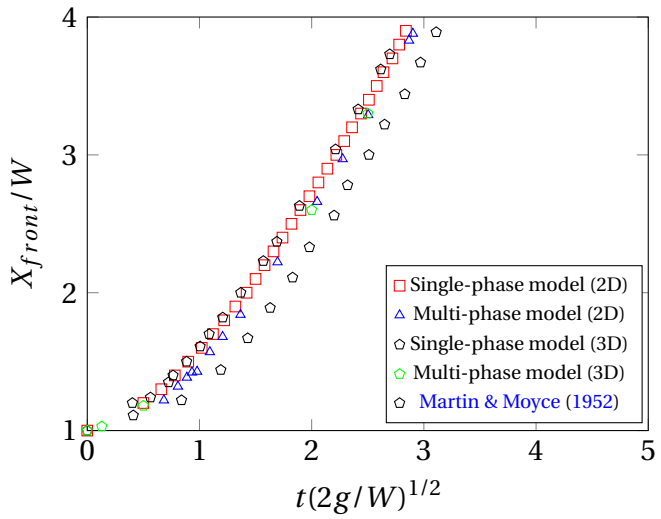

Figure 6.21: Time evaluation of the front of a collapsing water column $W = H/2, D = 2H$, for 2D-3D single, multi-phase models, compared to experimental data, Martin & Moyce (1952).

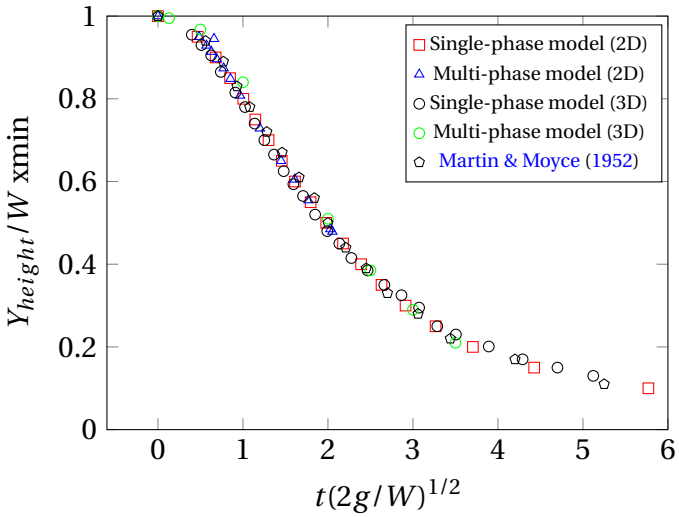

Figure 6.22: Time evaluation of the height of a collapsing water column $W = H/2, D = 2H$, for 2D-3D single, multi-phase models and compared to experimental data, [Martin & Moyce (1952)].

6.4 Conclusion

The 3D single-phase dam-break cases in this section have been extended to the multi-phase and compared with experimental and other numerical results, Zhou et al. (1999), Martin & Moyce (1952), Buchner (2002) and Colagrossi & Landrini (2003) for the front and height of the water column and pressure values on the right wall. The pressure oscillation is reduced in 3D multi-phase and the second peak pressure is closer to the experimental result compared to the single-phase. The reason may be due to some air particles become entrapped inside the water particles in the multi-phase model. In general, corresponding to the single-phase results, the 3D multi-phase results are improved and generally in good agreement with experimental and other numerical results. There is no significant influence on the free surface and water front position. But there are some particles splashing around the fluid after impact the right wall.

The parallel code has been used to simulate these two 3D multi-phase cases. The total number of particles 7680000 and 3456000 were used for case one and case two, respectively. The domain was divided to equal pieces in $x-$ direction and each processor received the same number of particles. This balance will be kept during the whole simulation.

CHAPTER 7

VALIDATION: SIMULATION OF 2D AND 3D FLAT PLATE IMPACT

Contents

7.1 Introduction

In this chapter, we use an SPH method to simulate the impact of a flat plate on a water surface, as carried out experimentally in the FROTH project at Plymouth University, Mai (2017). The geometry of the impact

plate is shown in Figure 7.1 (left). The plate was held by two driver plates with varied mass from 32 kg to 52 kg. The falling plate was dropped with impact velocity between 4 m/s to 7 m/s. In the experiments the pressure at the five different points was measured by pressure transducer Model XPM10 installed on the plate at locations shown in Figure 7.1 (right).

The main aim of our study is to simulate the flow due to the impact of a flat plate on pure and aerated water surfaces and, in particular, to evaluate the loading pressure on the flat plate at the time of the entry. The flat plate is 250mm long and 250 mm wide with a 12mm thickness. The actual experimental impact velocity time series will be used in our simulations, Ma et al. (2016) and Mai (2017). The velocity at each time steps was integrated from the data calculated by accelerometer model 4610 located on the top of the plate. A novel feature of the experiments

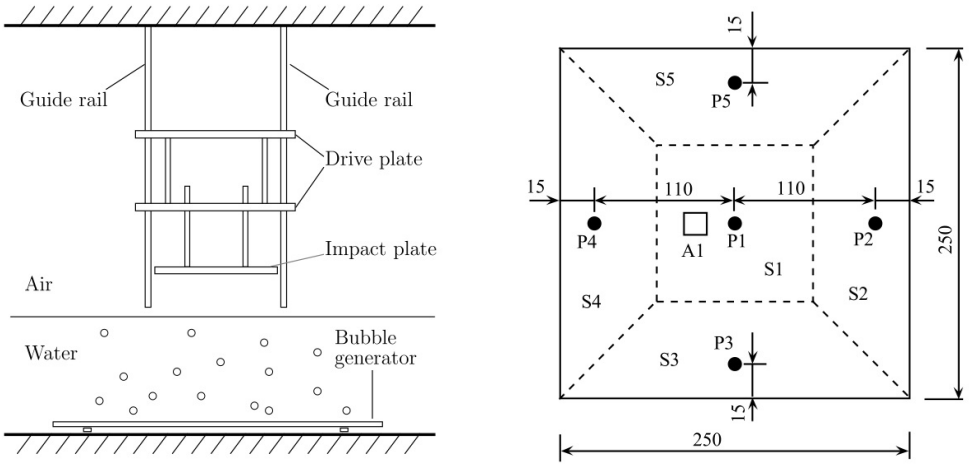

Figure 7.1: A sketch of experimental model and configuration of the instrumentation on the plate on the $P_1 - P5$ are pressure sensors, $S_1 - S5$ are influence region and A_1, is the accelerometer, Mai (2017).

was that, in order to mimic wave/structure impacts, the water was aerated

by bubbling air from underneath the water surface. This created a non-homogeneous, compressible mixture.

The sound speeds used in this study are much larger than ten times the maximum fluid velocity u_{max} and are set as physical sound speeds determined by aeration levels in the water-air mixture. Figure 7.2 illustrate the speed of sound in a water-air mixture.

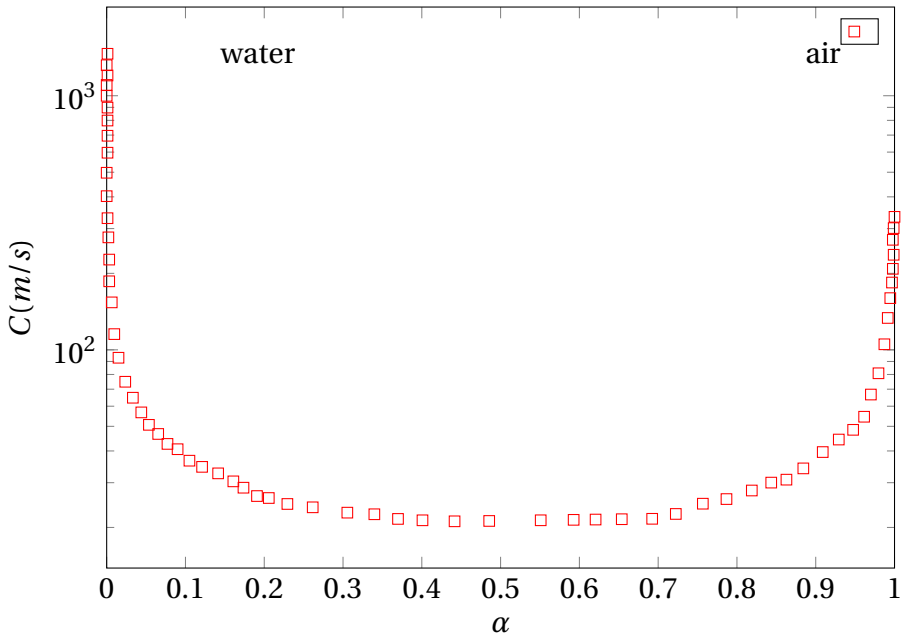

Figure 7.2: The speed of sound in water-air mixture at one atmospheric pressure and 15 C. c is speed of sound, α is volume fraction, Brennen (1995).

We use the following equation, Brennen (1995), to find the speed of sound at the different aeration levels:

$$\frac{1}{c^2{}_w} = \frac{\alpha}{kp}(\rho_l(1-\alpha) + \rho_g\alpha) \tag{7.1}$$

where c is speed of sound, α is aeration level, ρ_l and ρ_g are densities of fluid and air, respectively. k is constant and is taken as 1. For pure water, we use speed of sound 700 m/s which was the maximum possible speed of

sound that would give stable simulations. From equation 7.1, the speeds of sound used for aerated levels of 0.75%, 1.02% and 1.6% were 122 m/s, 107 m/s and 86 m/s, respectively. As we mentioned in section 3.9.1, the time step is chosen with a minimum of three conditions and limited for the stability reason and also the Mach number needs to be less than 0.1. On the other hand, in this simulation, the time step is constant and read from the experimental data which is not small enough for multi-phase simulations. For example, step size of time in experiment is 0.2×10^{-5} but for multi-phase flow with aerated level 0.78% the time step required is 0.994410×10^{-6}. To fix this issue we interpolate the experimental plate velocity as it enters the water and this is used as a boundary condition for the SPH model and the experimental plate velocity containing velocity fluctuations.

7.2 Solid discretization

Dealing with more than one phase needs some extra care to ensure correct enforcement of boundary condition at interfaces. The solid particles on the interface are treated as a boundary for the fluid phase. Applying an extra procedure for solid particles is needed.

7.2.1 Rigid body discretization

Referring to Figure 7.3, the ghost images of the upper blue particles are the particles coloured black. The images of the lower blue particles are

coloured green. The upper blue particles interact only with the black particles, whereas the lower blue particles interact only with the green ones.

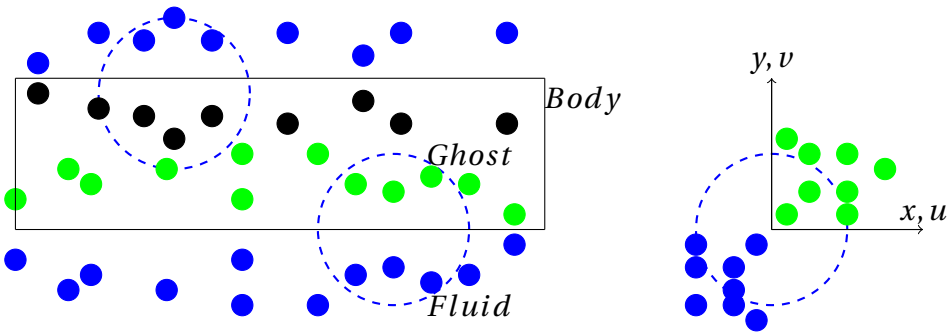

Figure 7.3: Schematic of particles close to the body (left) and close to the corner (right).

7.2.2 Moving bodies with SPH

As we mentioned in a previous section, when the particles approach the boundary, a ghost particle will be created. In this technique, the approaching particles on each side of a body will create the image of fluid particles inside the body. We follow the following step: if the ghost particle j belongs to the same side of the body boundary as particle i, see Figure 7.3, it is taken into account to find the acceleration and density of the particle i. Finally to move the body, here we use the experimental velocities data (Mai (2017)) and interpolate the velocity at each time step. The interpolated value is used to move the plate. This is expressed as

$$y_{iG} = 2y_{body} - y_i$$

$$x_{iG} = x_i$$

$$v_{iG} = 2v_{body} - v_i$$

$$u_{iG} = -u_i$$

$$\rho_{iG} = \rho_i$$

$$p_{iG} = p_i$$

where v and u are the tangential and normal velocity to the plate boundary, respectively. The reason for using these conditions is to prevent non-penetrating particles from going through the plate and to provide kernel support close to the solid boundary.

7.3 Simulation of 2D Single Phase impact flat plate

The motion of a flat plate dropping onto water has been investigated experimentally in the FROTH project at the Plymouth University. Figure 7.4 shows the computational set up corresponding to the experimental tests for both pure water and entrained water with air bubbles, Ma et al. (2016) and Mai (2017). The impact velocity is between 4 m/s and 7 m/s,

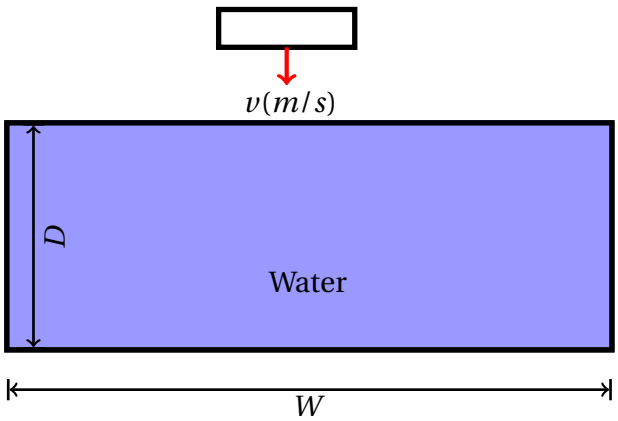

Figure 7.4: Schematic representation of impact of a flat plate

by adjusting the initial position of the flat plate. In 2D simulation, the

pressure has been measured at three points during impact, see Figure 7.5.

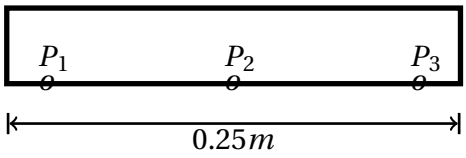

Figure 7.5: Schematic representation of 2D of a flat plate

Flat plate impact calculations are compared with experimental data for a given initial velocity. We use 240000 particles to discretize the domain and the time step was set at $\Delta t = 0.2 \times 10^{-5}$. The domain of water tank in the experiments was 35m long and 15.5m wide and 1m deep. In this study, to decrease the computational time we reduce the computational domain size from 35 m to 6 m long and from 15.5 m to 6 m wide but the same depth as the experiments has been used. The reduction of computational domain did not affect the results. We set 0.1 m as the initial distance between the flat plate and free surface of the water. Following Ma et al. (2016), we shifted all time series to correlate the first peak pressure at P_2 to time $t = 0$.

7.3.1 Fresh water entry

Firstly the fresh water (0% aeration) is considered. Figures 7.6 and 7.7 show the comparison of the time series of gauge pressure at the centre of the plate for impact velocities of $v = 4$ m/s, $v = 5$ m/s and $v = 7$ m/s, respectively. The SPH results agree reasonably well with experimental results, Mai (2017), and in general, the SPH method and FROTH project

at Plymouth University experiments give close peak pressure. The peak pressure for $v = 4$ m/s is almost similar, but for $v = 5$ m/s and $v = 7$ m/s, the peak pressure in our simulations is lower than experimental results. There is pressure oscillation after impact in experimental results, but we can not get that in our simulations due to the air phase not being taken into account. The small peak pressure is found after high peak in our simulations which is as a result of the reflecting pressure wave after flat plate impact.

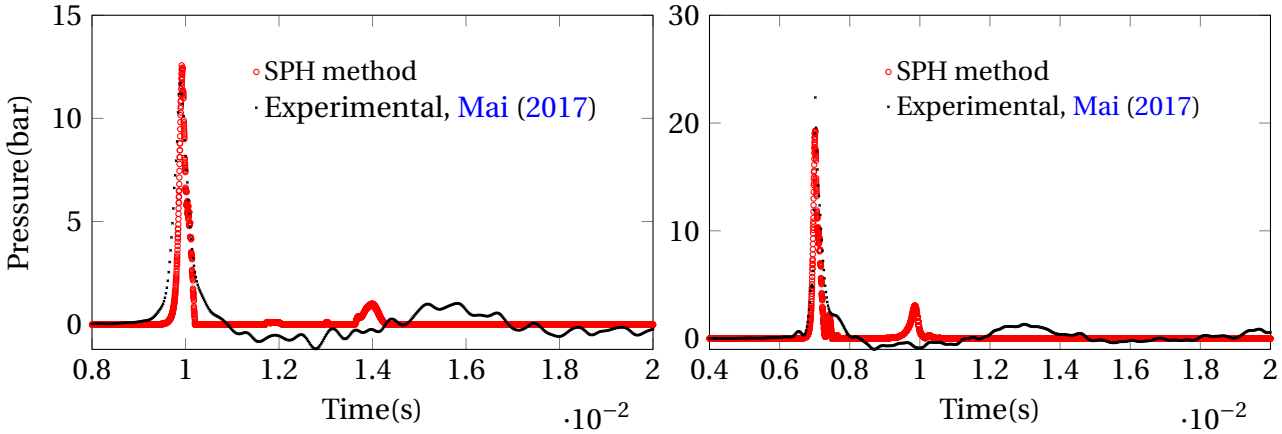

Figure 7.6: (left) Pressure distribution on the plate at p_2 with unaerated for $v = 4$ m/s. (right) Pressure distribution on the plate at p_2 with unaerated for $v = 5$ m/s.

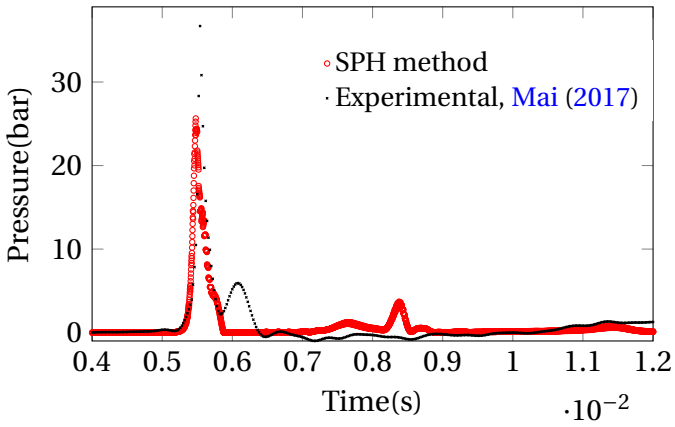

Figure 7.7: Pressure distribution on the plate at p_2 with unaerated for $v = 7$ m/s.

Figure 7.8 shows the pressures are not equally distributed on the plate, with the pressure going up from edges of the flat plate to the centre. Table

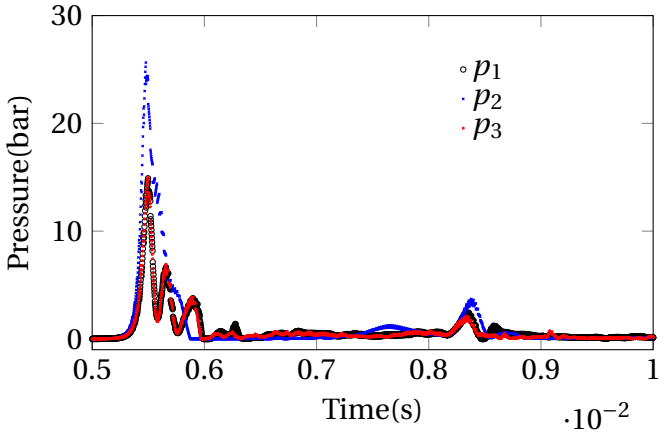

Figure 7.8: Pressure distribution on the plate at p_1, p_2 and p_3 with unaerated for $v = 7$ m/s.

7.1 shows a comparison between experimental and numerical values of the pressure impulse evaluated at point p_2 for the unaerated water impact at impact velocities of 4 m/s, 5 m/s and 7 m/s.

The impact pressures are high, but act over the water surface for a short period of time, so the integrated load over the plate during the impact will be investigated and compared with Ma et al. (2016). The pressure impulse is defined as time integral of the pressure over the duration of an impact event. The comparison is in good agreement (see Table 7.1) with experimental results. The pressure impulse is approximated here as:

$$I = \frac{1}{2}(p_{max}(t_{up} + t_{dn})), \tag{7.2}$$

where p_{max} is the maximum impact pressure and (t_{up} and t_{dn} are the rise and fall times of the maximum pressure).

	$v = 4$ m/s		$v = 5$ m/s		$v = 7$ m/s	
	Experimental	SPH	Experimental	SPH	Experimental	SPH
P_2(Pa s)	–	348	652.46	627	783.27	724

Table 7.1: Pressure impulses of impact on the plate for pure water entry is calculated before and after shock

Before water separation, that is, water splashing around the plate, as shown in Figure 7.9 (left), the maximum pressure is located in the center of the plate and the top center of the water. Figure 7.9 (right) displays the pressure distribution of the flat plate plunging into the water tank. At 0.01162 s the pressure wave for unaerated water has reached the tank floor (see Figure 7.10 (left)). Figure 7.10 (right) shows the pressure wave reflection after reaching the tank floor. The flat plate penetration into free surface causes the water to move to the sides of the plate, see Figures 7.11 and 7.12. Figures 7.11 and 7.12 show the velocity fields before impact and after impact with the free surface. Impact creates two jets of water on both side of the plate (see Figure 7.12). The maximum pressures at the time of penetration for velocity $v = 4$ m/s, $v = 5$ m/s and $v = 7$ m/s are shown in Table 7.2.

	$v = 4$ m/s		$v = 5$ m/s		$v = 7$ m/s	
	Experimental	SPH	Experimental	SPH	Experimental	SPH
P_1	9.6817	7.35	11.4776	10.13	10.78644	14.97
P_2	11.706	12.6	22.37049	19.3	36.6996	25.6
P_3	4.17352	7.25	6.521011	10.9	14.9984	14.9

Table 7.2: Maximum gauge pressure of the plate with unaerated water.

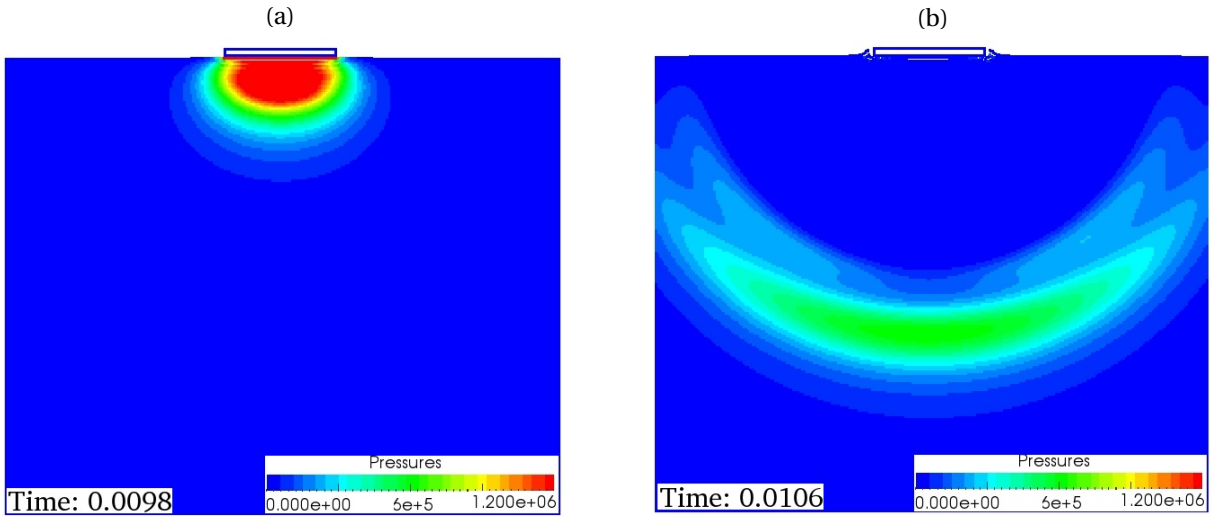

Figure 7.9: Snapshot of pressure contour of dropping flat plate into water (a) at t=0.0098 s, $v = 4$ m/s and unaerated water (b) unaerated at t=0.0106 s after impact.

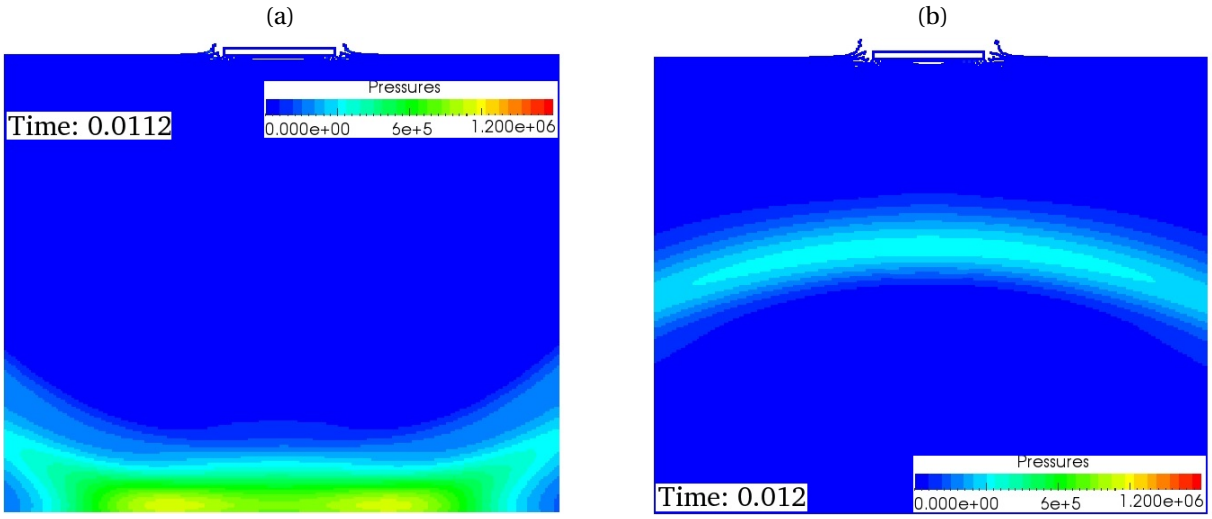

Figure 7.10: (a) Reflection of pressure wave after reaching the floor of tank at t=0.0112 s (b) Predicted water jet flows and pressure contours in water tank at t=0.0106 s.

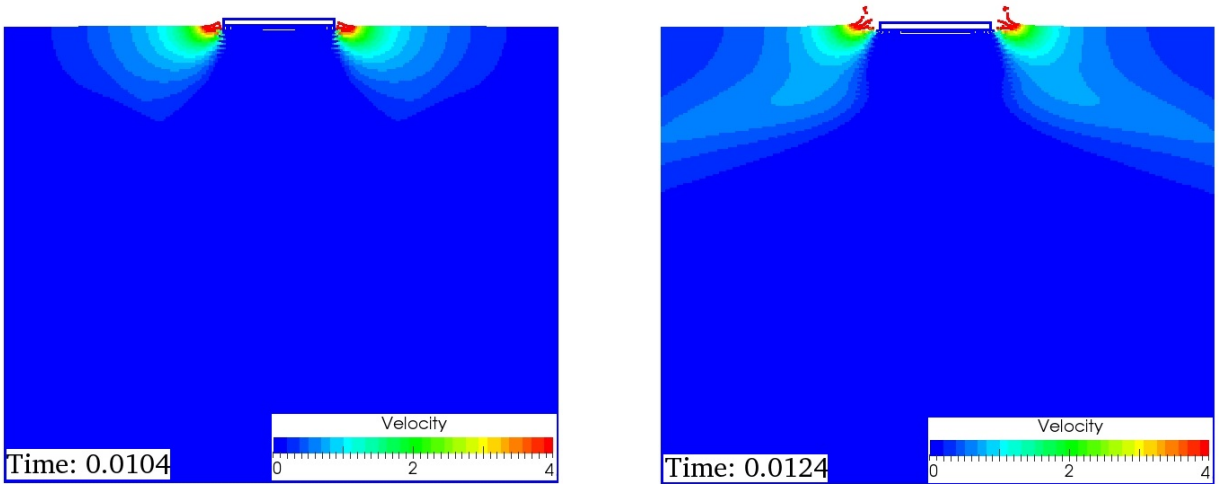

Figure 7.11: Dropping flat plate into still water tank with 0.00% aeration level and $v = 4$m/s (a) at t=0.0104 s (b) at t=0.0124 s time to impact.

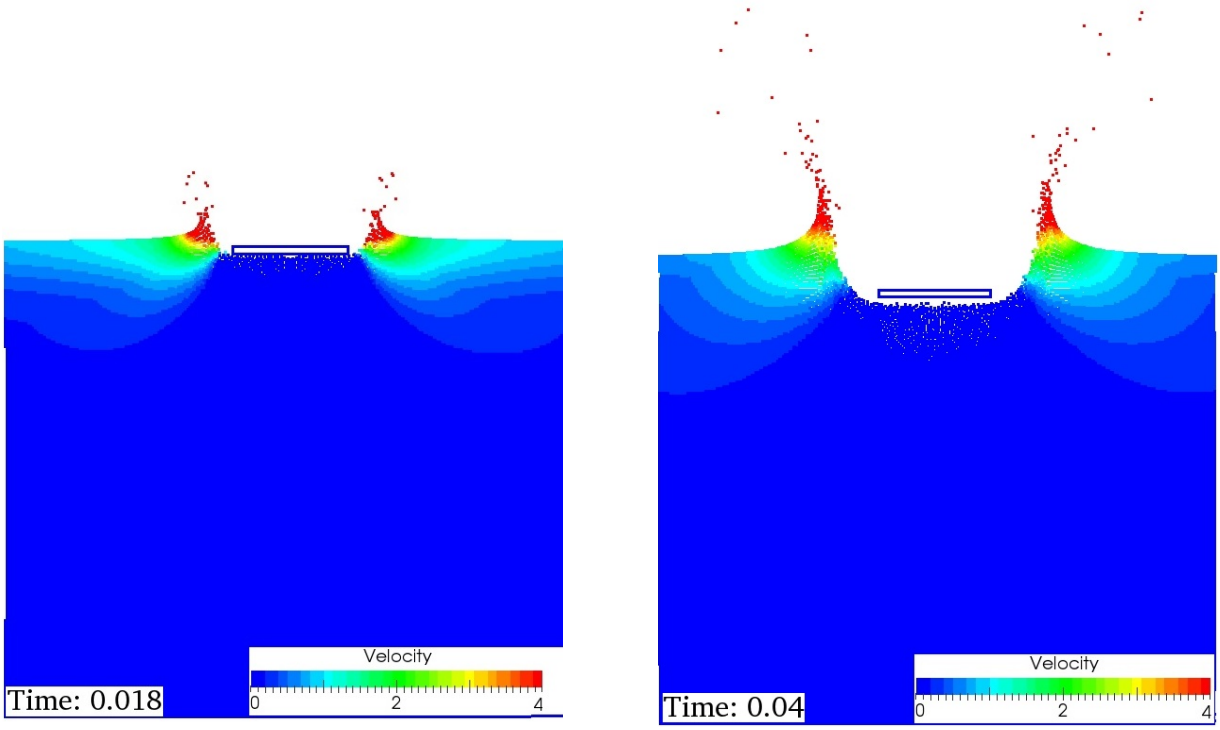

Figure 7.12: (a)Penetrate flat plate into a water tank and velocity contours at t=0.018 s (b)Predicted water jet flows and velocity contours in water tank at t=0.04 s.

7.3.2 Aerated water entry

In this section, we investigate the effects of aerated water entry on the pressure. The case shown in Figure 7.4 for pure water, is also used for the aerated water entry. The aeration levels in the water are 0.78% , 1.02% and 1.6%. We use the same number of particles as for pure water entry and measure the pressure on the bottom of the flat plate at three positions as previously. Figures 7.13 (left), 7.13 (right) and 7.14 show the comparison of time series of gauge pressure at the bottom centre of the plate for impact velocity $v = 4$ m/s, $v = 5$ m/s and $v = 7$ m/s, respectively. The SPH results for main peak values compared well with experimental results, Ma et al. (2016). However, the oscillations after impact are not captured well and the second small peak pressure is again seen after impact as a result of the reflected pressure wave.

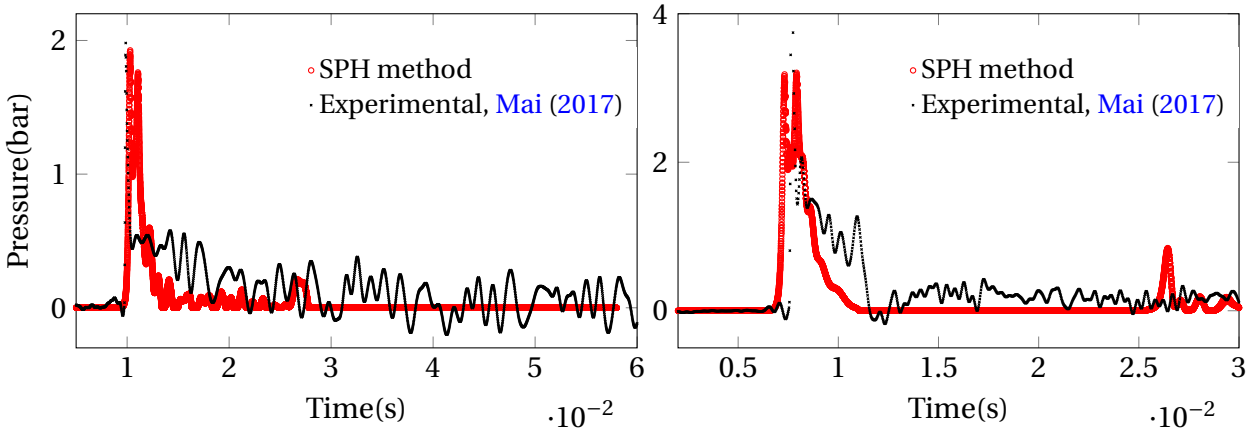

Figure 7.13: (left) Pressure distribution on the plate at p_2 with aeration level=0.78% for $v = 4$ m/s. (right) Pressure distribution on the plate at p_2 with aeration level=0.78% for $v = 5$ m/s.

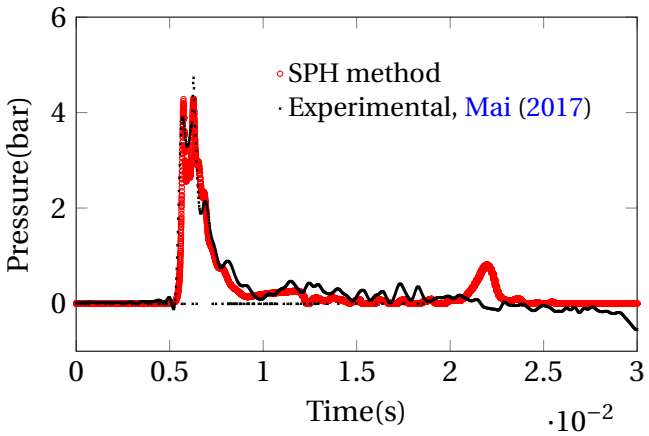

Figure 7.14: Pressure distribution on the plate at p_2 with aeration level=0.78% for $v = 7$ m/s.

Table 7.3 shows the peak pressure value within the water for 0.78% , 1.02% and 1.6% aeration levels.

	$v = 4$ m/s	$v = 5$ m/s	$v = 7$ m/s
0.00%	12.6	19.3	25.6
0.78%	1.93	3.21	4.29
1.02%	1.64	2.85	3.81
1.06%	1.23	2.32	3.08

Table 7.3: Pressure distribution on the plate at p_2 with aeration level=0.00%, 0.78%, 1.02% and 1.06% for $v = 4$ m/s, $v = 5$ m/s and $v = 7$ m/s.

Snapshots for two instances for 0.78% and 1.6% aeration levels are presented in Figures 7.15 - 7.18. The pressure wave clearly travels faster for the 0.78% aerated level than for 1.6%, due to the higher sound speed in the former. The pressure wave in 0.78% has reflected from floor the tank (see Figure 7.18 (left)) but in the 1.6% aeration level, it has just reached the floor (see Figure 7.16 (right)).

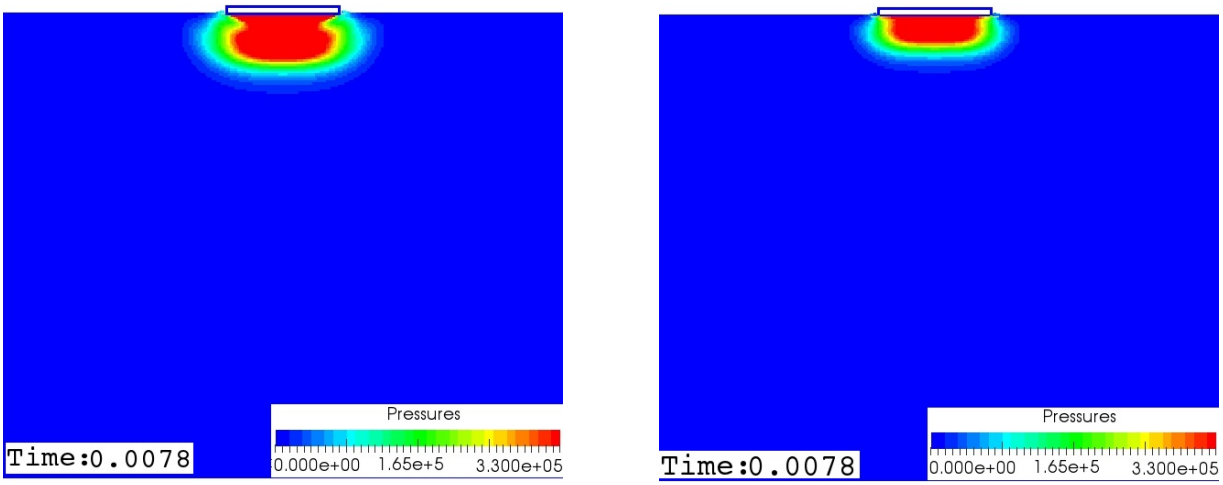

Figure 7.15: Snapshot of pressure contour of dropping flat plate into water at t=0.0078s, $v = 5$ m/s (left) aeration level is 0.78% (right) aeration level 1.6%.

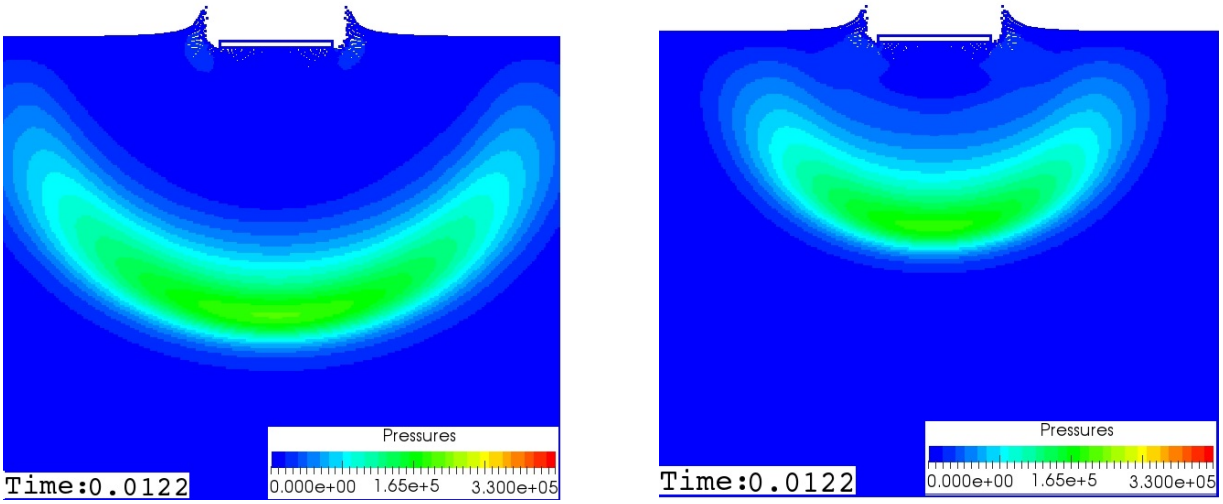

Figure 7.16: Snapshot of pressure contour of dropping flat plate into water at t=0.0122 s, $v = 5$ m/s (left) aeration level is 0.78% (right) aeration level 1.6%. after impact.

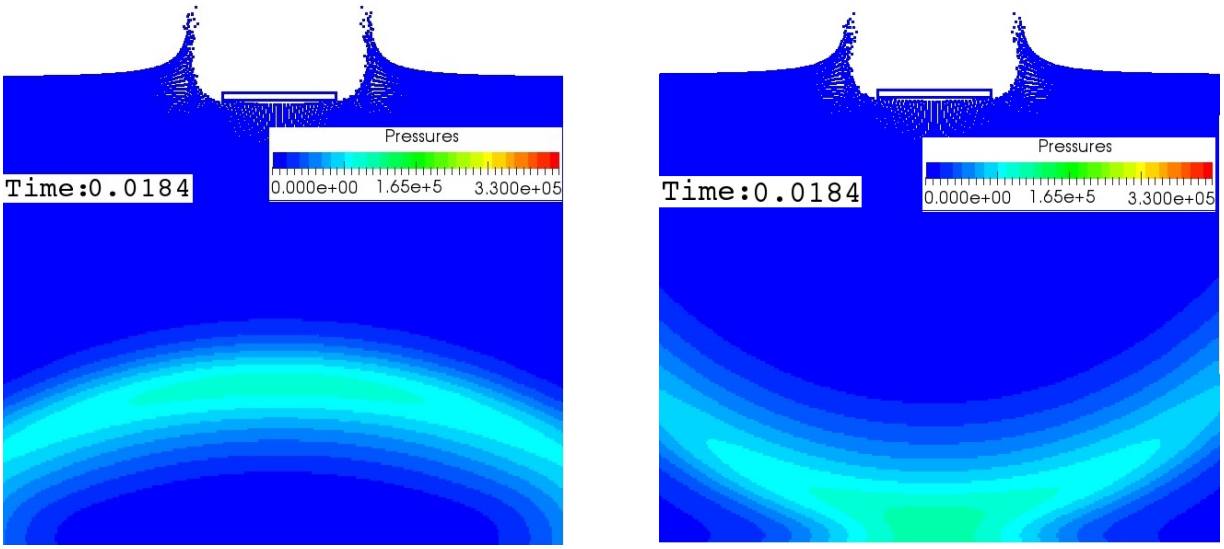

Figure 7.17: Pressure wave of dropping flat plate into water at t=0.0184 s, $v = 5$ m/s (left) aeration level is 0.78% after reflection (right) aeration level 1.6% reached the floor.

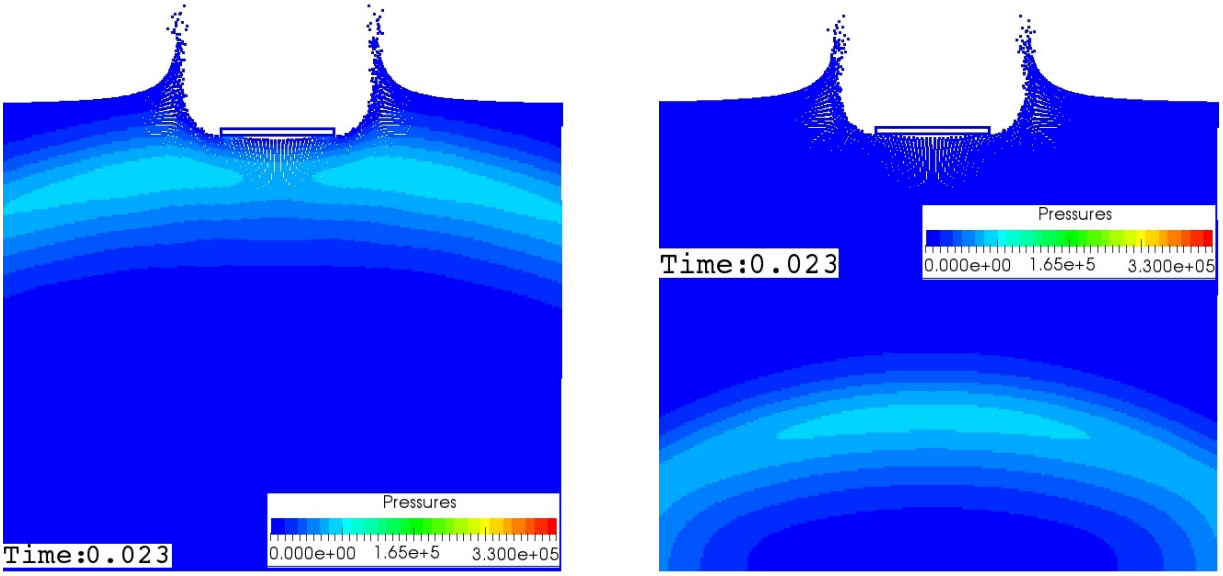

Figure 7.18: Reflection pressure wave after reached the floor of tank at t=0.023 s, $v = 5$ m/s (left) aeration level is 0.78% (right) aeration level 1.6%.

Figures 7.19, 7.20 and 7.21 show that in the experiments, the peak impact pressure on the center of the flat plate is significantly reduced by increasing the aeration level. Unlike Mai (2017) in the SPH method, the peak pressure is similarly reduced by increasing the aeration level. Table 7.4 shows the peak pressure values on the flat plate for velocities 4 m/s, 5 m/s and 7 m/s for 0.78% aeration level. The maximum value of the peak pressure at P_2 is 4.291 bar for the SPH simulation and 4.729 bar for experimental results with velocity 7 m/s. At the sides P_1 and P_3, the computed pressure at the impact are 3.11 and 3 bar but experiments show 4.6547 and 4.849 bar, respectively. We can see some difference between numerical results and experimental especially for the aerated simulations. This maybe due to the fact that the bubble maker for the experimental case makes the water surface little bit higher and is not flat when the plate impacts the surface. In our simulation we set the water surface to be flat. Tables 7.5 and 7.6 list all peak loading pressures on the plate at different locations, with velocities 4 m/s, 5 m/s and 7 m/s for experimental results and SPH simulations.

	$v = 4$ m/s		$v = 5$ m/s		$v = 7$ m/s	
	Experimental	SPH	Experimental	SPH	Experimental	SPH
P_1	1.8346	1.3	6.01698	2.28	4.6547	3.11
P_2	1.9810	1.93	6.084	3.21	4.729	4.291
P_3	1.77	1.25	6.118	2.18	4.849	3

Table 7.4: Maximum gauge pressure of the plate with aeration level=0.78%

	$v = 4$ m/s		$v = 5$ m/s		$v = 7$ m/s	
	Experimental	SPH	Experimental	SPH	Experimental	SPH
P_1	1.62	1.11	3.49515	2.01	2.8396	2.78
P_2	0.778	1.64	3.0418	2.85	2.7138	3.81
P_3	1.0777	1.07	1.7803	1.94	2.3521	2.67

Table 7.5: Maximum gauge pressure of the plate with aeration level=1.02%

	$v = 4$ m/s		$v = 5$ m/s		$v = 7$ m/s	
	Experimental	SPH	Experimental	SPH	Experimental	SPH
P_1	0.9388	0.852	–	1.63	1.1218	2.25
P_2	1.8517	1.23	–	2.32	2.6332	3.08
P_3	1.441	0.816	–	1.57	3.9371	2.18

Table 7.6: Maximum gauge pressure of the plate with aeration level=1.6%

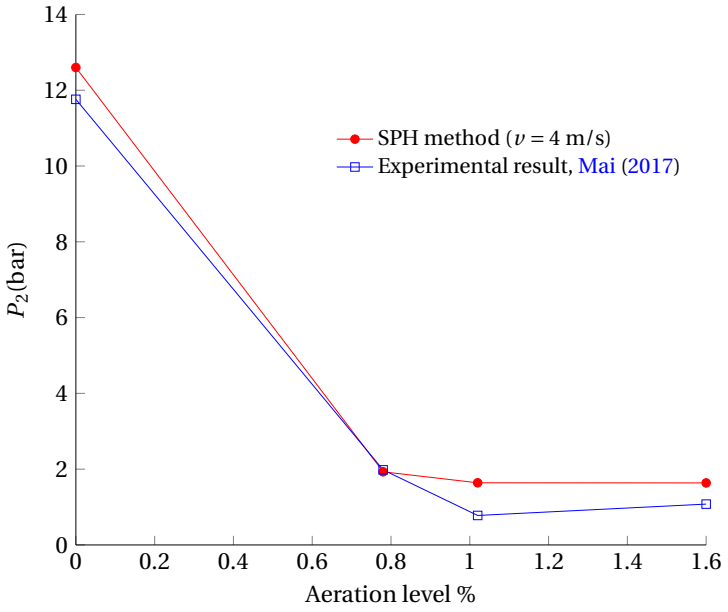

Figure 7.19: The peak impact gauge pressure affected by aeration at $v = 4$ m/s

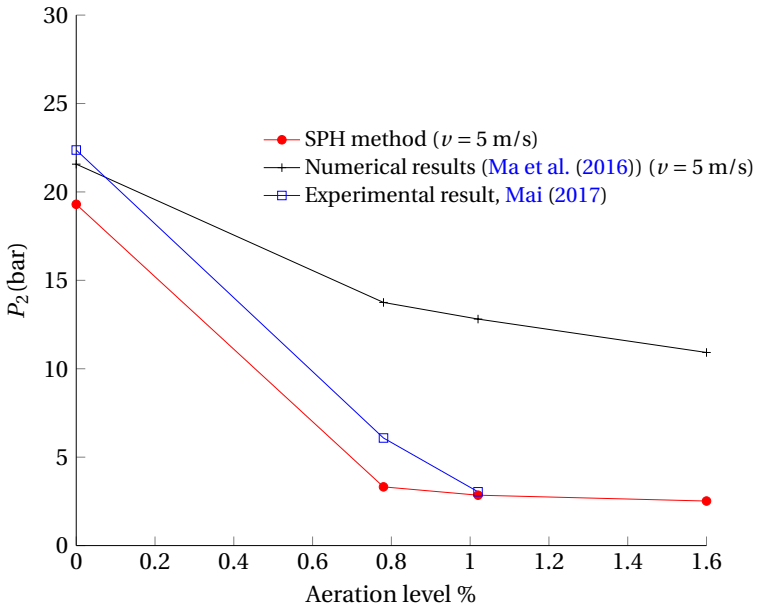

Figure 7.20: The peak impact gauge pressure affected by aeration at $v = 5$ m/s

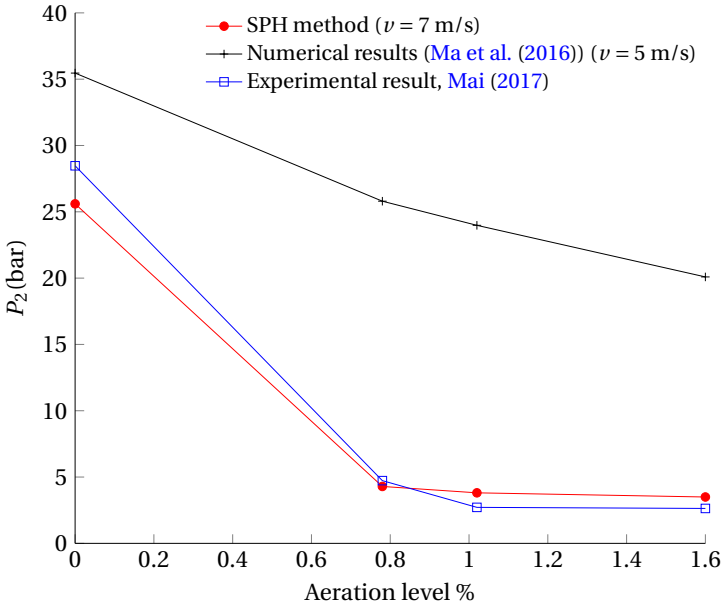

Figure 7.21: The peak impact gauge pressure affected by aeration at $v = 7$ m/s

7.3.3 Convergence in SPH Single phase method

In this section, we study the convergence of SPH and to show that how the difference resolutions affect the peak pressure at the centre of the plate. Four different particle numbers, 135000, 240000 , 540000 and 843750, are used for a resolutions investigation. Figures 7.22, 7.23 and 7.24 compare the SPH peak pressure at the middle of the plate for these four resolutions for velocity 4, 5 and 7, respectively. It shows that the peak pressure is not strictly converged and also is very sensitive to the number of particles.

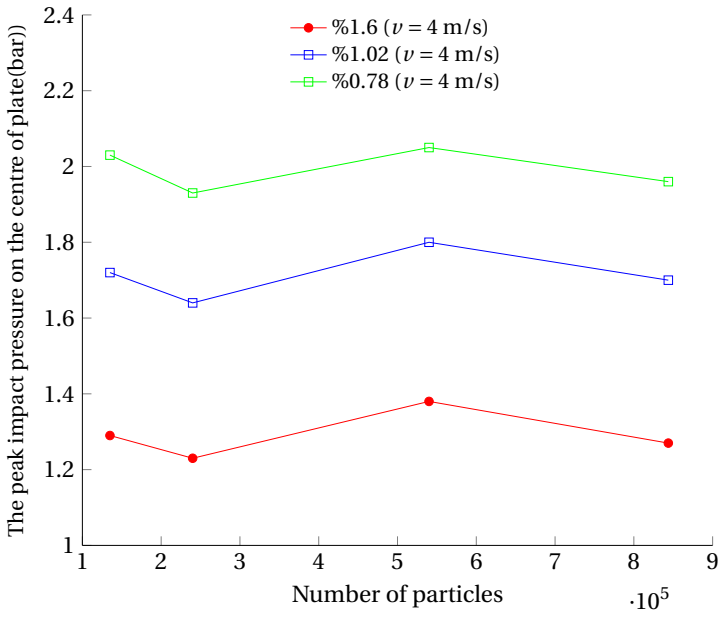

Figure 7.22: The peak impact gauge pressure affected by different resolutions for $v = 4$ m/s .

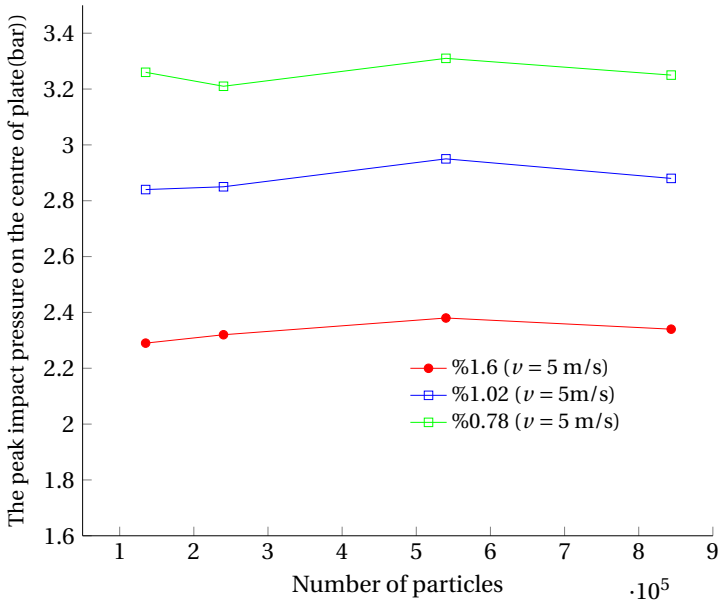

Figure 7.23: The peak impact gauge pressure affected by different resolutions for $v = 5$ m/s.

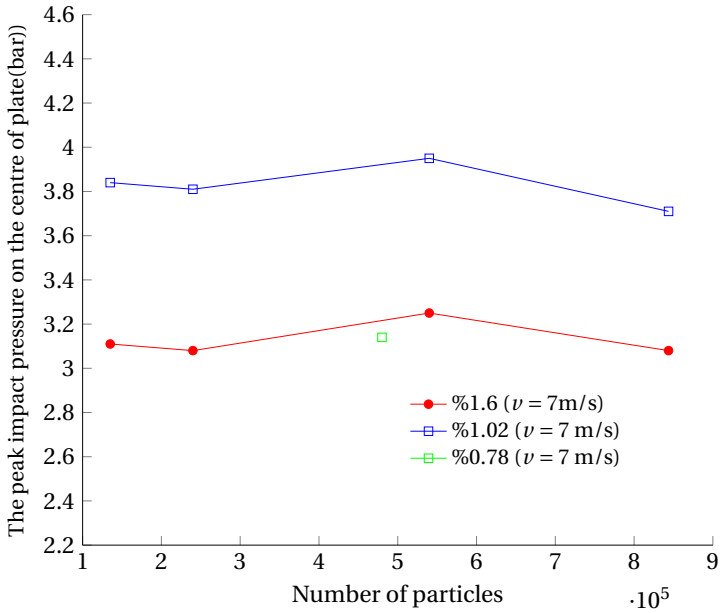

Figure 7.24: The peak impact gauge pressure affected by different resolutions for $v = 7$ m/s.

7.4 Conclusion

First, we used the SPH method to simulate a flat plate impacting onto a water surface with different water aeration levels. The SPH method successfully predicts the reduction in the impact loading on the flat plate during the water entry due to increased aeration. Four different resolutions have been investigated to show how the number of particles affects the peak pressure at the centre of the plate. The results showed that the pressure peak was not very sensitive to the number of particles. The numerical and experimental results show that for impact velocity $v = 7$ m/s the pressure peak on the plate will be reduced from 25.6 bar in pure water to 3.08 bar in 1.6% aerated water, from 19.3 bar in pure water to 2.32 bar in 1.6% and from 12.6 bar in fresh water to 1.23 bar in 1.6% for $v = 7$ m/s, $v = 5$ m/s and $v = 4$ m/s, respectively. In the next section, we simulate 2D multi-phase simulations of a flat plate impacting on aerated water to find out the rule of air phase on the free surface and plate.

7.5 2D Multi-phase

In this section, a multi-phase water and air model of the flat plate drop will be investigated. In this case, air is entrapped by the flat plate. The dimension of the tank and the plate will be the same as for the single phase cases. The main difference in multi-phase is that we track the influence of the air phase over the plate and free surface. The number of particles used in these simulations is 480000.

After the start of the simulation, the plate moves down where, at about 0.008s after starting of simulation, the plate impacts with the free surface, reducing the velocity of the plate. The air plays an important role to determine the pressure at impact. The values of speed of sound for aerated water are the same a single phase simulations (see Figure 7.1), while the speed of sound for the air phase can be found by:

$$\frac{C_a^2 \rho_a}{\gamma_a} = \frac{C_w^2 \rho_w}{\gamma_w} \tag{7.3}$$

where C_a, ρ_a and γ_a are for the air phase and C_w, ρ_w and γ_w are for the water phase. Figure 7.25 shows the initial water, air and plate at t=0.

7.5.1 Influence of background pressure

The results presented in sections 5.5.1 and 5.5.2 showed the benefits of using background pressure to remove the formation of voids in the air phase. Here, the voids appeared around the flat plate in air phase. From comparing Figures 7.26, 7.27 and 7.28, it is clear that, as expected, the

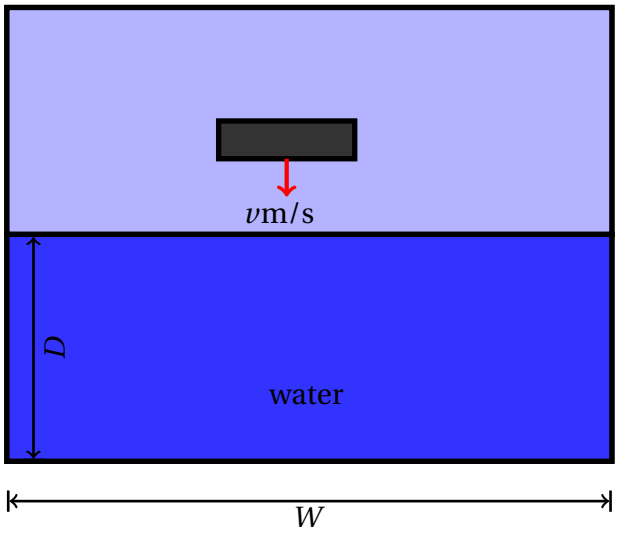

Figure 7.25: Set up the model of impact of a flat plate

voids will disappear when the background pressure is used. $\chi = 0.01$ is the value of background used in these simulations (see equation 3.23). As shown in Figures 7.26, 7.27 and 7.28, the background pressure does not affect the overall water movement, in general.

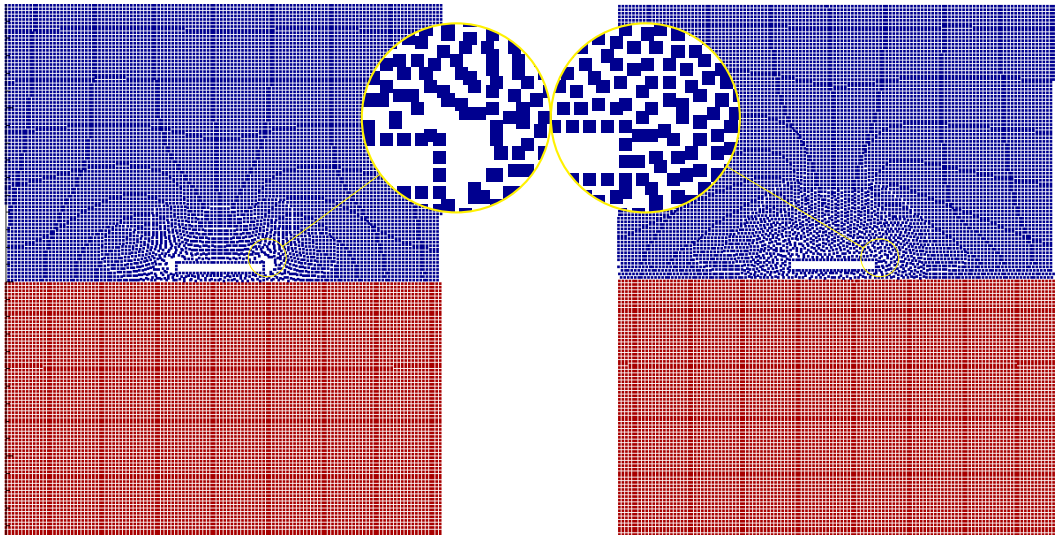

Figure 7.26: Drop plate at t=0.005 s without using background pressure (left) and with background pressure (right)

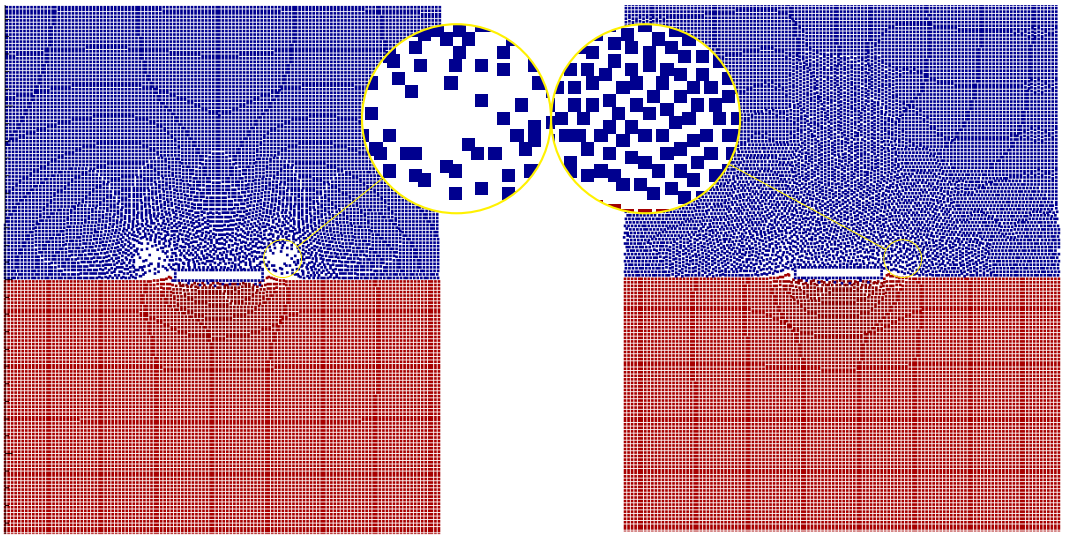

Figure 7.27: Drop plate at t=0.0086 s without using background pressure (left) and with background pressure (right)

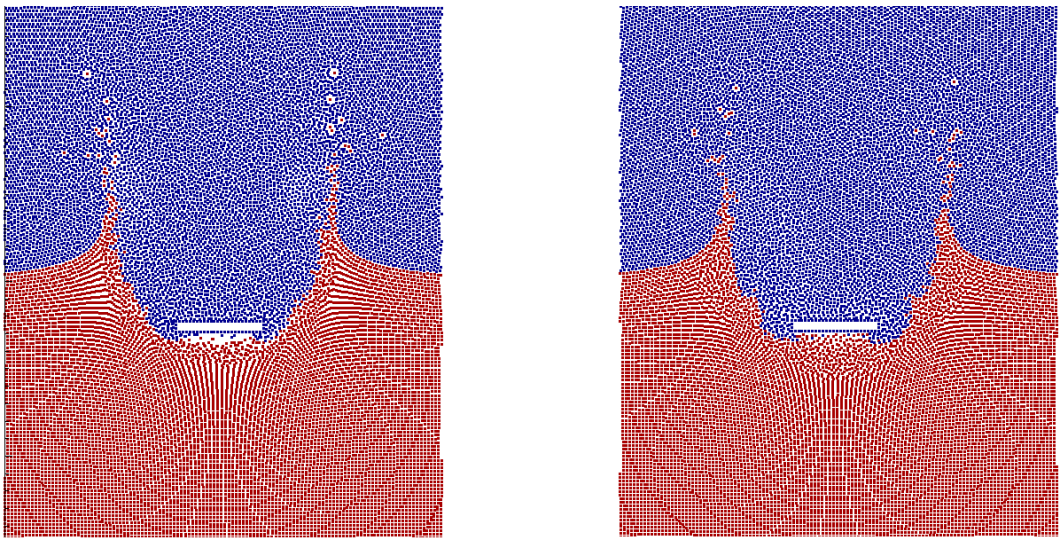

Figure 7.28: Drop plate at t=0.0572s without using background pressure (left) and with background pressure (right)

7.5.2 Aerated water entry

In this section, the effects of the air phase on the peak pressure and free surface for different levels of aeration will be investigated. To measure the pressure on the plate, the SPH sum is used as in previous sections. The influence of the air phase on the free surface is shown in Figure 7.29 (right) and compared with single phase simulation, see Figure 7.29 (left). It shows the flat plate is still far from the water surface, but clearly influences the free surface pressure wave, whereas for the single phase it takes about 0.008 s to start the wave pressure. Figure 7.30 and 7.31 indicate a sequence of snapshots for single and multi-phase simulations and show the particle distribution at the time of impact and after impact, respectively (in each figure the top one is single phase and bottom is multi-phase). In the single phase case, the plate affects the free surfaces particles at the time of impact and there is no sign of deformation on the water surface (see Figure 7.30 (top)), but in the multi-phase case, the water surface particles caused by air particles just before impact and a small wave in the water surface are shown (see Figure 7.31 (bottom)). Figures 7.32, 7.33 and 7.34 show a sequence of snapshots for two different velocities (5 m/s and 7 m/s) of the same aeration level when the flat plate plunges into the water. Some air particles will be trapped beneath the flat plate, unable to escape and caused lack of symmetry. This produces an irreversible air-water mixture that is effective at cushioning the impact

and the pressure wave, Lind et al. (2015*b*).

Time series of pressure at the center of the plate for the impact velocities $v = 4$ m/s, $v = 5$ m/s and $v = 7$ m/s are plotted in Figures 7.35 , 7.36, 7.37 ,7.38 and 7.39, respectively. The results are compared with single phase and FROTH experiments and give generally good agreement compared to the single phase simulations, but the pressure of some air particles being trapped beneath the flat plate, causes a loss in the symmetry of the wave pressure (see Figures 7.32, 7.33 and 7.34).

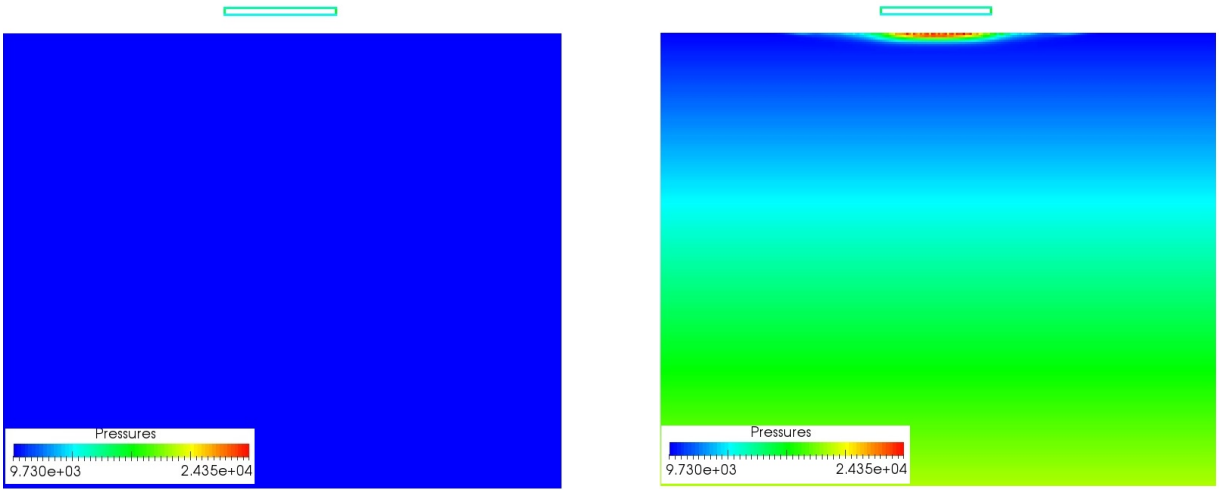

Figure 7.29: Snapshot of pressure contour of dropping flat plate into water at the start of simulation, $v = 5$ m/s and aeration level is 1.6% (left) Single phase (right) Multi-phase.

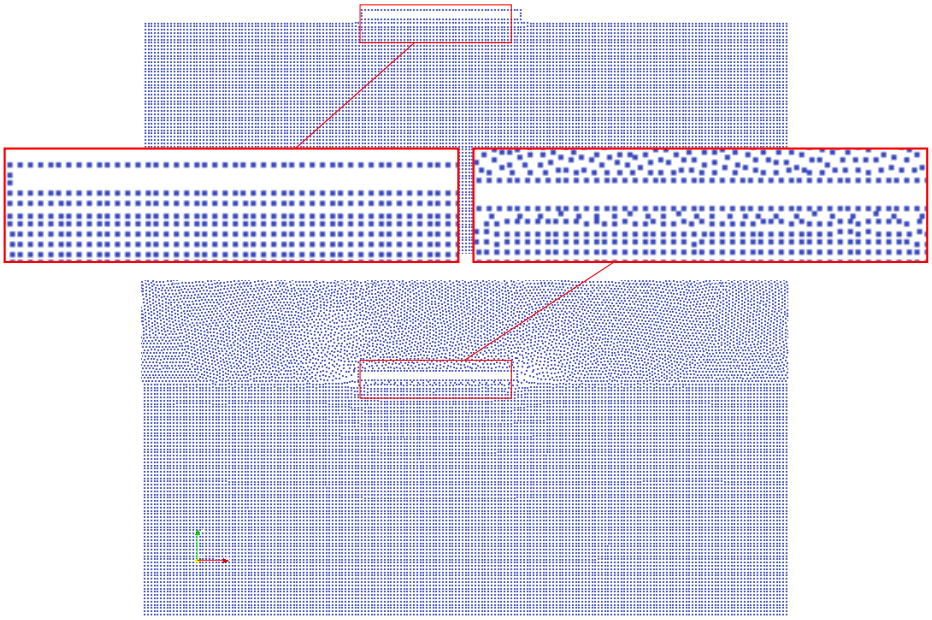

Figure 7.30: Compare particle distribution between single phase simulation (top) and multi-phase simulation (bottom)

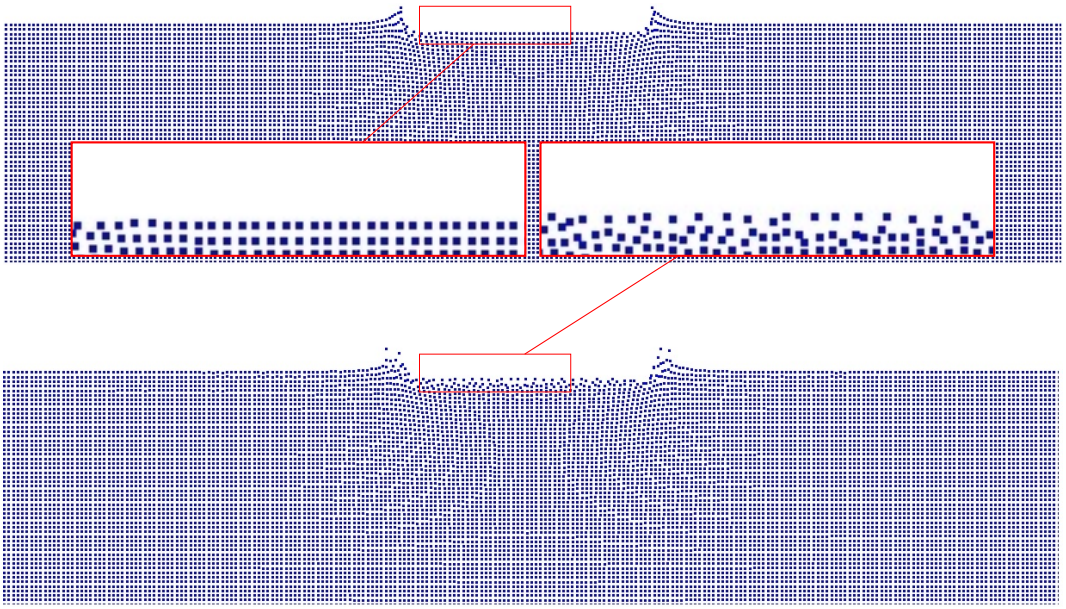

Figure 7.31: Compare particle distribution between single phase simulation (top) and multi-phase simulation (bottom)

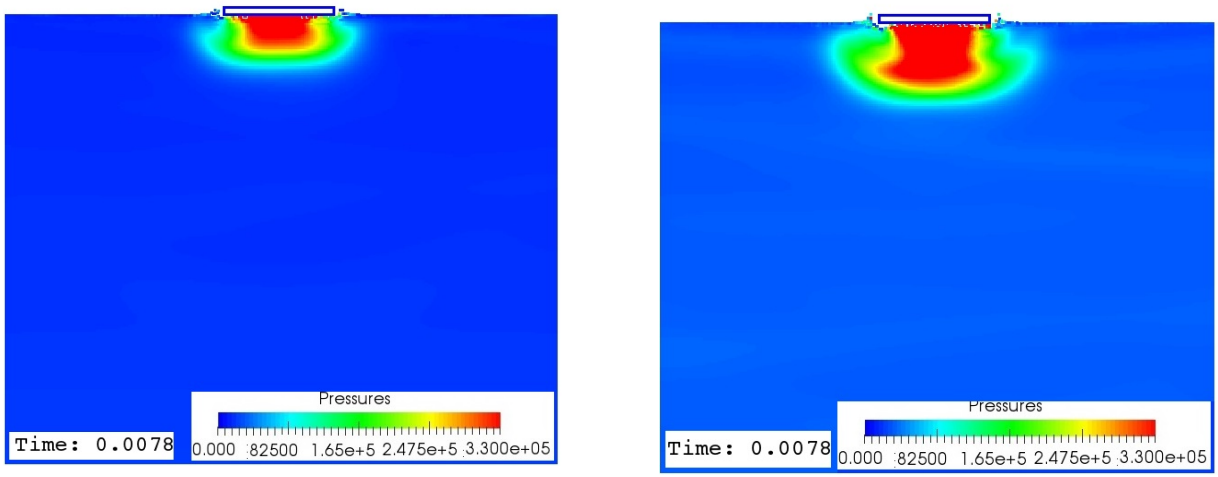

Figure 7.32: Snapshot of pressure contour of dropping flat plate into water at t=0.0078 s, v = 5 m/s (left) aeration level is 0.78% (right) aeration level 1.6%.

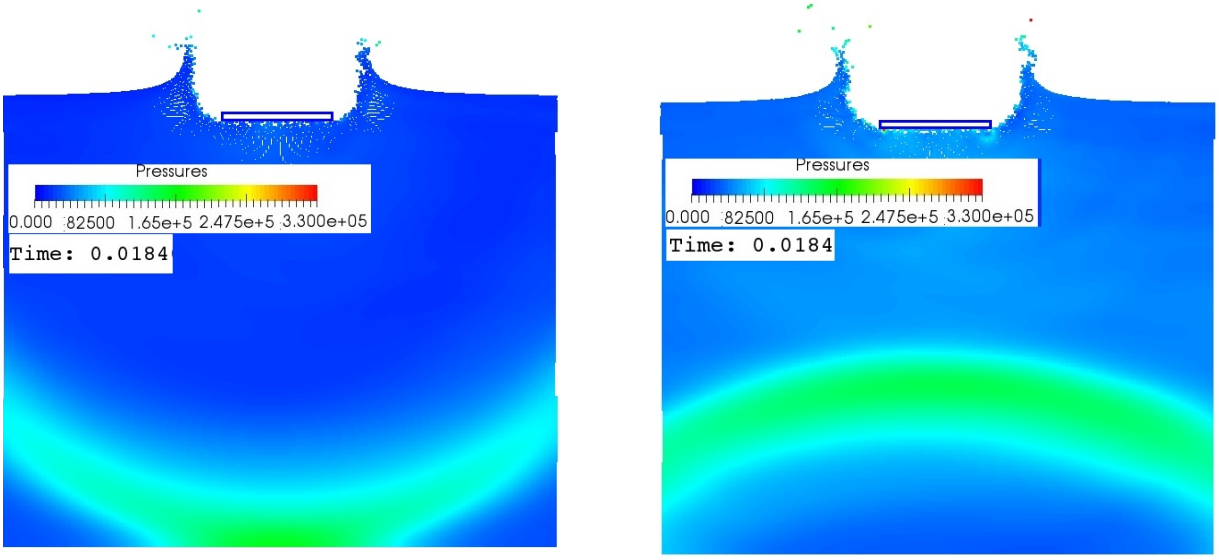

Figure 7.33: Snapshot of pressure contour of dropping flat plate into water at t=0.0184 s, v = 5 m/s (left) aeration level is 0.78% (right) aeration level 1.6%.

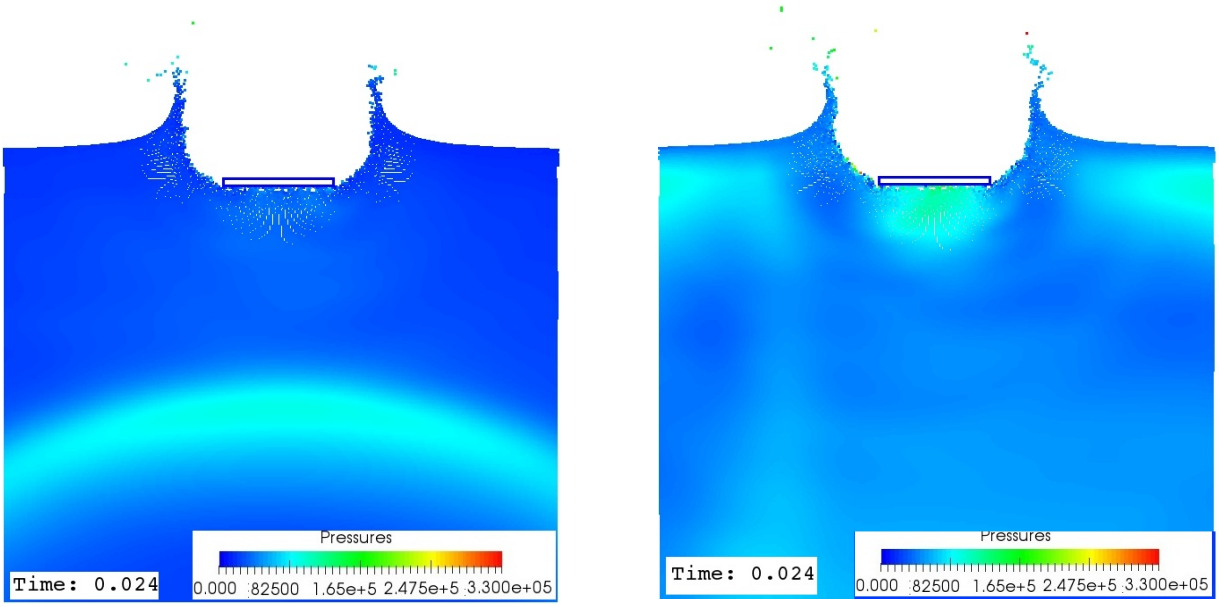

Figure 7.34: Snapshot of pressure contour of dropping flat plate into water at t=0.024 s, $v = 5$ m/s (left) aeration level is 0.78% (right) aeration level 1.6%.

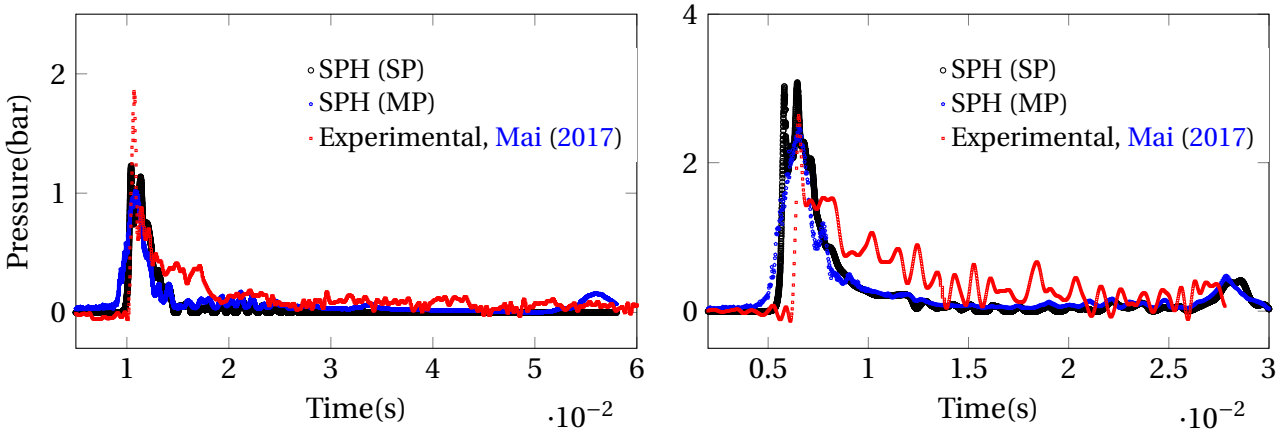

Figure 7.35: (left) Pressure distribution on the plate at p_2 with aeration level=1.6% for $v = 4$ m/s. (right)Pressure distribution on the plate at p_2 with aeration level=1.6% for $v = 7$ m/s.

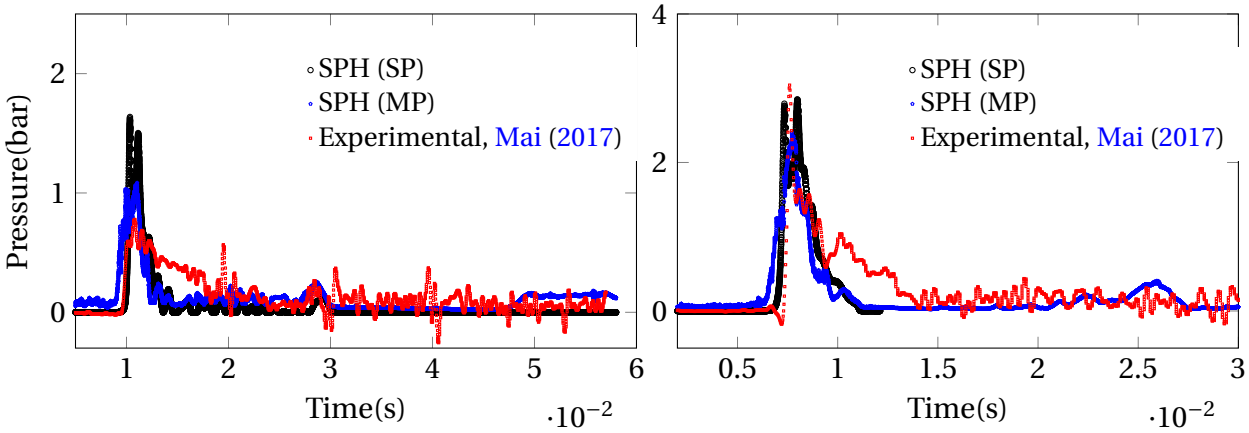

Figure 7.36: (left) Pressure distribution on the plate at p_2 with aeration level=1.02% for $v = 4$ m/s. (right)Pressure distribution on the plate at p_2 with aeration level=1.02% for $v = 5$ m/s.

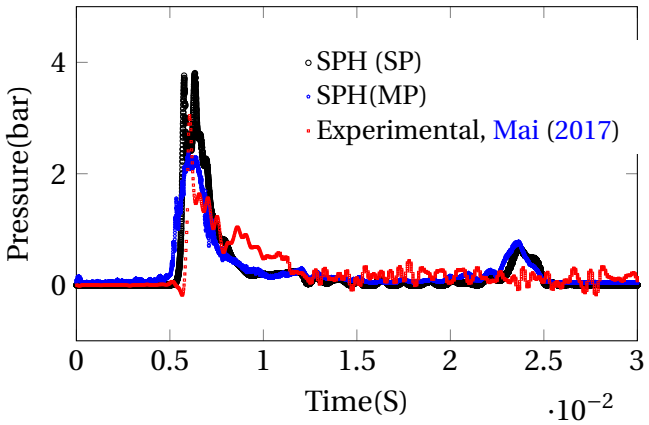

Figure 7.37: Pressure distribution on the plate at p_2 with aeration level=0.78% for $v = 7$ m/s.

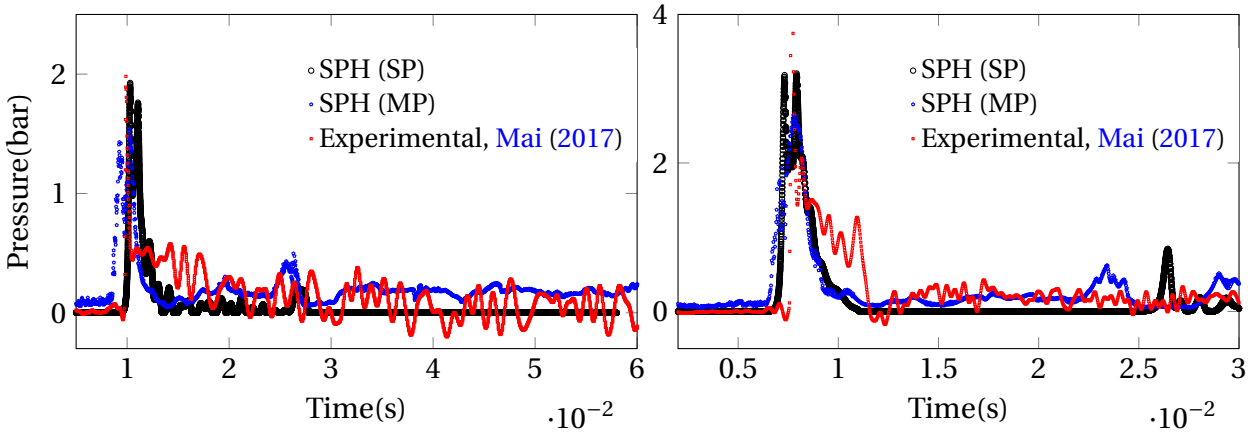

Figure 7.38: (left) Pressure distribution on the plate at p_2 with aeration level=0.78% for $v = 4$ m/s. (right)Pressure distribution on the plate at p_2 with aeration level=0.78% for $v = 5$ m/s.

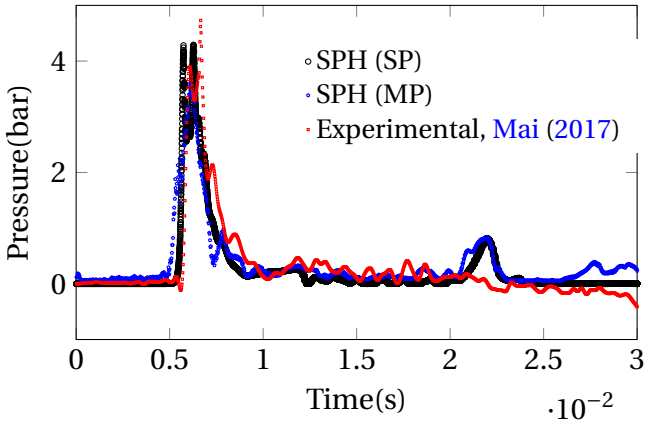

Figure 7.39: Pressure distribution on the plate at p_2 with aeration level=0.78% for $v = 7$ m/s.

The peak pressure values with the plate plunging into the water are presented in Tables 7.7, 7.8 and 7.9. Tables 7.7, 7.8 and 7.9 show the peak pressure values computed at the three different positions (center, left and right corner) at the time of impact for 0.78%, 1.02% and 1.6% aeration levels. The overall trends are captured reasonably well. As expected, the peak pressure in the computations are found at the middle measuring point P2. Furthermore, the computed pressure at P1 and P3 are close to each other, as expected from symmetry considerations. Peak pressure decrease sharply with increased aeration. Given the known difficulties in predicting impact pressure, the peak values compare surprisingly well with experimental values except for v=5 m/s at 0.78 % aeration, where the experimental values appear anomalously high (as pressures for this case exceed the pressure for $v = 7$ m/s at the same aeration level).

Tables 7.10, 7.11 and 7.12 show a comparison between experimental, SPH single phase and SPH multi-phase values of the pressure impulse

	$v = 4$ m/s			$v = 5$ m/s			$v = 7$ m/s		
	Exp.	SPH(SP)	SPH(MP)	Exp.	SPH(SP)	SPH(MP)	Exp.	SPH(SP)	SPH(MP)
P_1	1.8346	1.3	1.53	6.01698	2.28	1.38	4.6547	3.11	2.27
P_2	1.9810	1.93	1.48	6.084	3.21	2.35	4.729	4.291	3.43
P_3	1.77	1.25	1.2	6.118	2.18	1.61	4.849	3	1.98

Table 7.7: Maximum gauge pressure of the plate with aeration level=0.78% for experimental data, single phase and multi-phase at the time of impact.

	$v = 4$ m/s			$v = 5$ m/s			$v = 7$ m/s		
	Exp.	SPH(SP)	SPH(MP)	Exp.	SPH(SP)	SPH(MP)	Exp.	SPH(SP)	SPH(MP)
P_1	1.62	1.11	0.784	3.49515	2.01	1.77	2.8396	2.78	1.84
P_2	0.778	1.64	1.09	3.0418	2.85	2.4	2.7138	3.81	2.77
P_3	1.0777	1.07	0.87	1.7803	1.94	1.6	2.3521	2.67	1.75

Table 7.8: Maximum gauge pressure of the plate with aeration level=1.02% for experimental data, single phase and multi-phase at the time of impact.

	$v = 4$ m/s			$v = 5$ m/s			$v = 7$ m/s		
	Exp.	SPH(SP)	SPH(MP)	Exp.	SPH(SP)	SPH(MP)	Exp.	SPH(SP)	SPH(MP)
P_1	0.9388	0.852	0.593	-	1.63	0.95	1.1218	2.25	1.6
P_2	1.8517	1.23	1.02	-	2.32	1.68	2.6332	3.08	2.31
P_3	1.441	0.816	0.748	-	1.57	1.03	3.9371	2.18	1.24

Table 7.9: Maximum gauge pressure of the plate with aeration level=1.6% for experimental data, single phase and multi-phase at the time of impact.

evaluated at the centre of the plate for aerated water impact at $v = 5$ m/s and $v = 7$ m/s for 1.6%, 1.02% and 0.78%, respectively.

	$v = 5$ m/s			$v = 7$ m/s		
	Experiment	SPH(SP)	SPH(MP)	Experiment	SPH(SP)	SPH(MP)
P_2	–	756.55	574.69	884.2325	1027.17	790.16

Table 7.10: Pressure impulses aeration level 1.6%.

7.5.3 Plate impact on Fresh water

To simulate the flat plate entry on fresh water (0% aeration), the cushioning due to the air phase is considered. The dimensions of the plate and water tank are the same as the single phase case. The plate drops with three different velocities, $v = 4$ m/s, $v = 5$ m/s and $v = 7$ m/s. The impact

	$v = 5$ m/s			$v = 7$ m/s		
	Experiment	SPH(SP)	SPH(MP)	Experiment	SPH(SP)	SPH(MP)
P_2	584.5146	698.102	579.57	940.4118	1002.31	861.4

Table 7.11: Pressure impulses aeration level 1.02%.

	$v = 5$ m/s			$v = 7$ m/s		
	Experiment	SPH(SP)	SPH(MP)	Experiment	SPH(SP)	SPH(MP)
P_2	667.2559	665.915	545.72	834.6258	951.167	795.6132

Table 7.12: Pressure impulses aeration level 0.78%.

pressure at the center of plate is of interest and will be compared to the single phase, experimental and numerical results, Ma et al. (2016). The time history of the pressure at the center of the plate is plotted in Figures 7.40 and 7.41. As can be seen in the plot, the peak pressure in the SPH multi-phase simulation can not reach the single phase, experimental and numerical results due to the fact sound speed used here is limited. The results presented in sections 7.3.1, 7.3.2 and 7.5.2 show the peak pressure is affected by the speed of sound. For the results shown in section 7.3.1, the maximum speed sound of 700 was used for pure water. Here, in the multi-phase simulation a different value of speed sound is required. However, we would not be able to use the actual single phase sound speed since this would be very high, see equations 7.1 and 7.3. The reduction in sound speed will reduce the peak pressure and, consequently, the peak pressure is underpredicted.

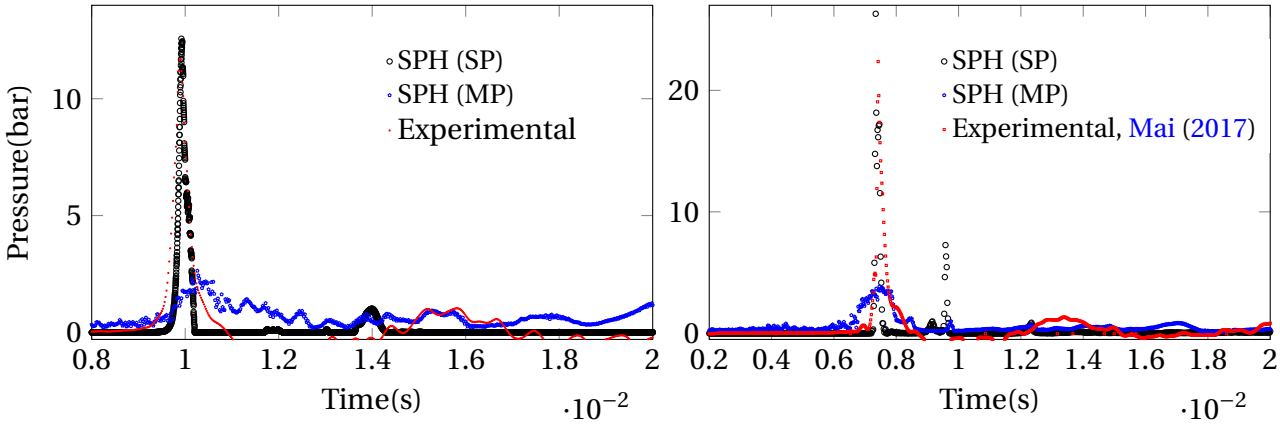

Figure 7.40: (left) Pressure distribution on the plate at p_2 with aeration level=0.00% for $v = 4$ m/s. (right) and for $v = 5$ m/s.

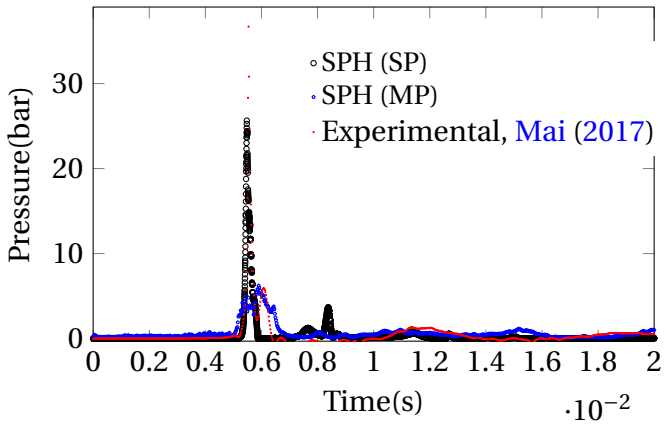

Figure 7.41: Pressure distribution on the plate at p_2 with aeration level=0.00% for $v = 7$ m/s.

7.5.4 Comparisons with Finite Volume Method (Ma et al. (2016))

In this section, our results will be compared with the numerical results of Ma et al. (2016)). Figures 7.42 and 7.43 show the SPH predictions of peak pressure are in good agreement with experiment results, whilst the prediction of maximum pressure in the finite volume method was higher the experiment data. For example: The maximum peak pressure in SPH for aeration level 1.6 is 2.447 bar but in the finite volume method is 20.09 bar, nearly 8 times higher than the measured value of maximum pressure. In multi-phase SPH simulations for fresh water, we face the same issue, where the peak pressure value at the center of the plate will be lower than the measured value, see section 7.5.3. Figures 7.44 and 7.45 show the comparison between experimental, finite volume method and SPH values of the pressure impulse evaluated at the center of the plate for the aerated water impact at $v = 5$ m/s and $v = 7$ m/s.

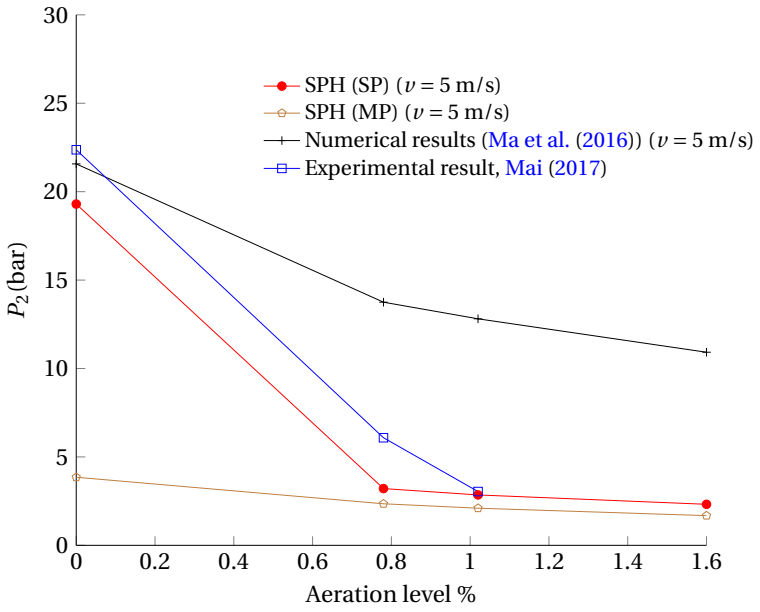

Figure 7.42: The peak impact gauge pressure affected by aeration at $v = 5$ m/s

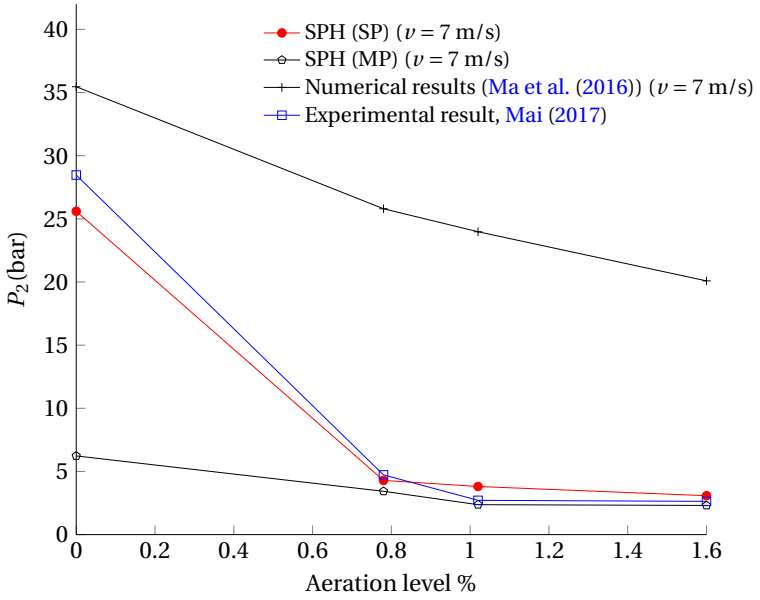

Figure 7.43: The peak impact gauge pressure affected by aeration at $v = 7$ m/s

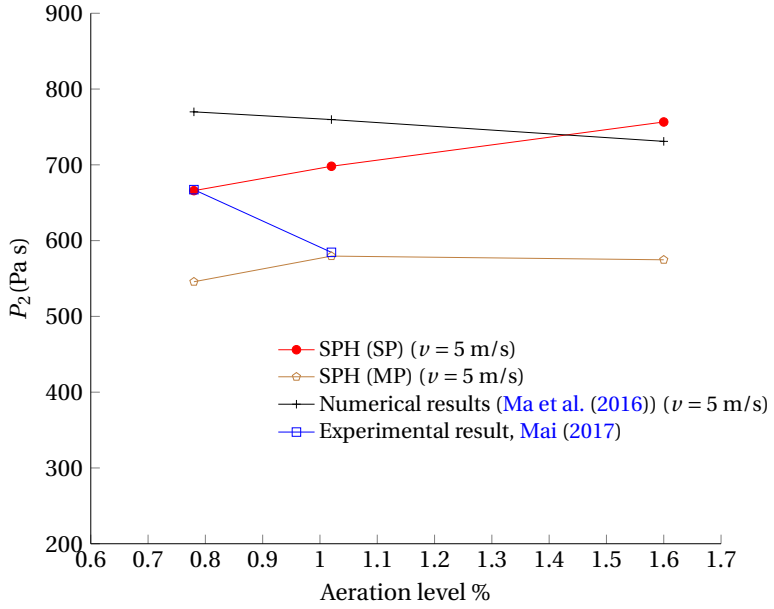

Figure 7.44: The impulse of shock loading affected by aeration at $v = 5$ m/s

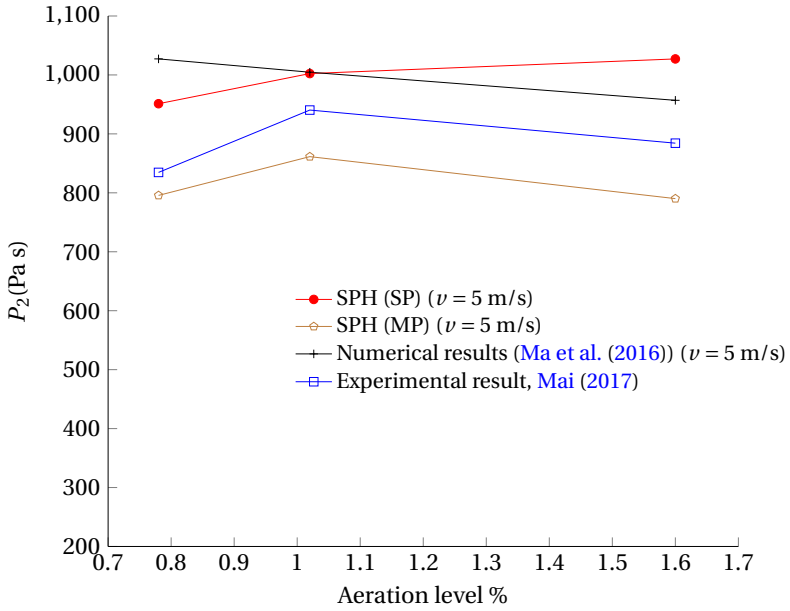

Figure 7.45: The impulse of shock loading affected by aeration at $v = 7$ m/s

7.5.5 Convergence in SPH multiphase method

Here, we move forward to find out about the effect of particle resolution on the peak pressure for multi-phase cases. We varied the number of

particles for two different velocities. Figure 7.46 compares the peak pressure results for three different numbers of particles: 480000, 1080000 and 1687500. It shows that the peak pressure is staidly increased with higher resolution in contrast to the single phase simulation in which the peak pressure in some cases decreased. The reason for this is that the number of air particles which are trapped beneath the flat plate and unable to escape, will be increased. Results, however are not exactly sensitive to particle spacing and are thus sufficiently well converged.

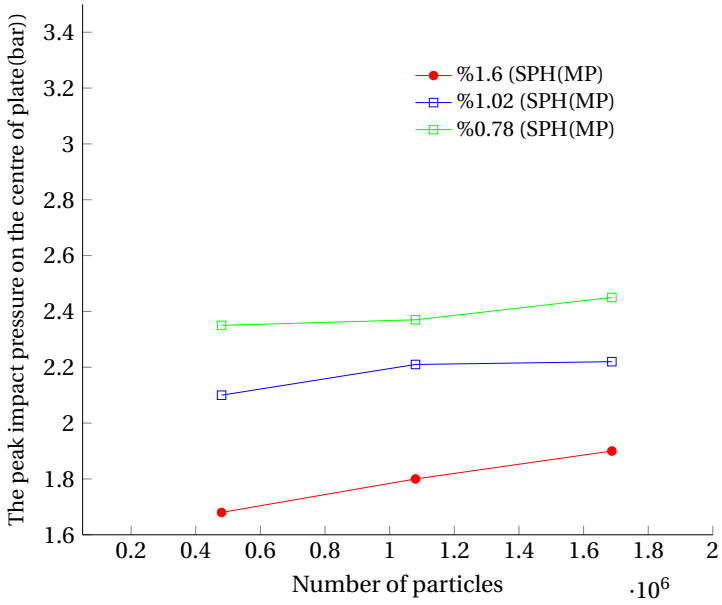

Figure 7.46: The peak impact gauge pressure affected by different resolutions for $v = 5$ m/s.

7.6 Conclusion

In this section, a 2D multi-phase SPH method has been used to simulate a flat plate impacting with with a water surface with different water aeration levels. The multi-phase SPH method is compared with single phase SPH, experimental (Mai (2017)) and finite volume results (Ma et al. (2016)) and the results show the impact loading on the flat plate during the water entry is fairly well predicted. The results showed the number of particles did not affect the peak pressure significantly. The SPH method and experimental results show the pressure peak on the plate will be slightly reduced compared to the single phase case due to the cushioning effect of the air particles over the plate. In the next chapter, we work to produce 3D single-phase simulations of a flat plate impacting on aerated water. We note that main difference between single and multi-phase results was that the predicted pressure begin to increases just before plate impact due to compression of the air cushion below the plate. Peak impact pressure did not show significant differences.

CHAPTER 8

3D FLAT PLATE DROPPING

In this chapter, obtaining realistic results for flat plate dropping and the validation of the single phase model will be extended to 3D. The flat plate dropping computational set up is similar to the two-dimensional cases with reduction of fluid domain to 1.6 m length, 1.6 m width and 1m depth. The depth of the fluid is 1m as for the experimental case, Mai et al. (2014). Figure 8.1 illustrates a snapshot of the experiment (Mai et al. (2014)) and schematics of 3D flat plate simulations. In both experimental and numerical setups the plate is above the water surface before dropping into water. A 0.25 m $\times$0.25m$\times$0.0125 m plate hits the stationary water surface with different aerated levels between 0.0%$-$1.6% at three different velocities v = 4 m/s, 5 m/s and 7 m/s. Fluid particles are distributed uniformly with spacing size $\Delta x = \Delta y = \Delta z = 0.00833$ where $\Delta x, \Delta y$ and Δz are the initial particle distances. The number of particles in x, y and z-

direction are 192, 192 and 120 particles, respectively, and the total number of particle used in this simulation is 4430000. Pressure is measured during the simulation at 5 points ($P_1 - P_5$) using an SPH sum and these measuring pressure positions in 3D are shown in Figure 8.2. The results are compared with experimental (Mai et al. (2014)) and 2D results include the pressure at the center and another four points at the side of the plate.

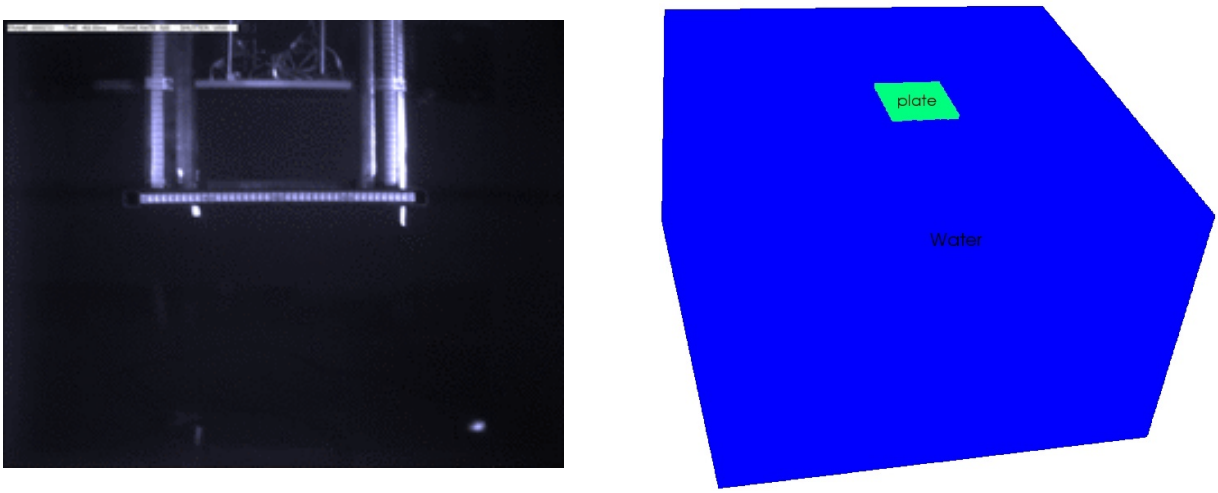

Figure 8.1: Snapshot of dropping flat plate into water at t=0.0s for $v = 4m/s$ and unaerated water : Experimental (left) SPH simulation (right).

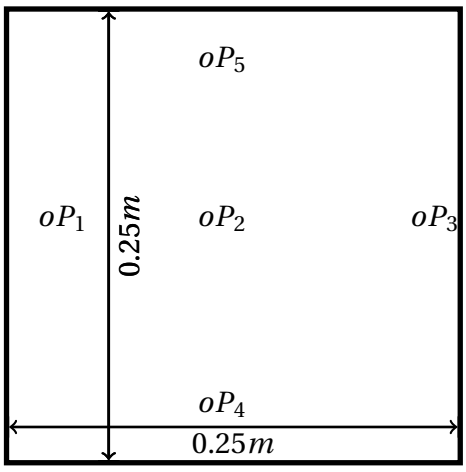

Figure 8.2: Measuring position of pressure in 3D of a flat plate

When the plate falls under the initial velocity and reaches the water

surface, the water particles move upwards as a result of the plate penetrating onto the water and forces exerted by the plate. After about 0.01s from impact, the plate impacts the stationary water and the water reduces the velocity of the plate; then loading pressure on the plate will be decreased. Figure 8.3 shows loading pressure on the plate for $v = 4m/s$ and unaerated water at the impact. It shows the loading pressure increases from the sides to the center of the plate and is symmetric.

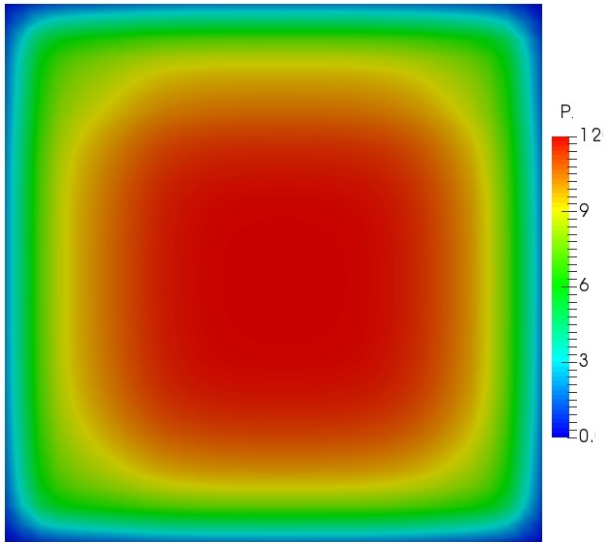

Figure 8.3: Loading pressure on the plate (units in bar) for $v = 4m/s$ and unaerated water at the peak pressure.

The particles around the plate will splash upwards with the high velocity. Figure 8.4 and 8.5 show comparison images of the motion of the plate after impact and velocity wave pattern created during impact to free surface for experimental and SPH simulation. We can see the developing splash created by the impact, see Figures 8.6 and 8.7. 8.6 and 8.7, are two figures of experimental and SPH results, and provide the results of the

splashing-up of the water around the plate and the increased jet diameter with plate entry into the water.

Figure 8.8 and 8.9 are two snapshots of the view from the bottom of the tank with jet deformation during the impact and shortly after impact onto the unaerated water and compared with experimental results (Mai et al. (2014)) and they are in reasonable qualitative agreement.

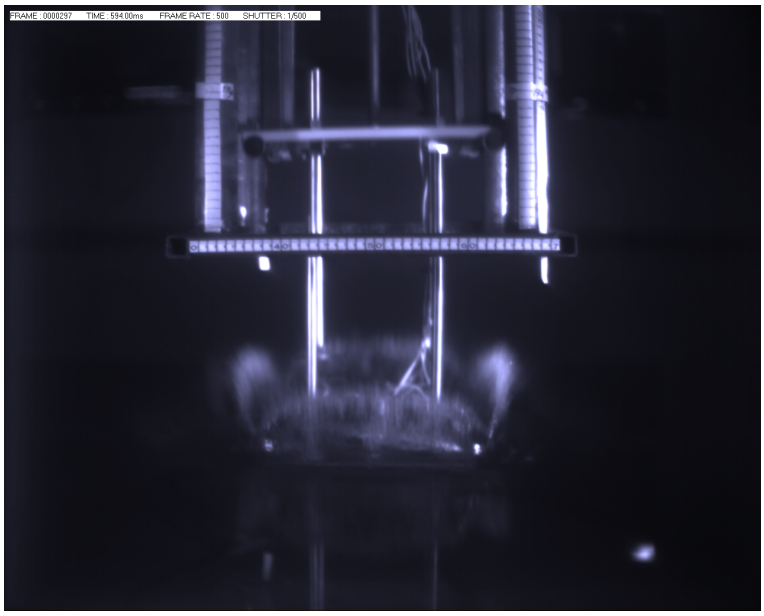

Figure 8.4: Experimental result at 0.008s after impact

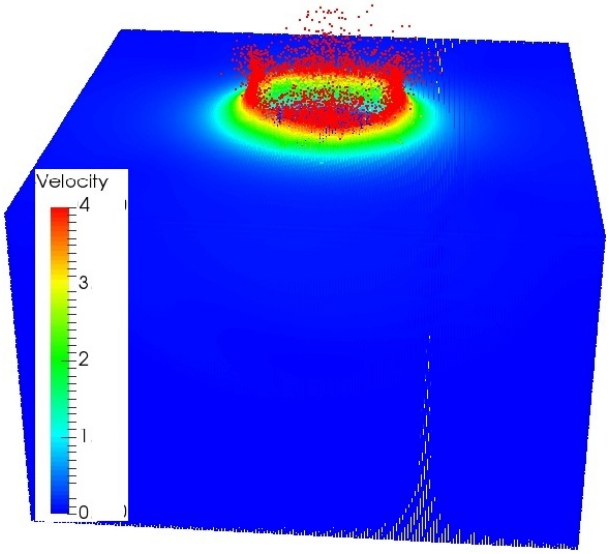

Figure 8.5: Velocity contours of a 3D flat plate impact for 4430000 particles at 0.008s after impact.

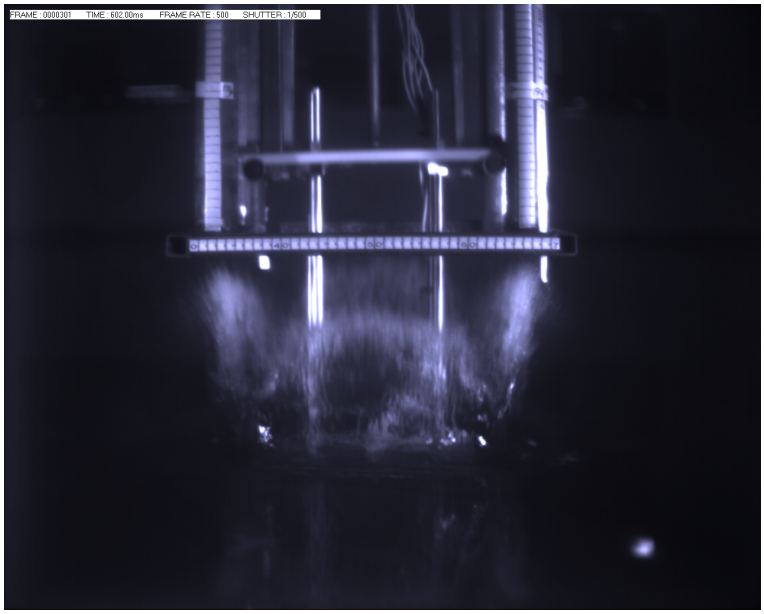

Figure 8.6: Experimental result at 0.016s after impact with the water surface

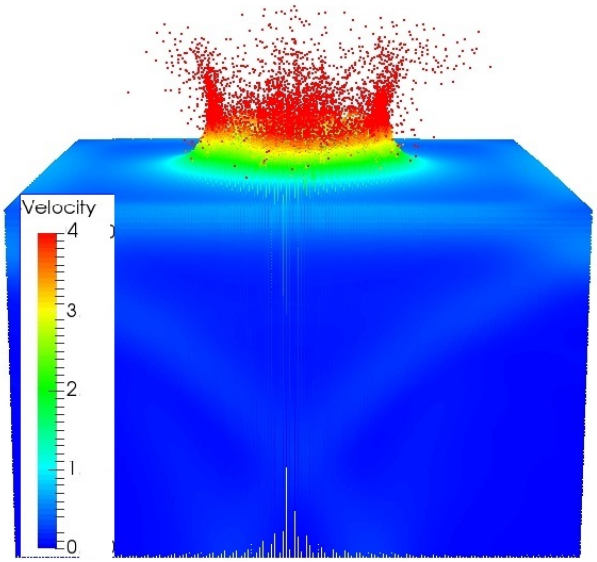

Figure 8.7: Velocity contours of a 3D flat plate impact for 4430000 particles at 0.016s after impact with the free surface.

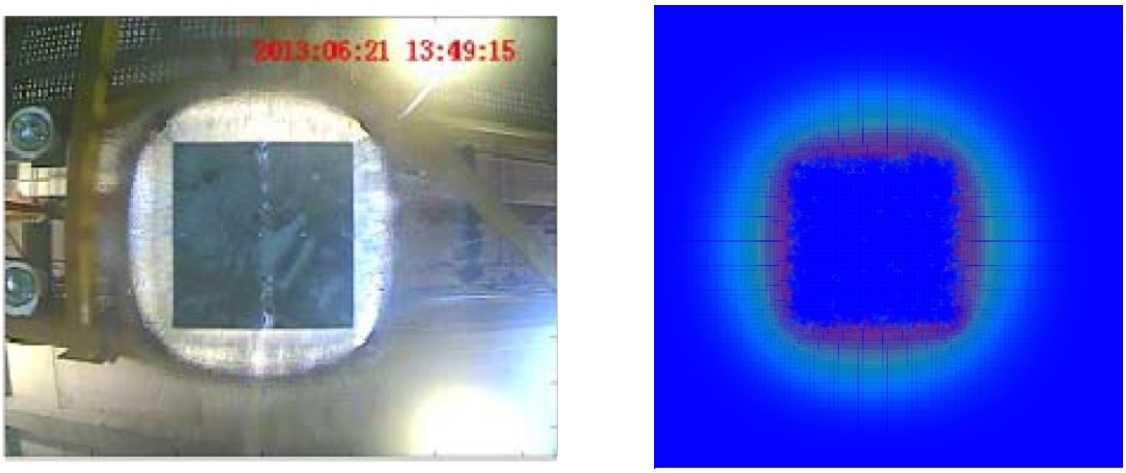

Figure 8.8: Snapshot of view from the bottom dropping flat plate into water during the impact for $v = 4$ m/s (left) Experimental results (right) SPH results.

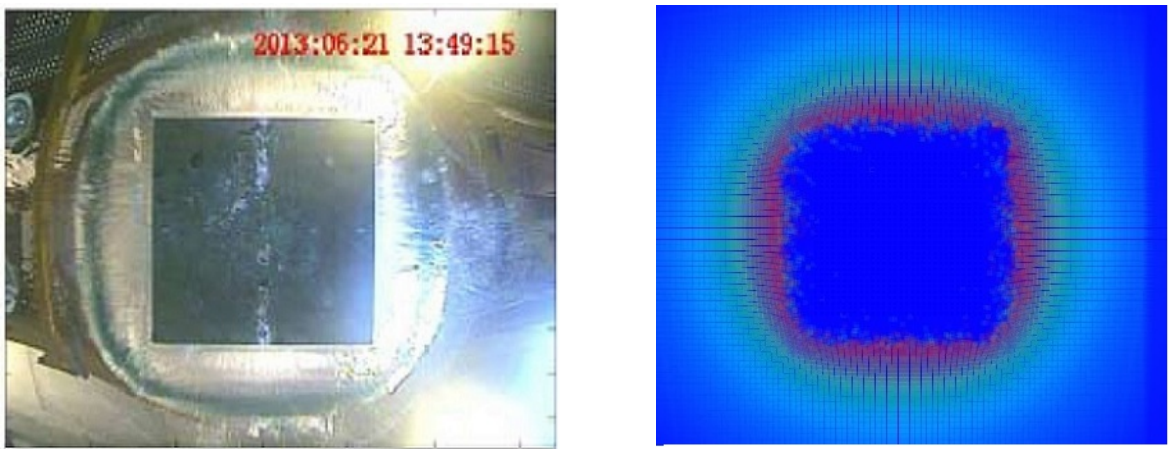

Figure 8.9: Snapshot of view from underneath impact in water for $v = 4$ m/s (left) Experimental results (right) SPH results.

The peak pressure at the center of plate is plotted in Figure 8.10 and Figure 8.11 for v = 5m/s and v = 7m/s, respectively. They show high impact pressures for fresh water, with the impact pressure reducing by adding more aeration. We see there are differences in pressure peaks in experimental compared to the finite volume results (Mai (2017)). Due to bubble rising creating aerated water, the surface will not be flat and the water surface is higher for large aeration levels, Ma et al. (2016). Especially, in 1.6% aeration level, there is a significant difference between numerical and experimental results, see Table 8.1. In addition, in SPH we set the water surface flat for all cases. The details of pressure at the points ($P_1 - P_5$) for different aeration levels at different impact velocities are listed in Tables 8.1, 8.2 and show high pressure at the center of the plate. Lower pressure are predicted towards the edges of the plate and the pressure are comparable at each edge point. Plate pressure levels in general, and peak pressure in particular are increased by reducing the aeration level. At the same time, the peak pressure is decreased by reducing the impact velocity.

	$v = 5m/s$		$v = 7m/s$	
	Exp.	SPH(SP3D)	Exp.	SPH(SP3D)
P_1	-	2.198	3.26	3.1358
P_2	-	2.339	2.6332	3.23857
P_3	-	2.133	3.333	3.03961
P_4	-	2.062	5.569	2.9123
P_5	-	2.153	5.288	3.1084

	$v = 5m/s$		$v = 7m/s$	
	Exp.	SPH(SP3D)	Exp.	SPH(SP3D)
P_1	2.49515	2.628	2.8396	3.674
P_2	3.0418	3.508	2.7138	3.998
P_3	3.08	3.204	4.036	3.723
P_4	2.702	3.054	3.41	3.344
P_5	1.780	3.362	2.352	3.451

Table 8.1: Maximum gauge pressure of the plate with aeration level: left: 1.6% and right: 1.02% aeration

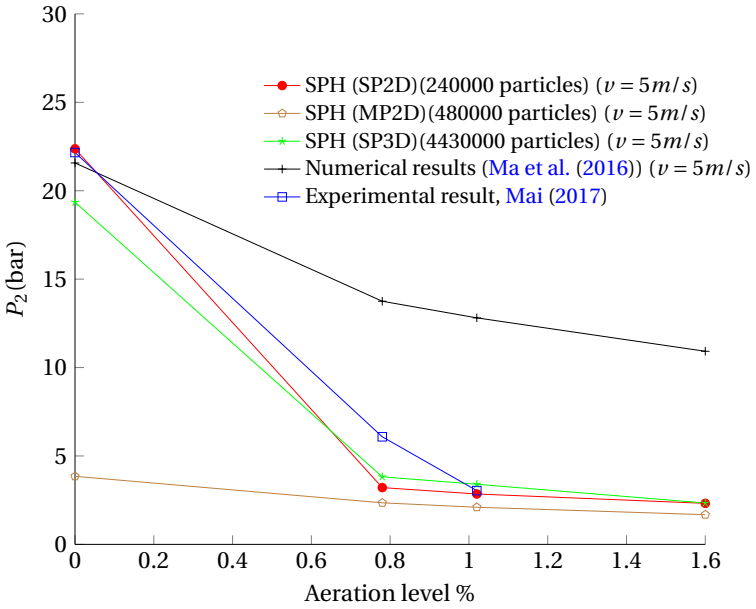

Figure 8.10: The peak impact gauge pressure affected by aeration at $v = 5m/s$

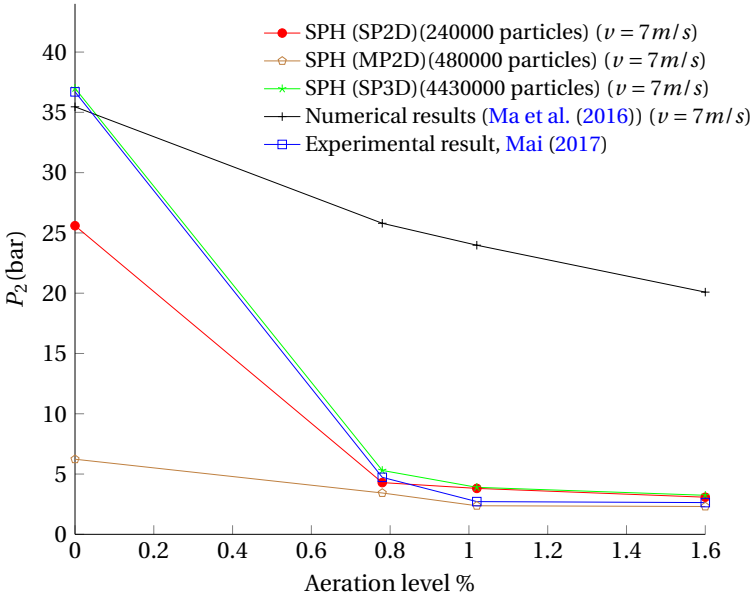

Figure 8.11: The peak impact gauge pressure affected by aeration at $v = 7m/s$

	$v = 5m/s$		$v = 7m/s$	
	Exp.	SPH(SP3D)	Exp.	SPH(SP3D)
P_1	6.01698	3.045	4.6547	3.253
P_2	6.084	3.820	4.729	3.714
P_3	5.78	3.109	7.389	3.14
P_4	1.041	3.265	2.874	3.26
P_5	6.11	3.638	3.049	4.1

	$v = 5m/s$		$v = 7m/s$	
	Exp.	SPH(SP3D)	Exp.	SPH(SP3D)
P_1	6.521	17.504	14.99	20.155
P_2	22.37	19.35	36.6996	37
P_3	8.379	15.6	15.933	18.098
P_4	9.309	14.7	12.449	19.6
P_5	11.47	18.87	10.786	23.93

Table 8.2: Maximum gauge pressure of the plate with aeration level: left: 0.78% and right: 0.0% aeration

8.1 Conclusion

The 2D single phase model has been extended in this chapter to 3D. The 3D simulation is more realistic but needs a large computational domain and more particles. The total number of particles used in 3D simulation is 4430000. The results indicate that computed impact loading on the flat during the water entry is in generally good agreement with experimental results for the loading pressure at 5 points on the plate. The 3D results showed more detail of splashing compared to 2D simulations, as with 3D, all sides of splashing water can be seen.

As we mentioned in the previous chapters, comparison between 2D single and multi-phase results are not much different and did not influence the fluid moving and free surface significantly. We simulated 3D single and multi-phase dam-break for two different cases as well and we found out at the the same, that there was no significant change. In both 2D and 3D, we have investigated the influence of the air phase which has shown the same influence in 2D and 3D multi-phase for dam-break. The drop plate cases for 2D single and multi-phase have been shown. From these simulation results, we have decided to simulate only 3D single-phase for drop plate. The 3D model provides a more faithful representation of the water motion then 2D model. It also predicts impact pressure acceptably well. The main reason for not extending the 3D model to multiphase is that, based upon 2D computations, the particle

resolution required to adequately resolve the air flow under the plate would be excessive. Very high resolution would be required to achieve converged results for impact pressures and the improvement expected compared with multiphae 2D or single-phase 3D does not justify the additional computational expense.

CHAPTER 9

CONCLUSION AND FUTURE WORK

Contents

9.1 Main Conclusion

This thesis has presented a smoothed particle hydrodynamics (SPH) model using Parallel code (MPI) to simulate several cases from lid-driven-cavity, Rayleigh-Taylor instability, rising bubble in water, dambreak and flat plate impact upon a bubbly water-air mixture in 2D and 3D.

Two different boundary conditions methods have been described: the first is a fixed dummy particles technique and second technique is a ghost particle method. The advantage of the first method is the saving of computational time compared to the second technique, but the second

is more fixable in adapting to the multi-phase SPH model. Therefore, the use of the ghost particle technique is preferred.

To assess the capability of the model the lid-driven cavity, dam break problems (wet and dry bed) have been investigated. In dam break cases, the prediction of load of pressure at the right corner and the height of the water with the toe of the water have been the main points of interest and have been compared to other numerical Colagrossi & Landrini (2003), Adami et al. (2012) and experimental results Martin & Moyce (1952). The result of a dam break with wet bed has been compared with Violeau & Issa (2007) and Jánosi et al. (2004), numerical and experimental results, respectively. Good agreement is achieved for comparison between them.

Multi-phase simulations for dam break, Rayleigh-Taylor and bubble rising problems have been studied. The results of multi-phase problems are compared to the single phase simulations and other numerical Cummins & Rudman (1999), Hu & Adams (2009*a*), Colagrossi & Landrini (2003), Sussman et al. (1994) and experimental results, Martin & Moyce (1952). The results obtained good agreement between SPH simulations and other numerical and experimental results.

The number of particles required in multi-phase cases is highly increased, therefore, to simulate such cases. Running serial code on a single CPU takes a large amount of computational time and the number of particles will be limited. The use of the MPI code enables running the simulations with millions of particles. The structure and detail of MPI

code are described in Chapter three.

A background pressure has been applied to prevent the formation of unphysical voids in the less dense phase at high resolutions instead of shifting algorithm, Mokos et al. (2017). The results are compared to other numerical and SPH results, the agreement between this study and another results are close.

For more realistic simulations, a 3D dam break case has been studied. The results achieved are compared with 2D single phase, multi-phase, numerical and experimental results of Colagrossi & Landrini (2003) and Martin & Moyce (1952), respectively. The results are shown generally with good agreement between them.

Finally, 2D and 3D simulations of a dropping plate onto the stationary water with aeration level between 0% – 1.6% have been investigated with the SPH model for three different velocities $v = 4$ m/s, 5 m/s and 7 m/s. The speed of the plate as it enters the water is specified from the experiments and data from this are used as boundary conditions for the SPH model. The sounds speeds used in this study are much larger than ten times the maximum fluid velocity u and are set as physical sound speeds determined by aeration level in the water-air mixture. The results obtained are compared to the experimental results; numerical results show the pressure peak on the plate is reduced compared to the single phase method, due to air cushioning over the plate. The role of the air particles is shown on the water surface before and after impact and has

an important role. In 2D and 3D simulations, the loading pressure on the plate at three points (2D) and five points (3D) has been the main point of interest. Results for these quantities have been compared to the FROTH project at the University of Plymouth and numerical results, Ma et al. (2016) and Mai (2017), the results show to be in good agreement.

9.2 Future research

To extend the work presented in this thesis possible avenues for further investigation could include the following:

- Full parallelisation in x, y, z direction: The use of parallel code to run large numbers of particle and to reduce the computation times for 3D multiphase simulations should push further. This will require a capable code. Instead of 1-dimensional domain decomposition into vertical slices and giving each slice to a different processor, 2-dimensional $(x-y)$ or 3-dimensional decomposition $(x-y-z)$ strategies could be developed.

- Coupled fluid/solid model that predicts the velocity of the plate rather than assume the velocity: In experiments the velocity during impact was integrated from the measured data recorded by an accelerometer.

  Investigation of predict the velocity of the plate after find the deflection of springs and taking into account the friction between plate

and holders, should be interesting in future work.

- More highly-resolved 3D simulations. However, due to the resolution required, this would require super-computing resources: To reduce the particle number and computational cost, variable resolution methods, including finer refinement around the plate and less fine far away from the plate could be used.

- Treatment of the air/water flow as an inhomogeneous mixture rather than assuming homogeneity as at present. The void fraction depends upon the total volume of all bubbles, but the bubble size varies. Then the air/water mixture during the simulation would not be guaranteed to remain homogeneous. Investigation of the air-water flow as an inhomogeneous mixture should be interesting for future work.

BIBLIOGRAPHY

Adami, S., Hu, X. & Adams, N. (2012), 'A generalized wall boundary condition for smoothed particle hydrodynamics', **231**(21), 7057–7075.

Barcarolo, D., Le Touzé, D. & De Vuyst, F. (2012), 'Validation of a new fully-explicit incompressible smoothed particle hydrodynamics method', *Blucher Mechanical Engineering Proceedings* **1**(1), 380–396.

Bonet, J. & Lok, T.-S. (1999), 'Variational and momentum preservation aspects of smooth particle hydrodynamic formulations', *Computer Methods in applied mechanics and engineering* **180**(1), 97–115.

Brennen, C. E. (1995), *Cavitation and Dynamics*, Oxford University versity Press.

Buchner, B. (2002), 'Green water on ship-type offshore structures', *Ph.D. thesis, Delft University of Technology* .

Cao, X., Ming, F. & Zhang, A. (2014), 'Sloshing in a rectangular tank based on sph simulation', *Applied Ocean Research* **47**, 241 – 254.

Chen, Z., Zong, Z., Liu, M., Zou, L., Li, H. & Shu, C. (2015), 'An sph model for multiphase flows with complex interfaces and large density dif-

ferences', *Journal of Computational Physics* **283**(Supplement C), 169 – 188.

Cherfils, J., Pinon, G. & Rivoalen, E. (2012), 'Josephine: A parallel {SPH} code for free-surface flows'.

Chuang, S.-L. et al. (1966), 'Experiments on flat-bottom slamming', *Journal of Ship Research* **10**(01), 10–17.

Colagrossi, A., Antuono, M., Souto-Iglesias, A. & Le Touzé, D. (2011), 'Theoretical analysis and numerical verification of the consistency of viscous smoothed-particle-hydrodynamics formulations in simulating free-surface flows', *Phys. Rev. E* **84**, 026705.

Colagrossi, A. & Landrini, M. (2003), 'Numerical simulation of interfacial flows by smoothed particle hydrodynamics', *J. Comput. Phys.* **191**(2), 448–475.

Colicchio, G., Landrini, M. & Chaplin, J. R. (2005), 'Level-set computations of free surface rotational flows', *Journal of Fluids Engineering* **127**(6), 1111–1121.

Crespo, A., Gomez-Gesteira, M. & Dalrymple, R. A. (2008), 'Modeling dam break behavior over a wet bed by a sph technique', *Journal of waterway, port, coastal, and ocean engineering* **134**(6), 313–320.

Crespo, A., Gomez-Gesteira, M., Dalrymple, R. A. et al. (2007), 'Boundary

conditions generated by dynamic particles in sph methods', *CMC-TECH SCIENCE PRESS-* **5**(3), 173.

Cummins, S. J. & Rudman, M. (1999), 'An {SPH} projection method', *Journal of Computational Physics* **152**(2), 584 – 607.

D. Violeau, A. Leroy, A. M. (2014), Exact computation of sph wall renormalising integrals in 3-d, 9 th SPHERIC International Workshop, pp. 95–102.

Dalrymple, R. & Knio, O. (2001), *SPH modeling of water waves*, Vol. 260, pp. 779–787.

Dalrymple, R. & Rogers, B. (2006), 'Numerical modeling of water waves with the sph method', *Coastal Engineering* **53**(2), 141 – 147. Coastal Hydrodynamics and Morphodynamics.

Dehnen, W. & Aly, H. (2012), 'Improving convergence in smoothed particle hydrodynamics simulations without pairing instability', *Monthly Notices of the Royal Astronomical Society* **425**(2), 1068–1082.

Dilts, G. A. (1999), 'Moving-least-squares-particle hydrodynamics?i. consistency and stability', **44**(8), 1115–1155.

Feldman, J. & Bonet, J. (2007), 'Dynamic refinement and boundary contact forces in sph with applications in fluid flow problems', *International Journal for Numerical Methods in Engineering* **72**(3), 295–324.

Ferrand, M., Laurence, D. R., Rogers, B. D., Violeau, D. & Kassiotis, C. (2013), 'Unified semi-analytical wall boundary conditions for inviscid,

laminar or turbulent flows in the meshless sph method', *International Journal for Numerical Methods in Fluids* **71**(4), 446–472.

Ferrari, A., Dumbser, M., Toro, E. & Armanini, A. (2010), A new parallel sph method for 3d free surface flows, *in* 'High Performance Computing on Vector Systems 2009', Springer, pp. 179–188.

Fourtakas, G. (2014), 'Modelling multi-phase flows in nuclear decommissioning using sph', *University of Manchester, Manchester, UK* .

Gao, R., Ren, B., Wang, G. & Wang, Y. (2012), 'Numerical modelling of regular wave slamming on subface of open-piled structures with the corrected sph method', *Applied Ocean Research* **34**, 173 – 186.

Ghia, U., Ghia, K. & Shin, C. (1982), 'High-re solutions for incompressible flow using the navier-stokes equations and a multigrid method', *Journal of Computational Physics* **48**(3), 387 – 411.

Gingold, R. A. & Monaghan, J. J. (1977), 'Smoothed particle hydrodynamics: theory and application to non-spherical stars', *Monthly notices of the royal astronomical society* **181**(3), 375–389.

Gomez-Gesteira, M., Rogers, B. D., Dalrymple, R. A. & Crespo, A. J. (2010), 'State-of-the-art of classical sph for free-surface flows', *Journal of Hydraulic Research* **48**(S1), 6–27.

Gong, K., LIU, H. & long WANG, B. (2009), 'Water entry of a wedge based

on sph model with an improved boundary treatment', *Journal of Hydrodynamics, Ser. B* **21**(6), 750 – 757.

Gotoh, H. & Sakai, T. (1999), 'Lagrangian simulation of breaking waves using particle method', *Coastal Engineering Journal* **41**(3-4), 303–326.

Grenier, N., Antuono, M., Colagrossi, A., Touze, D. L. & Alessandrini, B. (2009), 'An hamiltonian interface sph formulation for multi-fluid and free surface flows', *Journal of Computational Physics* **228**(22), 8380 – 8393.

Guo, X., Lind, S., Rogers, B., Stansby, P. & Ashworth, M. (2013), Efficient massive parallelisation for incompressible smoothed particle hydrodynamics with 108 particles, *in* 'Proceedings of the 8th International SPHERIC Workshop, Trondheim, Norway', pp. 397–402.

Hu, X. & Adams, N. (2009*a*), 'A constant-density approach for incompressible multi-phase {SPH}', *Journal of Computational Physics* **228**(6), 2082 – 2091.

Hu, X. & Adams, N. (2009*b*), 'A constant-density approach for incompressible multi-phase sph', *Journal of Computational Physics* **228**(6), 2082–2091.

Hu, X. Y. & Adams, N. A. (2006), 'A multi-phase sph method for macroscopic and mesoscopic flows', *J. Comput. Phys.* **213**(2), 844–861.

Hu, X. Y. & Adams, N. A. (2007), 'An incompressible multi-phase sph method', *J. Comput. Phys.* **227**(1), 264–278.

Huera-Huarte, F., Jeon, D. & Gharib, M. (2011), 'Experimental investigation of water slamming loads on panels', *Ocean Engineering* **38**(11-12), 1347–1355.

Hughes, J. P. & Graham, D. I. (2010), 'Comparison of incompressible and weakly-compressible sph models for free-surface water flows', *Journal of Hydraulic Research* **48**(S1), 105–117.

Jánosi, I. M., Jan, D., Szabó, K. G. & Tél, T. (2004), 'Turbulent drag reduction in dam-break flows', *Experiments in Fluids* **37**(2), 219–229.

Koshizuka, S., Nobe, A. & Oka, Y. (1998), 'Numerical analysis of breaking waves using the moving particle semi,Äêimplicit method', *International Journal for Numerical Methods in Fluids* **26**(7), 751–769.

Koukouvinis, P.-C. K. (2012), 'Development of a meshfree particle method for the simulation of steady and unsteady free surface flows: application and validation of the method on impulse hydraulic turbines'.

Kulasegaram, S., Bonet, J., Lewis, R. & Profit, M. (2004), 'A variational formulation based contact algorithm for rigid boundaries in two-dimensional sph applications', *Computational Mechanics* **33**(4), 316–325.

Lee, E., Moulinec, C., Xu, R., Violeau, D., Laurence, D. & Stansby, P. (2008*a*), 'Comparisons of weakly compressible and truly incompressible algorithms for the sph mesh free particle method', *Journal of Computational Physics* **227**(18), 8417–8436.

Lee, E., Moulinec, C., Xu, R., Violeau, D., Laurence, D. & Stansby, P. (2008*b*), 'Comparisons of weakly compressible and truly incompressible algorithms for the sph mesh free particle method', *Journal of Computational Physics* **227**(18), 8417–8436.

Leroy, A., Violeau, D., Ferrand, M. & Kassiotis, C. (2014), 'Unified semi-analytical wall boundary conditions applied to 2-d incompressible sph', *Journal of Computational Physics* **261**, 106 – 129.

Lewison, G., Maclean, W. et al. (1968), 'On the cushioning of water impact by entrapped air', *Journal of Ship Research* **12**(02), 116–130.

Libersky, L. D., Petschek, A. G., Carney, T. C., Hipp, J. R. & Allahdadi, F. A. (1993), 'High strain lagrangian hydrodynamics: A three-dimensional sph code for dynamic material response', *Journal of Computational Physics* **109**(1), 67 – 75.

Lin, M.-C. & Shieh, L.-D. (1997), 'Simultaneous measurements of water impact on a two-dimensional body', *Fluid Dynamics Research* **19**(3), 125.

Lind, S. & Stansby, P. (2016), 'High-order eulerian incompressible smoothed particle hydrodynamics with transition to lagrangian free-surface motion', *Journal of Computational Physics* **326**, 290 – 311.

Lind, S., Stansby, P., Rogers, B. & Lloyd, P. (2015*a*), 'Numerical predictions of water,Äìair wave slam using incompressible,Äìcompressible smoothed particle hydrodynamics', *Applied Ocean Research* **49**, 57 – 71.

Lind, S., Stansby, P., Rogers, B. & Lloyd, P. (2015*b*), 'Numerical predictions of water,Äìair wave slam using incompressible,Äìcompressible smoothed particle hydrodynamics', *Applied Ocean Research* **49**, 57 – 71.

Lind, S., Xu, R., Stansby, P. & Rogers, B. (2012), 'Incompressible smoothed particle hydrodynamics for free-surface flows: A generalised diffusion-based algorithm for stability and validations for impulsive flows and propagating waves', *Journal of Computational Physics* **231**(4), 1499 – 1523.

Liu, G.-R. & Liu, M. B. (2003), *Smoothed particle hydrodynamics: a mesh-free particle method*, World Scientific.

Lucy, L. B. (1977), 'A numerical approach to the testing of the fission hypothesis', *The astronomical journal* **82**, 1013–1024.

Ma, Z., Causon, D., Qian, L., Mingham, C., Mai, T., Greaves, D. & Raby, A. (2016), 'Pure and aerated water entry of a flat plate', *Physics of Fluids* **28**(1), 016104.

Mai, T. C. (2017), On the role of aeration, elasticity and wave-structure interaction on hydrodynamic impact loading, PhD thesis, University of Plymouth.

Mai, T., Greaves, D. & Raby, A. (2014), Aeration effects on impact: Drop test of a flat plate, *in* 'The Twenty-fourth International Ocean and Polar Engineering Conference (ISOPE2014)', Vol. 3.

Marrone, S., Antuono, M., Colagrossi, A., Colicchio, G., Touze, D. L. & Graziani, G. (2011), 'Œ¥-sph model for simulating violent impact flows', *Computer Methods in Applied Mechanics and Engineering* **200**(13), 1526 – 1542.

Marrone, S., Bouscasse, B., Colagrossi, A. & Antuono, M. (2012), 'Study of ship wave breaking patterns using 3d parallel sph simulations', *Computers and Fluids* **69**, 54 – 66.

Marrone, S., Colagrossi, A., Antuono, M., Lugni, C. & Tulin, M. (2011), 'A 2d+t sph model to study the breaking wave pattern generated by fast ships', *Journal of Fluids and Structures* **27**(8), 1199 – 1215.

Martin, J. & Moyce, W. (1952), 'Part iv. an experimental study of the collapse of liquid columns on a rigid horizontal plane', *Philosophical Transactions of the Royal Society of London. Series A, Mathematical and Physical Sciences* **244**(882), 312–324.

Maruzewski, P., Touzé, D. L., Oger, G. & Avellan, F. (2010), 'Sph high-performance computing simulations of rigid solids impacting the free-surface of water', *Journal of Hydraulic Research* **48**(S1), 126–134.

Miyamoto, T. & Tanizawa, K. (1984), 'A study of the impact load on ship bow', *Journal of the Society of Naval Architects of Japan* **1984**(156), 297–305.

Mokos, A. D. (2014), 'Multi-phase modelling of violent hydrodynamics using smoothed particle hydrodynamics (sph) on graphics processing units (gpus)'.

Mokos, A., Rogers, B. D. & Stansby, P. K. (2017), 'A multi-phase particle shifting algorithm for sph simulations of violent hydrodynamics with a large number of particles', *Journal of Hydraulic Research* **55**(2), 143–162.

Monaghan, J. (1994), 'Simulating free surface flows with {SPH}', *Journal of Computational Physics* **110**(2), 399 – 406.

Monaghan, J. & Gingold, R. (1983), 'Shock simulation by the particle method sph', *Journal of Computational Physics* **52**(2), 374 – 389.

Monaghan, J. J. (1982), 'Why particle methods work', *SIAM Journal on Scientific and Statistical Computing* **3**(4), 422–433.
URL: *http://dx.doi.org/10.1137/0903027*

Monaghan, J. J. (1992), 'Smoothed particle hydrodynamics', *Annual review of astronomy and astrophysics* **30**, 543–574.

Monaghan, J. J. (2000), 'Sph without a tensile instability', *J. Comput. Phys.* **159**, 290–311.

Monaghan, J. J., Cas, R. A. F., Kos, A. M. & Hallworth, M. (1999), 'Gravity currents descending a ramp in a stratified tank', *Journal of Fluid Mechanics* **379**, 39,Äì69.

Monaghan, J. J. & Lattanzio, J. C. (1985), 'A refined particle method for astrophysical problems', *Astronomy and astrophysics* **149**, 135–143.

Monaghan, J. & Rafiee, A. (2013), 'A simple sph algorithm for multi-fluid flow with high density ratios', *International Journal for Numerical Methods in Fluids* **71**(5), 537–561.

Monaghan, J., Rung, T. & Ulrich, C. (2011), A simple and efficient sph algorithm for multi-fluids, pp. 172 – 178.

Morris, J. P., Fox, P. J. & Zhu, Y. (1997), 'Modeling low reynolds number incompressible flows using sph', *J. Comput. Phys.* **136**(1), 214–226.

Nugent, S. & Posch, H. (2000), 'Liquid drops and surface tension with smoothed particle applied mechanics', *Physical Review E* **62**(4), 4968.

Oger, G., Doring, M., Alessandrini, B. & Ferrant, P. (2006), 'Two-dimensional sph simulations of wedge water entries', *Journal of Computational Physics* **213**(2), 803 – 822.

Oger, G., Le Touzé, D., Guibert, D., De Leffe, M., Biddiscombe, J., Soumagne, J. & Piccinali, J.-G. (2016), 'On distributed memory mpi-based

parallelization of sph codes in massive hpc context', *Computer Physics Communications* **200**, 1–14.

Oger, G., Marrone, S., Touze, D. & de Leffe, M. (2016), 'Sph accuracy improvement through the combination of a quasi-lagrangian shifting transport velocity and consistent ale formalisms', *Journal of Computational Physics* **313**, 76 – 98.

Okada, S. & Sumi, Y. (2000), 'On the water impact and elastic response of a flat plate at small impact angles', *Journal of marine science and technology* **5**(1), 31–39.

Panizzo, A. & Dalrymple, R. (2004), 'Sph modelling of underwater landslide generated waves', *COASTAL ENGINEERING CONFERENCE* **29**, 1147.

Peters, I. R., van der Meer, D. & Gordillo, J. M. (2013), 'Splash wave and crown breakup after disc impact on a liquid surface', *Journal of Fluid Mechanics* **724**, 553,Äì580.

Quinlan, N. J., Basa, M. & Lastiwka, M. (2006), 'Truncation error in mesh-free particle methods', *International Journal for Numerical Methods in Engineering* **66**(13), 2064–2085.

Randles, P. & Libersky, L. (1996), 'Smoothed particle hydrodynamics: Some recent improvements and applications', *Computer Methods in Applied Mechanics and Engineering* **139**(1), 375 – 408.

Shadloo, M. S., Zainali, A., Yildiz, M. & Suleman, A. (2012), 'A robust weakly compressible sph method and its comparison with an incompressible sph', *International Journal for Numerical Methods in Engineering* **89**(8), 939–956.

Shakibaeinia, A. & Jin, Y.-C. (2011), 'A mesh-free particle model for simulation of mobile-bed dam break', *Advances in Water Resources* **34**(6), 794–807.

Shao, S. & Lo, E. Y. (2003), 'Incompressible {SPH} method for simulating newtonian and non-newtonian flows with a free surface', *Advances in Water Resources* **26**(7), 787 – 800.

Shepard, D. (1968), A two-dimensional interpolation function for irregularly-spaced data, *in* 'Proceedings of the 1968 23rd ACM National Conference', ACM '68, ACM, New York, NY, USA, pp. 517–524.

Skillen, A., Lind, S., Stansby, P. K. & Rogers, B. D. (2013), 'Incompressible smoothed particle hydrodynamics (sph) with reduced temporal noise and generalised fickian smoothing applied to body,Äìwater slam and efficient wave,Äìbody interaction', *Computer Methods in Applied Mechanics and Engineering* **265**, 163 – 173.

Sun, P., Ming, F. & Zhang, A. (2015), 'Numerical simulation of interactions between free surface and rigid body using a robust sph method', *Ocean Engineering* **98**, 32 – 49.

Sussman, M., Smereka, P. & Osher, S. (1994), 'A level set approach for computing solutions to incompressible two-phase flow', *ournal of Computational Physics* **114**(1), 146 – 159.

Takeda, H., Miyama, S. M. & Sekiya, M. (1994), 'Numerical simulation of viscous flow by smoothed particle hydrodynamics', *Progress of Theoretical Physics* **92**(5), 939–960.

Verhagen, J. et al. (1967), 'The impact of a flat plate on a water surface', *Journal of Ship Research* **11**(04), 211–223.

Verlet, L. (1967), 'Computer" experiments" on classical fluids. i. thermodynamical properties of lennard-jones molecules', *Physical review* **159**(1), 98.

Viccione, G., Bovolin, V. & Carratelli, E. P. (2008), 'Defining and optimizing algorithms for neighbouring particle identification in sph fluid simulations', *International Journal for Numerical Methods in Fluids* **58**(6), 625–638.

Vila, J. P. (1999), 'On particle weighted methods and smooth particle hydrodynamics', *Mathematical Models and Methods in Applied Sciences* **09**(02), 161–209.

Violeau & Issa, R. (2007), Spheric benchmark test case number 5: sensitivity analysis to numerical and physical parameters, *in* editor, ed., 'booktitle'.

Wendland, H. (1995), 'Piecewise polynomial, positive definite and compactly supported radial functions of minimal degree', *Advances in computational Mathematics* **4**(1), 389–396.

Xu, R., Stansby, P. & Laurence, D. (2009*a*), 'Accuracy and stability in incompressible sph (isph) based on the projection method and a new approach', *Journal of Computational Physics* **228**(18), 6703 – 6725.

Xu, R., Stansby, P. & Laurence, D. (2009*b*), 'Accuracy and stability in incompressible sph (isph) based on the projection method and a new approach', *Journal of computational Physics* **228**(18), 6703–6725.

Yan, S. & Ma, Q. (2007), 'Numerical simulation of fully nonlinear interaction between steep waves and 2d floating bodies using the qale-fem method', *Journal of Computational Physics* **221**(2), 666 – 692.

Zhang, Y. (2010), 'A level set immersed boundary method for water entry and exit'.

Zhao, R., Faltinsen, O. & Aarsnes, J. (1996), Water entry of arbitrary two-dimensional sections with and without flow separation, *in* 'Proceedings of the 21st symposium on naval hydrodynamics', Trondheim, Norway, National Academy Press, Washington, DC, USA, pp. 408–423.

Zhou, Z. Q., Kat, J. O. D. & Buchner, B. (1999), A nonlinear 3D approach to simulate green water dynamics on deck, *in* 'Seventh international conference on numerical ship hydrodynamics', pp. 1–4.